Design and optimization of microwave antenna array for next-generation wireless networks

Politecnico di Bari

Department of Electrical and Information Engineering
ELECTRICAL AND INFORMATION ENGINEERING
Ph.D. Program
SSD: IINF-02/A –ELECTROMAGNETIC FIELDS

Final Dissertation

Design and optimization of microwave antenna array for next-generation wireless networks

---

by
Md. Imran Khan

Supervisor:

Prof. Francesco Prudenzano

Coordinator of Ph.D. Program:
Prof. Nicola Giaquinto

Course n°38, 01/04/2023-31/03/2026

Politecnico di Bari

Department of Electrical and Information Engineering
ELECTRICAL AND INFORMATION ENGINEERING
Ph.D. Program
SSD: IINF-02/A –ELECTROMAGNETIC FIELDS

Final Dissertation

Design and optimization of microwave antenna array for next-generation wireless networks

---

by

Md. Imran Khan

Md. Imran Khan

Referees:

Prof. Gino Sorbello

Dr. Valeria Marrocco

Supervisor:

Prof. Francesco Prudenzano

Francesco Prudenzano

Coordinator of Ph.D Program:

Prof. Nicola Giaquinto

Nicola Giaquinto

Course n°38, 01/04/2023-31/03/2026

Abstract

This Ph.D. thesis presents different novel high-performance antenna systems for satellite communication, 5G wireless networks, and RADAR system applications. The research deals with several aspects of antenna during design to produce electromagnetic structures for exhibiting high gain, wide bandwidth, and cost-effective fabrication. To meet the demands of modern communication systems, all critical issues present in conventional antennas are addressed and solved through proper electromagnetic design.

The first part of this thesis focuses on planar transmitarray antenna, which provides dual polarized radiation while maintaining a compact architecture. After fabrication and characterization, this multi-layer phase-compensating structure demonstrates a peak gain of approximately 21 dB with beam steering up to ±30°. This transmitarray can be considered as a practical alternative to the conventional high gain antenna as it features low transmission loss, accurate phase control, and low side-lobe levels.

Next, the thesis focuses on additive manufacturing techniques based Fabry–Pérot cavity antennas. In this antenna, gain is enhanced through constructive interference executed by partially reflective surfaces, while low-cost and scalable fabrication is enabled through conductive inkjet printing. Cost-effective manufacturing method is used to produce flexible microwave structure. Measurement shows that this fabricated cavity antenna exhibits a maximum gain of approximately 13.2 dBi with a 3 dB gain bandwidth of 24.5% proves its potential.

Wideband magneto-electric dipole antennas integrated with advanced electromagnetic structures are addressed by the subsequent work. Wide impedance bandwidth with reduced side-lobe levels is exhibited by the electromagnetic bandgap structure-based magneto-electric dipole antenna at millimeter wave frequency, while enhanced gain with slant polarization-based radiation is provided by metasurface (artificial magnetic conductor) based dipole antenna for 5G applications. The performance evaluation of these designs illustrated that the effective use of EBG (Electromagnetic Bandgap) and AMC (Artificial Magnetic Conductor) structures can control unwanted surface mode propagation for shaping radiation pattern and reduce the overall profile thickness respectively. Moreover, stable and symmetric radiation pattern is observed over the targeted band for the internal characteristics of the magneto electric dipole antenna.

Finally, a wideband patch antenna array for SOTM (Satellite Communications on the Move) applications is demonstrated which provide wide impedance bandwidth, high gain, and stable radiation patterns. This design addresses the challenges of wideband operation required for mobile satellite communications and highlight the capability of polarization control with easy integration of external electronic circuitry. Furthermore, investigation on different fabrication and system set up tolerances show minimal effect on performance makes this array more attractive.

Altogether, a comprehensive framework for designing, fabricating, and deploying antenna system of high-performance in terms of bandwidth, gain, radiation pattern, and profile compactness is established by this thesis which is significant for next-generation wireless communication technologies.

Contents

Introduction

Wireless communication in higher frequencies like Ku-band, and millimeter-wave band faces several challenges such as higher propagation losses, sensitivity to fabrication tolerances, and integration constraints make the antenna design in these frequencies more challenging [1],[2],[3]. A strong demand for antenna solutions that combine high gain, wide bandwidth, wide coverage, polarization flexibility, high efficiency, and economical fabrication is created due to the ongoing expansion of wireless technologies, including next-generation cellular networks, satellite communications and others broadband communication systems. Therefore, researchers try to explore antenna solutions that ensure a good balance between above mentioned high performances and cost-effective practical fabrication.

Among many approaches, highly directive low profile planar antennas, low-cost resonant cavity-based antennas, metasurface-enhanced magneto-electric dipoles, and stacked patch arrays have emerged as promising solutions for a wide range of applications. The following sections summarize different aspects of these designs, like specific performance or practical limitations of each type of design.

Transmitarray antennas is drawing attention nowadays as it provides high directive radiation. It makes it a suitable alternative of traditional high-gain reflectors and phased arrays. A transmitarray can focus energy from a feed into a narrow, high-gain beam, by controlling the phase shift at each unit cell across a planar surface. It is advantageous as it does not need bulky reflectors or complex active phase-shifting networks [4]. This architecture combines high gain and efficient radiation while maintaining a low-profile structure as applications like backhaul links and satellite communication need low profile structure [5], [6]. Another important feature of the transmitarray is beam steering capability which is necessary for improved coverage [7].

Though traditional transmitarray can provide excellent directivity, it suffers from complex and costly high-precision unit cells required for wideband operation. This problem can be solved by Fabry–Pérot resonator antennas (FPRAs) as it doesn't need to design any unit cell of specific phase. Rather, it forms a resonant cavity between a partially reflective surface (PRS) and a ground plane which strengthens radiation in the broadside direction and support planar and simple construction [8], [9]. FPRA can achieve wide impedance and gain bandwidths by adjusting the PRS properties while maintaining high efficiency makes it a good candidate for high-directivity applications [10]. These features make FPRA appealing for modern wireless communication system where both high directivity and simple fabrication are critical.

The need for broadband operation, stable radiation patterns, and planar integration becomes more demanding as communication systems move further into the mm-wave spectrum. Magneto-electric (ME) dipole antenna is particularly well-suited for these applications as it provides broad impedance bandwidth and stable broad-side radiation patterns by combining electric and magnetic current modes within a single planar structure [11]. The planar structure of this antenna makes it suitable for low-cost PCB fabrication, while providing high radiation efficiency across the operating band. The performance of the ME dipole antenna can be further enhanced by integrating electromagnetic bandgap (EBG) and artificial magnetic conductor (AMC) structures to control the radiation pattern and profile reduction respectively [12], [13]. Thus, this type of antenna becomes popular in 5G mm-wave applications as it offers a balance of compact planar structure and high directional performance.

Lastly, stacked patch arrays are gaining attention for the satellite communications on the move (SOTM) applications due to its capability of maintaining reliable communication with mobile platform. These stacked patch arrays employ corporate feed networks and multilayer configuration to attain dual-linear or circular polarization, wide impedance bandwidth and ensure robust operation under platform orientation variations [14]. Stacked patch arrays can be produced with conventional PCB technology due to their planar and modular design. These types of arrays offer cost-effective performance which is suitable for Ku-band mobile satellite applications [15]. The multi-stacked patch arrays are the current state-of-the-art solution for SOTM applications due to the advantages of broadband operation, polarization flexibility, and mechanical robustness.

This thesis explores the electromagnetic design, simulation, and experimental validation of advanced antenna architectures suitable for Ku band, and X band applications. Specifically, the work focuses on:

1. **Transmitarray antennas** for dual linearly polarized highly directive beamforming with beam steering capabilities at Ku band.
2. **Fabry Pérot antenna** with metasurface using unconventional materials for cost-effective fabrication and achieving high gain at X band.
3. **Wideband magneto-electric dipole antennas** with usage of metasurfaces like electromagnetic bandgap structure (EBG) structure for radiation pattern control by supressing surface waves and usage of artificial magnetic conductor (AMC) for profile reduction by manipulating reflecting phase at 5G millimeter wave.

4. **Dual-polarized wideband patch arrays** which offers structural simplicity and wideband operation for Ku band satellite on-the-move (SOTM) application.

The aim of this thesis is to contribute to the development of next generation antenna systems having the capability of fulfilling the demands of the modern communication system. This research emphasizes on achieving high performance, operational flexibility and manufacturability. It shows that how novel geometry, unconventional material and innovative techniques can be used to design antennas for both efficient and real-world applications.

More precisely, this thesis is organized as follows:

- Chapter 1 presents the state of the art about planar transmitarray, PRS based Fabry Pérot antenna, wideband ME dipole antenna and dual polarized array for SATCOM applications.
- Chapter 2 reports the theory of operating principles for the following components: i) Planar transmitarray, ii) PRS based Fabry Pérot antenna, iii) ME dipole antenna, iv) Artificial magnetic conductor (AMC), and v) Electromagnetic bandgap structure (EBG).
- Chapter 3 illustrates the detailed electromagnetic design of a Ku band dual polarized planar transmitarray. At first, the design of unit cell is presented along with the working principle of the equivalent circuit of that unit cell. Secondly, the phase compensation mechanism is described. Thirdly, comparison of simulated and measured result of different performance parameters of the proposed transmitarray is exhibited. Finally, the comparison with other related work is shown before the concluding remarks.

- Chapter 4 presents three antenna based on metasurface. It starts with the design, fabrication and characterization of a PRS based Fabry Pérot antenna. After that, an EBG based wideband ME dipole antenna is presented for millimeter wave applications. Finally, the design and simulated results of a low-profile AMC based wideband ME dipole antenna is proposed.
- Chapter 5 focuses on the detailed design, fabrication and characterization of an aperture coupled multi stacked patch array for SOTM applications. Also, comparison with other related works is shown in this chapter to prove the superiority of this proposed array.

1 State of the art

This chapter introduces the state-of-the-art about all the topics considered in the Ph.D. research activity, i.e. planar transmitarray, PRS based Fabry Pérot antenna, ME dipole antenna and aperture coupled wideband patch array for SATCOM application.

1.1 Planar transmitarray

Antenna plays an important role in a wide range of applications including wireless communications, broadcasting, space exploration, remote sensing and radar. Antenna technology continues to evolve for over a century driven by the requirement of the specific application area, obligation in higher frequency band, the development of advanced simulation and characterization tools and improvements in fabrication processes. The transmitarray antenna is gaining attention among the newer classes of antenna structures in recent years as a promising high-gain solution for long distance communication. Conventionally, two main design paradigms are used to achieve high-gain performance. These are geometrical optics based structures and antenna array theory based structures. The examples of first category are curved surface based parabolic reflectors [16] and dielectric lenses which are used to focus radiation. The second category is waveguide-slot arrays [17] or phased microstrip arrays [18] where multiple radiating elements with phase control are used to achieve beam shaping. Transmitarrays follow a hybrid approach. They adopt the phase control flexibility of arrays along with the aperture control mechanism of lens-based systems. Planar transmitar-

rays present a convincing choice for emerging wireless systems because of high radiation efficiency and beam reconfigurability. They are especially advantageous when high performance is present with a compact structure.

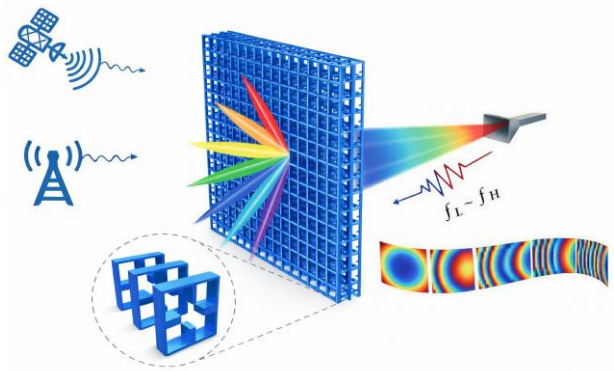

Figure 1.1 Conceptual architecture of a transmitarray antenna and its applications [19].

Figure 1.1 illustrates a transmitarray system where a feed source is illuminating on a planar transmitting surface [19]. A spherical wavefront is emitted by the feed source which is positioned at an equivalent focal point. An array of individually engineered antenna elements acts as a transmitting surface. In order to transform the spherical phase front into a planar one, each antenna element is designed with specific transmission coefficients. High-gain performance with highly focused radiation beam is achieved through this phase transformation.

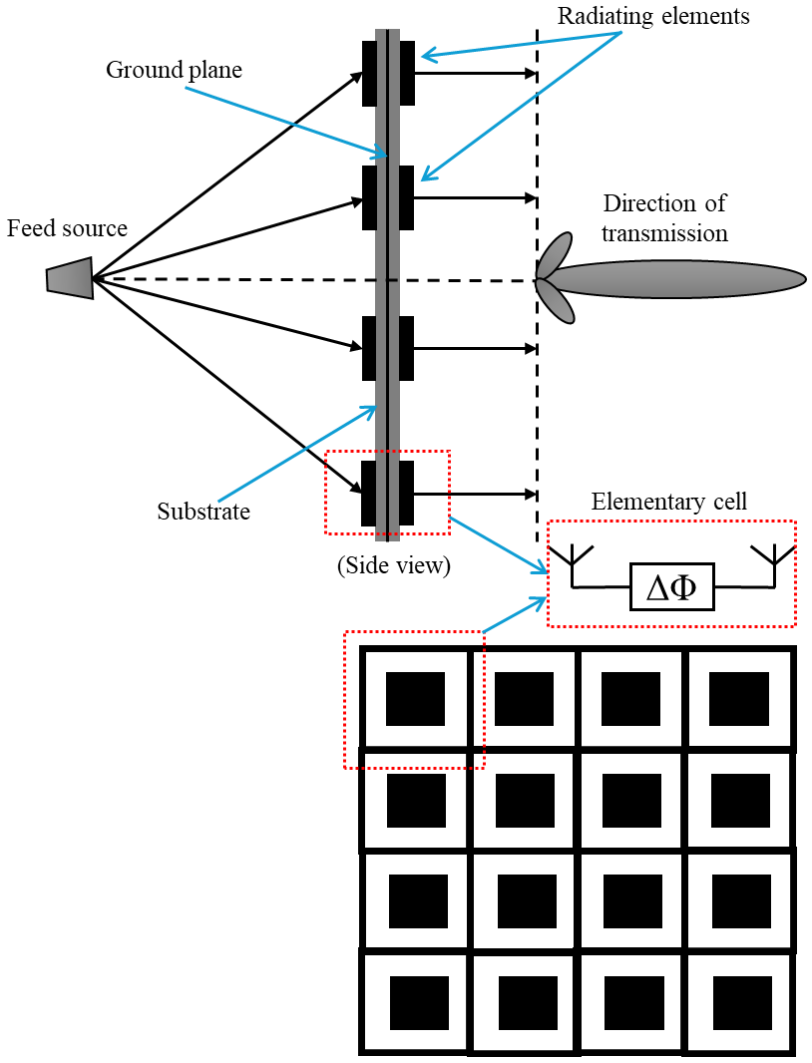

Figure 1.2 The concept of transmitarray as a lens for focusing and signal enhancements [20].

Significant performance is offered by the transmitarray antennas in many ad-

vanced applications. For example, it can be used in high-frequency wireless communications, earth remote sensing, terahertz (THz) imaging and sensing, solar energy concentration systems, and spatial power combining for high-power systems.

Far-field radiation patterns can be shaped by the transmitarray. Figure 1.2 shows that the electromagnetic energy is focused at a specific spatial location by the transmitarrays like a planar lens [20]. The transmitarray converts the incoming wavefront into a focused beam at a designated focal point in space by engineering the transmission phase distribution across the aperture through adjusting the geometries and placements of each individual radiating elements, also known as unit cells. The transmitarray is useful in short range applications also where signal focusing is required, as it exhibits the lensing functionality.

There are different approaches followed for transmitarray antenna design. Three methods are recalled here to show alternatives offering distinct advantages. Multilayer frequency selective surfaces (M-FSS), receiver–transmitter design and the metamaterial approach are three primary design techniques. The spherical phase front radiated by the feed source is converted into a planar phase front by the transmitarray. By adjusting the physical dimensions of each printed element of the array in planar surface, the transmission phase is individually controlled to convert the spherical phase front into the planar one. But, it is typically not possible to provide the full 360° phase coverage necessary for high-gain beamforming through a single-layer element array. Multi-layer structures are used to overcome this limitation. Figure 1.3 illustrates several frequency selective surface (FSS) layers separated by thick dielectric substrates or air gaps to extend the phase range while maintaining high transmission magnitude.

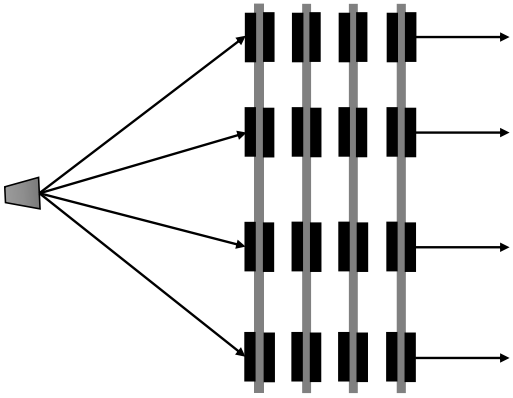

Figure 1.3 Multi-layer FSS configuration [21].

The second design technique is the receiver–transmitter configuration. Two planar arrays of printed antenna elements have formed this structure. A feed antenna illuminates the first array which received the signal. The via coupling structures or interconnecting transmission lines (metallic vias) [22] is used to transfer the received signal to the second array. The signal is radiated into the free space by the second array like a transmitter. To achieve the desired amplitude and phase distribution, the coupling mechanism between the two layers is designed carefully. Fine control over the radiation characteristics can be achieved by this method. Figure 1.4 shows the representative unit-cell structure of this kind of configuration [23].

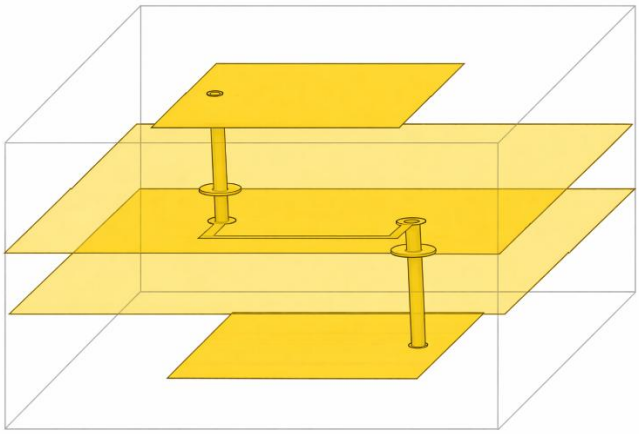

Figure 1.4 Receiver–transmitter configuration [23].

The third method involves the usage of metamaterials to manipulate the effective permittivity and permeability of the substrate for phase control in transmitarrays. The design of Huygens metasurface based transmitarray is the most popular approach among other metamaterial-related approaches. This metasurface uses the principle of Huygens to manipulate electromagnetic waves. Every point on a wavefront act as a secondary source of spherical wavelets as per the principle of Huygens. Each unit cell needs to scatter these wavelets with specific amplitude and phase for focusing, phase shifting and beam steering. A Huygens metasurface must support electric dipole moments (EDMs) and magnetic dipole moments (MDMs) for controlling wave propagation efficiently.

In contrast with the traditional M-FSS stacking, the current distribution on the corresponding layers of each unit cell of this design induce the electric and magnetic dipoles to achieve minimal reflection and high transmission with full 360^{o} phase coverage [24], [25], [26], [27], [28], [29]. A reconfigurable dual-layer Huygens element based beam-scanning transmitarray is implemented in [24].

The phase is tuned to achieve wide angle beam steering while the adjustment of the geometry related to dipole resonance is performed to tune the phase. Another work [25] experimentally demonstrated that the efficient phase control through dual polarized element of a passive Huygens' metasurface lens can improve the gain of slotted waveguide antennas. Another Huygens' metasurface with an ultrathin layer is proposed in [26]. This metasurface shows broadband behaviour with high transmittance. By shaping the resonant response through careful geometry design, it achieves 360° phase coverage. A transmitarray with high-aperture-efficiency based on Huygens' principle is proposed in reference [28]. In this design, efficient transmission is ensured by synthesizing in-phase electric and magnetic surface currents through the geometry adjustment of meta-atoms. Lastly, a near-unity aperture illumination efficiency based cavity-excited Huygens metasurface antenna is introduced in [29]. In this design, high directivity and efficiency are achieved by tuning subwavelength resonator geometry.

In comparison among these three transmitarray antenna design approaches, it can be said that the multilayer frequency selective surface (M-FSS) and the receiver–transmitter design approach typically rely on either explicit physical coupling mechanisms or a layered network interpretation. Cascading of some independent layers are often performed to form a transmitarray in the M-FSS design approach. In this case, the overall transmission phase is contributed incrementally by each layer.

In contrast, vertical metal vias or coupling structures are used by the receiver–transmitter design method. As a result, the coupling between layers can be controlled through vias or coupling structures as these structures link directly the radiating and receiving elements across layers. Despite of the advantage of coupling control mechanism between layers, this approach suffers from complex

fabrication and integration procedure. The problem is crucial at millimeter wave frequencies. Also, in case of planar implementations such as window-integrated devices it is challenging in terms of integration process.

Finally, the design approach based on metamaterial, particularly Huygens-type unit cells based design mainly focuses on manipulating the medium's effective electromagnetic properties by controlling effective electromagnetic dipole moments or subwavelength resonances. Satisfactory performance can be expected from this method if local permittivity and permeability profiles can be tailored by the collective behaviour of resonant elements. Conversely, in many cases the phase response varies rapidly with frequency when Huygens-type unit cells are inherently resonant structures. If multiple resonances are not carefully engineered, then this phenomenon can limit usable bandwidth. Additionally, precise control over both electric and magnetic dipole component is required in case of Huygens-type unit cells. These structures frequently require either layers with different metal patterns or, at least three layers or both to maintain vertical symmetry and ensure reciprocity in the unit cell design (shown in Fig. 1.5). Consequently, their practical implementation usually involves higher fabrication overhead and increased structural complexity [26] though Huygens metasurfaces offer full phase coverage and high transmission. It is noticeable that to control both the electric and the magnetic dipole moments the unit cell requires three layers with different metal layers [26].

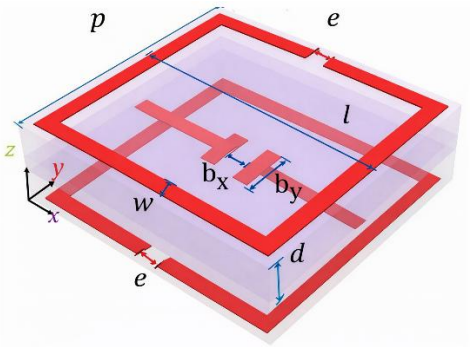

Figure 1.5 The schematic of a Huygens metasurface embedded in a homogeneous medium [26].

Considering the limitations of receiver–transmitter design and the metamaterial based approach, multi-layer frequency selective surface (M-FSS) is considered in this thesis. Study has performed on several M-FSS method based planar transmitarray antennas. Controlling the transmission magnitude and phase of the corresponding elements by varying the dimensions of metal patches on the surfaces of the backing dielectric layers is the main spirit of this method. Though, research [21],[30] show a theoretical limit which indicates that, a full 360º transmission phase range can only be achieved by using at least three layers in this M-FSS method. Over the past decade, researchers used multi-layer design as per this theoretical framework [31],[32],[33],[34],[35],[36]. To achieve the required 360º transmission phase range they used patterned metal layers which are separated and backed by either dielectrics or air gaps.

1.2 PRS based Fabry Pérot antenna

The Fabry-Pérot resonant cavity antenna (FPCA) is known as 2-D leaky-wave antenna (LWA). The main radiating mechanism of FPCA is to use a guiding structure to propagate leaky wave radially so that the beam can be formed. It can produce either pencil beams or conical beams. The most common is broadside pencil beam. Generally, a ground plane backed primary radiator covered by a partially reflecting surface (PRS) forms FPCA structure. A 2-D periodic array of metal patches with slots or a periodic frequency selective surface (FSS) can function as a PRS. However, unlike a periodic LWA, the radiation of this structure occurs from the fundamental (n = 0) space harmonic which makes it a quasi-uniform LWA [37]. This harmonic is associated with the radially propagating leaky mode of the parallel-plate waveguide. Fabry-Pérot resonant cavity antenna can also be referred as Electromagnetic Band Gap (EBG) antenna when an EBG structure is used as the PRS to form the cavity.

The FPCA structure was introduced decades ago [38]. A PRS parallel to the source located on a ground plane with a at a certain distance consist the FPCA structure. This research shows that multiple reflections occur with amplitude decrement in between the PRS and ground plane. For producing maximum radiated power at broadside direction, an expression for the resonance condition is also derived in this research [38]. An array of closely spaced parallel conducting wires consist the PRS. The generated electric filed is parallel to the PRS structure.

This FPCA structure [38] is improved by [39] through optimization of the PRS placed above of a waveguide aperture positioned in the ground plane. The wide-

band performance of the antenna results from the linear phase increment of the optimized PRS with frequency. The performance of the PRS is investigated for various element geometries [40]. These included patches, rings, dipoles, crossed dipoles, and square loops. Circular or square patches and dipoles produces less beam variation with frequency. However, in case of cross-dipoles, square loops, and rings do not show this stable behaviour. Even if the elements are closely packed together this slow variation was not found unlike patches and dipoles. In this work, patches are chosen as unit elements of the PRS for this reason.

Recent advancement in the research of these structures is studied. Various research shows different techniques for achieving multiband operation, making thinner structure and enhancing bandwidth for broadside applications. Like in [41], a multilayer PRS structure is proposed for achieving the bandwidth enhancement. Figure 1.6 shows a PRS consisting of two capacitive arrays of metallic square patches with different dimensions with a 2-D leaky wave antenna formed FPCA [41]. The condition of resonance occurs over a wide frequency range because of this two layered PRS. Square patches of the upper array are not bigger in dimensions in comparison with the patches present in the lower array. A 3 dB bandwidth of about 5.5% was obtained after optimization of the double-layer PRS, specially optimizing the size of the patches of both PRSs through several parametric studies.

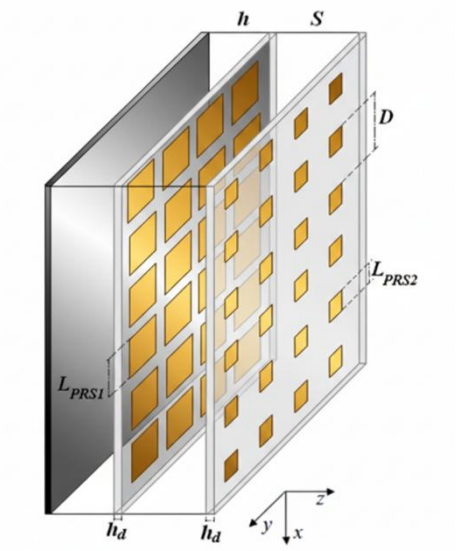

Figure 1.6 Layout of the broadband high-gain resonant leaky-wave antenna formed by two metallodielectric PRSs [40].

Research in [42] indicates that the linear increment of reflection coefficient phase with frequency is necessary for achieving high bandwidth and broadside radiation. A defected EBG structure composed of two double-layer FSSs is used in [43]. A wavelength spacing is maintained in between these two layers. An allowed frequency band was created within the EBG band gap due to the presence of the defect. A significant improvement of bandwidth is observed in this structure where a resonator is formed between the double-layer FSS and a metallic ground. In [44], bandwidth enhancement is performed through another technique. Two metallic layers of orthogonal strips etched on PCB surfaces con-

stitute the PRS which is positioned about a half-wavelength above of the ground plane [43]. Figure 1.7 shows the sketch of the structure.

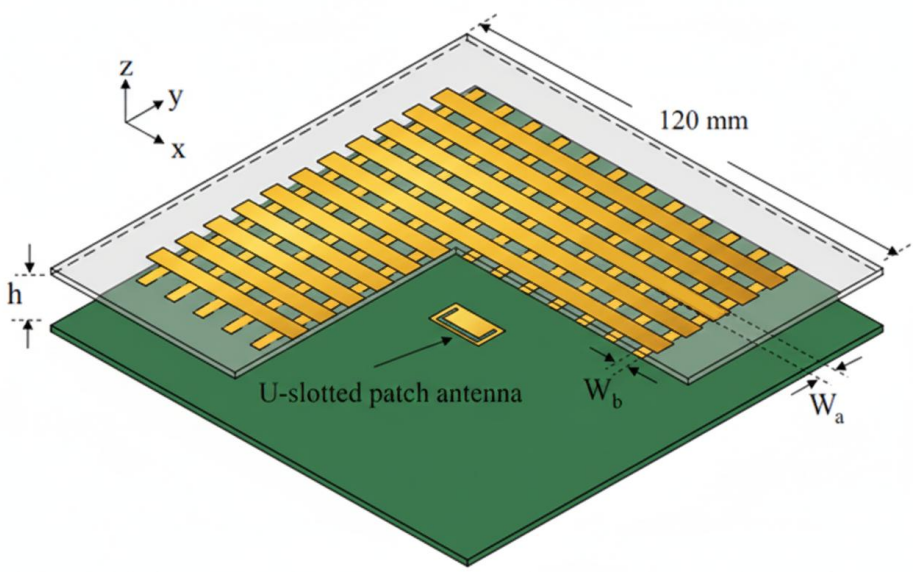

Figure 1.7 Broadband PRS antenna, with h = 11.8 mm, W_a = 4.5 mm, and W_b = 2.7 mm [43].

In [44], experimentl validation shows that the PRS of two metallic layers provides superior performance in comparison with a traditional one layer PRS antenna in terms of bandwidth enhancement. For the same gain, the 3-dB bandwidth increases from 6.2% to 12.3% when traditional one layer PRS is replaced by the two layers of PRS. Some other bandwidth enhancement approaches are discussed in [45],[46],[47],[48],[49].

Low profile Fabry-Pérot resonant cavity antenna structures is another popular area of study. To reduce the antenna profile while maintaining the high gain ca-

pability, an artificial magnetic conductor (AMC) based ground plane is used instead of a conventional PEC ground plane in [50],[51],[52]. The presence of the AMC ground plane has changed the resonance condition. As a result, the thickness of the cavity becomes half of its previous value approximately. A resonant cavity antenna based on subwavelength metamaterial is presented in [53]. The metasurface PRS composed simultaneously of an inductive and capacitive grid, and a PEC ground plane formed the cavity antenna. A 2×2 microstrip patch array is used as a multi-source to feed the antenna. Results show that high directivity and low side lobe level are achieved from this multi-source fed cavity antenna. Several works have done based on other metamaterial based resonant cavity antennas [54],[55],[56],[57],[58],[59],[60]. Figure 1.8 shows a low-profile Fabry-Pérot resonant cavity antenna[61] which also uses dual layer PRS with an easily integrated patch antenna. This cavity backed antenna exhibits higher gain and smaller cavity size in comparison with the antenna of [50]. Furthermore, the integration related problem of the feed antenna in AMC based ground plane of [50] is also solved here.

A high-gain and ultrathin resonant cavity antenna is studied in [62]. In comparison with the metamaterial based Fabry-Pérot structures of [52], [55], and [63], this antenna is advantageous in terms of structural simplicity as there is no need of integration of a high impedance surface or AMC on the substrate of the feeding patch. Also, by tuning the phase of the PRS, the total reflection phase is engineered which allows a flexibility of controlling the cavity thickness. Some other works [64],[65],[66] also research on low profile FPCA structures.

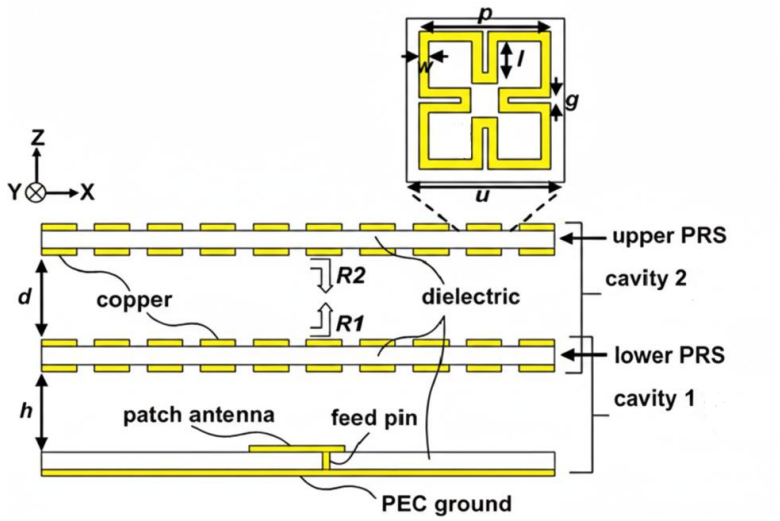

Figure 1.8 Configuration of the proposed antenna and unit cell patterns: d =5 mm, h = 5 mm, g = 0.2 mm, l = 5.7 mm, p = 15 mm, u = 15.95 mm, and w = 0.5 mm [61].

1.3 Magneto-electric (ME) dipole antenna

A magneto-electric (ME) dipole antenna supports an electric dipole mode and an orthogonal magnetic dipole mode simultaneously. The radiated fields of electric dipole and magnetic dipole combine constructively in the forward direction and destructively in the backward direction. Currently magneto-electric (ME) dipole antennas are seeking attention due to their wide bandwidth and high gain features. When the electric dipole mode and the magnetic dipole mode operating at slightly different frequencies then these features are obtained. Higher gain and higher front to back ratio are achieved as the ground plane of this antenna reflects

the backward radiation. From the first design to the evolution of ME dipole antennas will be discussed in this section.

The original concept of combining an electric dipole and a magnetic dipole was first presented by the author of [67] in 1954. Two complementary sources are excited simultaneously to make an antenna that can produce symmetrical radiation patterns in E- and H-plane [67]. A wideband unidirectional antenna having 60% impedance bandwidth, composed of electric dipole and a shorted bowtie patch was introduced by another author [68] in 2008. A vertical quarter-wave slot cavity (magnetic dipole) and a horizontal planar dipole (electric dipole) formed the antenna. To provide a wide impedance bandwidth, the two complementary dipoles radiate at the adjacent frequency bands. Due to the complementary nature of the dipoles the antenna produces symmetrical radiation patterns in both E- and H-planes and the whole operating band shows stable radiation patterns. Author of [69] presents a low-profile ME dipole with folded-cavity geometry as antennas with the low-profile feature are in high demand in many applications. The height of the ME dipole is reduced to 0.169 λ_0 while maintaining an impedance bandwidth of 45.6% and a stable high gain in the operating frequency band. Another ME dipole antenna having 60% impedance bandwidth (VSWR $\leq$ 2) is reported in [70]. This antenna is fed by a microstrip line, consists of a shorted bowtie patch placed under an electric dipole. In [71], Γ shaped probe fed ME dipole antenna with a reconfigurable beamwidth is presented. By controlling the connection of the strip and the grating reflector through switching the pin diodes conduction state, beamwidth reconfigurability in H-plane is achieved by this reported antenna [71]. For multi-band operations, some ME dipole antennas have been designed [72],[73],[74]. Also, for different polarization based applications, such as dual linear polarization [75],[76],[77],[78],[79] or circular po-

larization [80],[81],[82],[83] some ME dipole antennas have been designed by implementing different feeding methods.

With the advancement of wireless communication technologies after 2010, including 3G, Wi-Fi, and LTE, new performance requirements were imposed on antenna front-end architectures. Some features are expected from the modern day antennas due to the great demand for miniaturization of mobile devices and higher data transmission speed. These features are: (i). wide bandwidth, to support higher number of channels within the designated frequency band, (ii). sufficient high gain to mitigate free-space propagation loss, and (iii). a low-profile configuration that facilitates integration into diverse device platforms[69],[79],[84]. Figure 1.9 illustrates an A unidirectional low-profile wideband antenna [70]. In this antenna, there is a pair of horizontal patches which are functioning as electric dipoles having a wideband response. Furthermore, a quarter-wave cavity is formed by two vertical folded short patches of this antenna which is working as a magnetic dipole. This ME dipole antenna is fed by a DC grounded coaxial cable. To provide high gain and to reduce the back-lobe radiation a rectangular cavity backed ground plane is used as a reflector. This antenna also obtained wide impedance bandwidth of 45.6% with VSWR $\leq$ 1.5 while maintaining the height of only $0.169\lambda_0$ (here λ_0 is the wavelength of the center frequency of interest), benefit from the vertical oriented folded short patches. Traditionally, a profile height of $0.25\lambda_0$ is maintained as to achieve a relatively equal reflection at both low and high-frequency bands the ground plane reflector should be set at a quarter wavelength away from the radiation layer. This antenna provides roughly 3dB more gain due to the ground plane.

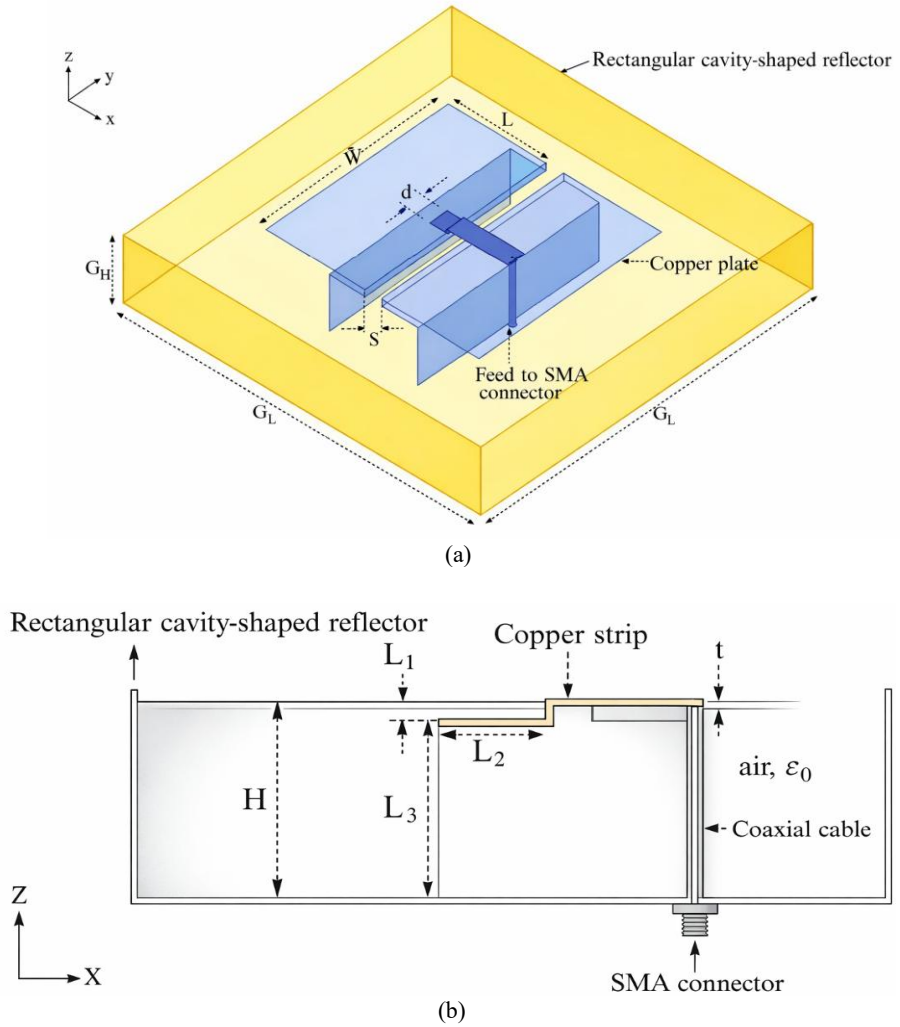

Figure 1.9 Geometry of the low-profile E dipole (a) 3D view (b). side view [70]

The design of a millimeter wave ME dipole antenna is published in 2012 [85].

A pair of planar patches, vias and a lossy substrate (Rogers 5880, $\varepsilon_r = 2.2$, thickness H = 0.787 mm) constitute this antenna. The 3-D and side view of the millimeter wave printed ME dipole antenna is shown in Figure 1.10. Excitation is accomplished through a T-shaped coupled strip feed. The feeding pin and two symmetrically placed shorting pins form a ground–signal–ground (GSG) transmission line structure. A W-type connector (from Anritsu: W1-103F) is located underneath the ground plane. The average gain of this printed ME dipole antenna is 7.5dBi with an impedance bandwidth of 33% (50GHz to 70 GHz).

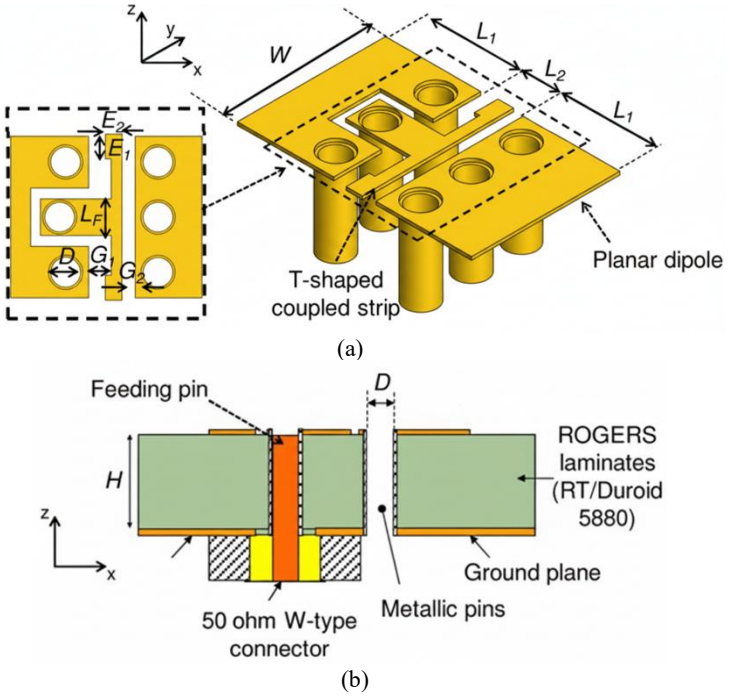

Figure 1.10 Configuration of magneto-electric dipole antenna. (a) 3-D View (c) Side View. [85]

1.4 Dual polarized array for SATCOM applications

Modern wireless communication systems are incomplete without mobile satellite communications (SATCOM). SATCOM supports a wide range of services that cover civil defense, commercial, and military applications as it can function in limited infrastructure environment [86],[87],[88]. SATCOM on-the-move (SOTM) is one of the important parts of this framework. Reliable and continuous satellite connectivity with systems with mobile terminals like airborne systems, maritime vessels and ground vehicles is the prime requirement of this communication system. SOTM scenarios are naturally very dynamic. For providing the appropriate alignment with the satellite, it has strict demands on antenna array system such as dynamic beam steering capability and the reconfigurability of the polarization of radiated beam.

Mechanical, electronic, and hybrid beam steering techniques are three principal approaches which have been developed to address these requirements [89],[90],[91],[92]. The most cost effective solution is mechanical steering, but it suffers from low tracking speeds. On the other hand, electronic steering is free from slow tracking problem but the usage of phase shifter in this approach increases system complexity and cost. By combining a fast response and reduced hardware complexity, hybrid solutions balance these trade-offs. A number of research have been performed on SOTM antenna including multilayer patch arrays[93], cavity-backed substrate-integrated waveguide (SIW) antennas [94],[95], waveguide-fed structures [96] and some novel structures [91],[92]. Figure 1.11 shows the antenna of [91] consists of orthogonal dipoles to attain the dual-polarization capability.

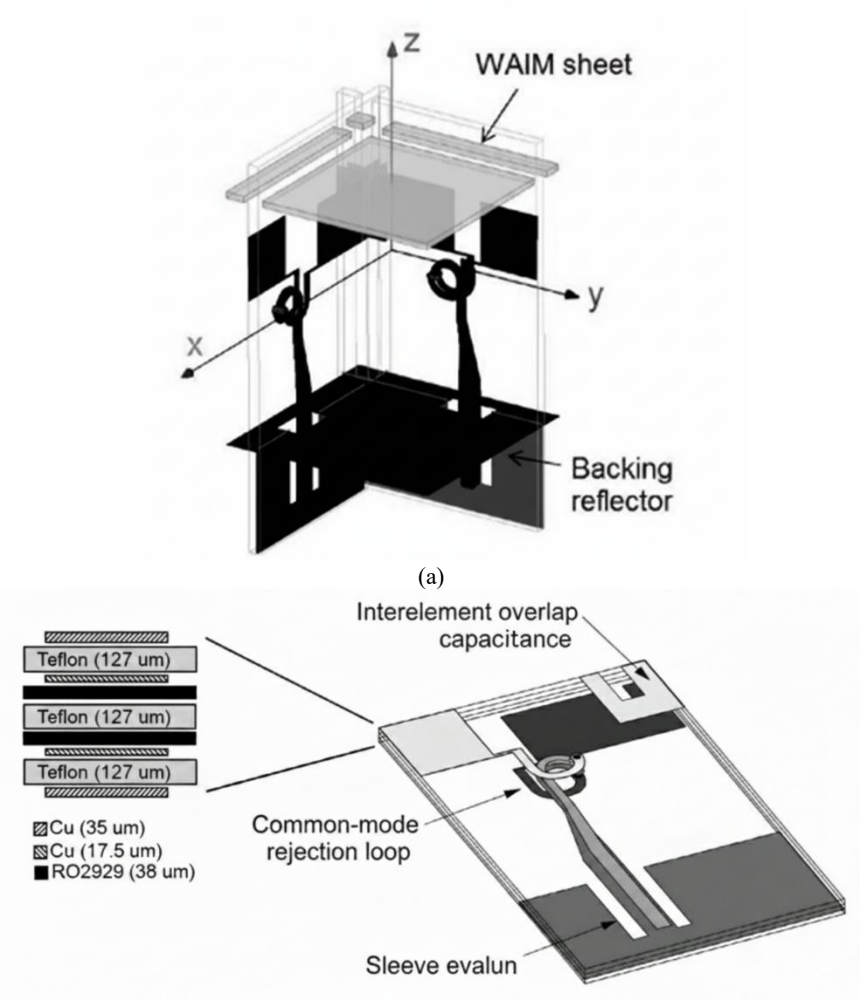

Figure 1.11 (a) Three-dimensional view of the array unit cell and (b) components of the dipole and the feed structure in the multilayer PCB [91].

Multilayer vertical printed circuit boards (PCBs) are used to print the dipoles, and to allow two sets of elements to be interleaved orthogonally, slots are cut.

Three RT5880 Duroid substrates having a thickness of 127-µm and two very thin (38 µm) RO2929 bonding films formed the final stack. Lastly, an array of 512 elements is designed with a cross-polarization discrimination higher than 15 dB.

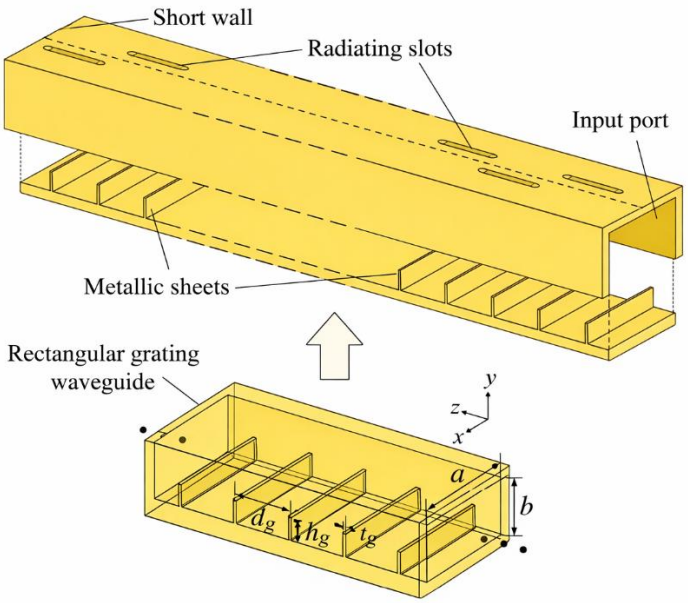

Figure 1.12 Configurations of the rectangular grating waveguide slot array antenna and the rectangular grating waveguide.[92].

Figure 1.12 shows the configuration of the rectangular grating waveguide slot array antenna [92]. Multiple metallic sheets are arranged on the bottom broad wall of this antenna. This antenna performs well at receiving frequencies of 12.25–12.75 GHz. At the transmitting frequencies of 14.0–14.5 GHz, it reduces the realized gain by 14.8–21.3 dB. This shows that the antenna has a filtering response. Performance optimization in terms of impedance and gain bandwidths,

radiation efficiency, structural robustness, and ease of integration into mobile platforms are the aims of each solution.

In [97], a dual linear polarized antenna with high isolation between ports is proposed. The measured result of this antenna shows a 50 dB difference between the co-polarization and cross polarization peaks which indicates its suitability for the array performance. Circularly polarized antennas are also presented by some research [98],[99],[100]. In mobile SATCOM application, circular polarization is useful as under varying orientation and environmental conditions it reduces polarization mismatch losses and enhances link reliability [98],[99],[100].

1.5 Conclusion

In this chapter, the state of the art of several advanced antenna technologies has been reviewed, including planar transmitarrays, PRS-based Fabry–Pérot antennas, ME dipole antennas, and dual polarized arrays. Highly directive beam can be produced by the planar transmitarray through phase compensated frequency selective surfaces while the same can be achieved by the lightweight PRS-based Fabry–Pérot antennas through resonant cavity effects. On the other hand, ME dipole antennas are popular for their wide impedance bandwidth, low cross-polarization and stable radiation patterns, whereas scalable high-performance solutions are provided by the wideband patch arrays. There are some inherent trade-offs between bandwidth, gain, and profile in each approach despite of above-mentioned advantages. These challenges are addressed and solved through novel antenna concepts and design strategies in the following chapters.

2 Theoretical principles

In this chapter, the theory useful for the design of i) planar transmitarray, ii) partial reflecting surface (PRS) based Fabry Perot antenna; iii) magnetoelectric (ME) dipole antenna; iv) artificial magnetic conductor (AMC) and electromagnetic bandgap structure (EBG) is briefly reviewed.

2.1 Model description of transmitarray based on ray tracing approach

Several research works successfully developed the following method, and its accuracy has already established [101],[102],[103],[104],[105]. Figure 2.1 shows the topology of the simplified system. An array of antenna elements models the transmitarray, while a focal point and one radiation pattern specify the feed. In this model, a scattering matrix and two radiation patterns (transmission and reception) are used to describe each array element.

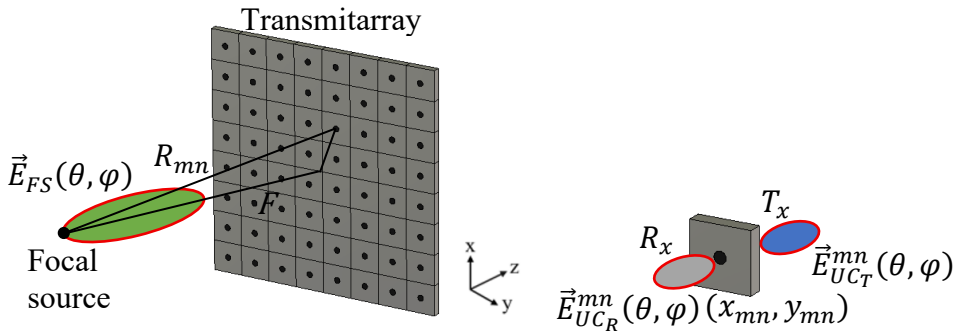

(a) (b)

Figure 2.1 (a) General scheme of the transmitarray antenna using ray tracing technique and (b) unit cell topology, defined by its scattering matrix and two radiation patterns, one in reception and one in transmission [106].

To calculate the radiated field of a given transmitarray with a focal distance F, the incident wave on the transmitarray, $\vec{\alpha}_1^{mn}$ is determined first. The Friis equation is applied between the focal source and each unit-cell as follows [101]:

$$\vec{\alpha}_1^{mn} = \sqrt{P_0}\,\frac{\lambda}{4\pi R_{mn}}\,e^{-j\frac{2\pi R_{mn}}{\lambda}}\left[\vec{E}_{FS}(\theta,\varphi).\vec{E}^{mn}_{UC_R}(\theta,\varphi)\right] \tag{2.1}$$

Where, λ is the wavelength at the frequency of observation and P_0 is the input power of the focal source. The far-field quantities of the focal source and the unit-cell in the reception side are represented by the vectors $\vec{E}_{FS}(\theta,\varphi)$ and $\vec{E}^{mn}_{UC_R}(\theta,\varphi)$ respectively. The spatial phase delay between the feed source and the transmitarray is compensated by each unit-cell to provide a collimating beam. So, the corresponding phase is equal to [104]:

$$\Delta\varphi_{sp} = \frac{2\pi R_{mn}}{\lambda} = \frac{2\pi}{\lambda}\sqrt{({x_{mn}}^2 + {y_{mn}}^2 + F^2)} \tag{2.2}$$

Each unit-cell is located at (x_{mn}, y_{mn}, F) and the feed point represents the center of the reference system. Furthermore, an additional phase component is considered to point the beam at some angle (θ_0, φ_0) in far-field. Finally, the total phase compensation at each unit-cell as per standard antenna array theory [16] is:

$$\psi_{mn} = \Delta\varphi_{sp} - \frac{2\pi}{\lambda}(x_{mn}sin\theta_0 cos\varphi_0 + y_{mn}sin\theta_0 sin\varphi_0) \tag{2.3}$$

So, the design process of the transmitarray provides a targeted value of the phase ψ_{mn} for each unit-cell. Once the total phase distribution is calculated from (2.3), the transmitted wave, $\vec{\beta}_2^{mn}$ at each corresponding unit-cell can be simply found as [106]:

$$\vec{\beta}_2^{mn} = S_{21}^{mn}\vec{\alpha}_1^{mn} \tag{2.4}$$

where S_{21}^{mn} is the transmission coefficient of the corresponding unit-cell. Generally, a few number of distinct phases can be achieved through different unit-cell topologies. As a result, the quantization of the phase distribution is performed, which leads to a gain loss. Normally, eight different unit-cell topologies are employed to minimize the quantization loss. As a result, the phase difference between the neighbouring states becomes 45° in a 3-bit phase resolution system. In this way, the quantization loss can be limited to less than 0.5 dB.

Now, at some distance r,the radiated power density of the transmitarray can be written as [106]:

$$S(\theta,\varphi) = \frac{1}{4\pi r^2}\left|\sum_{m=1}^{M}\sum_{n=1}^{N}\left[\vec{\beta}_2^{mn}\vec{E}_{UCT}^{mn}(\theta,\varphi)\right]\right|^2 \tag{2.5}$$

Consequently, the expression of the antenna directivity is [106]:

$$D(\theta,\varphi) = \frac{S(\theta,\varphi)}{P_0/4\pi r^2} \tag{2.6}$$

Finally, the realized gain of the transmitarray antenna can be calculated as [106]:

$$G(\theta,\varphi) = \eta_{FS}\eta_{SP}D(\theta,\varphi) \tag{2.7}$$

In expression (2.7), η_{SP} is the spillover efficiency and η_{FS} is the efficiency of the focal source. η_{FS} can be expressed as [106]:

$$\eta_{FS} = \frac{P_1}{P_0} \tag{2.8}$$

where P_1 is the source radiated power. Similarly, the spillover efficiency η_{SP} can be found from the ratio of the incident power on the transmitarray P_2, to the source radiated power P_1 [106]:

$$\eta_{SP} = \frac{P_2}{P_1} \tag{2.9}$$

The following sum represents the incident power on the transmitarray P_2 [106]:

$$P_2 = \sum_{m=1}^{M}\sum_{n=1}^{N}|\vec{\alpha}_1^{mn}|^2 \tag{2.10}$$

So, the total transmitted power is equal to [106]:

$$P_3 = \sum_{m=1}^{M} \sum_{n=1}^{N} \left|\vec{\beta}_2^{mn}\right|^2 \tag{2.11}$$

Due to the reflection and dissipation losses introduced by the unit-cells, P_3 is generally less than P_2. The corresponding insertion efficiency is equal to [106]:

$$\eta_{IL} = \frac{P_3}{P_2} \tag{2.12}$$

Hence, the expression of the total efficiency η_{tot} of the transmitarray antenna is [7]:

$$\eta_{tot} = \eta_{FS}\eta_{SP}\eta_{IL} \tag{2.13}$$

A complete power budget estimation can be carried out if all four power quantities are known (P_0, P_1, P_2 and P_3).

2.2 Theoretical analysis of frequency selective surface

A two-port system [31],[107] represents a single-layer with a conducting element as illustrated in Fig. 2.2. It is illuminated from both sides. At the left-side terminal plane, $\vec{E}_1^{+}$and $\vec{E}_1^{-}$are the incident and reflected plane waves, respectively. Also, at the right-side terminal plane, the incident and reflected plane waves are $\vec{E}_2^{+}$and $\vec{E}_2^{-}$, respectively.

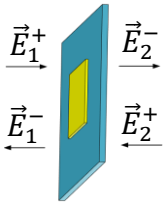

Figure 2.2 Single layer with a conducting element.

Four complex quantities of two port network are related to each other by the following matrix according to the linear two-port networks theory [108]:

$$\begin{bmatrix} E_1^- \\ E_2^- \end{bmatrix} = \begin{bmatrix} \mathrm{S}_{11}\ \mathrm{S}_{12} \\ \mathrm{S}_{21}\ \mathrm{S}_{22} \end{bmatrix} \begin{bmatrix} E_1^+ \\ E_2^+ \end{bmatrix} \tag{2.14}$$

In the expression of (2.14), [S] represents the scattering matrix of the two-port system. To derive the useful features of the [S] matrix of the frequency selective surface (FSS) layer, several assumptions and approximations are adopted.

The following relations are satisfied [108] if the FSS layer is symmetrical and reciprocal:

$$S_{11} = S_{22} \text{ and } S_{12} = S_{21} \tag{2.15}$$

In case of a lossless FSS layer, the following expressions [108] can be written:

$$|S_{11}|^2 + |S_{21}|^2 = 1 \tag{2.16a}$$

$$|S_{12}|^2 + |S_{22}|^2 = 1 \tag{2.16b}$$

$$S_{11}S_{21}^* + S_{21}S_{22}^* = 0 \tag{2.17}$$

Equation (2.17) is updated by substituting Equation (2.15), resulting in:

$$|S_{11}|e^{\,j(\angle S_{11})}|S_{21}|e^{-\,j(\angle S_{21})} + |S_{21}|e^{\,j(\angle S_{21})}|S_{11}|e^{-\,j(\angle S_{11})} = 0$$

$$e^{\,j(\angle S_{11})}e^{-j(\angle S_{21})} + e^{\,j(\angle S_{21})}e^{-j(\angle S_{11})} = 0$$

$$\angle S_{11} - \angle S_{21} = \pm\frac{\pi}{2} \tag{2.18}$$

From equation (2.18), it can be said that, irrespective of the FSS shape and transmission magnitude, the phase difference between the transmitted and reflected waves of any conductor layer is $\pi/2$.

It is also observed that, the higher order harmonics of the FSS layer can be neglected as they are relatively small. Therefore, the Fresnel reflection and transmission coefficients [109] can be written as:

$$S_{21} = 1 + S_{11} \tag{2.19}$$

Equation (2.19) is updated by substituting Equation (2.18), resulting in:

$$|S_{21}|e^{\,j(\angle S_{21})} = 1 + \ |S_{11}|e^{\,j(\angle S_{21}\pm\frac{\pi}{2})}$$

$$|S_{21}| - \ |S_{11}|e^{\pm j\frac{\pi}{2}} = e^{-\,j(\angle S_{21})}$$

$$|S_{21}| \mp j|S_{11}| = cos(\angle S_{21}) - jsin(\angle S_{21}) \tag{2.20}$$

From equation (2.20), the real and imaginary parts can be decomposed into two equations:

$$|S_{21}| = cos(\angle S_{21}) \tag{2.21}$$

$$|S_{11}| = \pm sin(\angle S_{21}) \tag{2.22}$$

2.3 Ray model analysis of partial reflecting surface based Fabry-Pérot antenna

The Fabry Pérot cavity antenna (FPCA) was first modelled by [39], which provides important information about the design of this antenna. Figure 2.3 shows the structure that consists of a radiation source on a conducting plane and a partial reflecting surface (PRS) at a distance D parallel to it. A brief outline of the ray model analysis is made below.

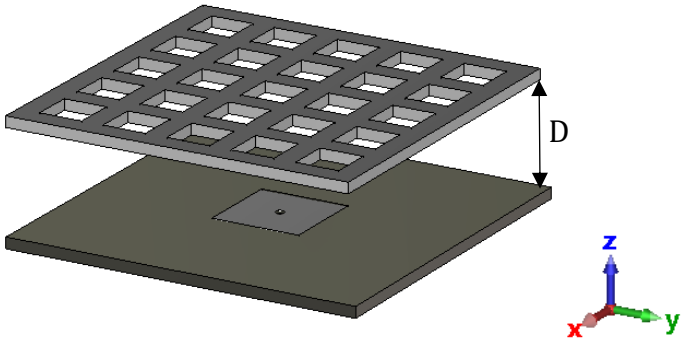

Figure 2.3 Cavity with the selected PRS design [110].

It is assumed that these surfaces are infinite. As a result, the electromagnetic field generated at the source repeatedly reflects between the two surfaces until PRS transmits it fully.

The electric field generated by the source is [110]:

$$\boldsymbol{E}_{\boldsymbol{source}}(\theta) = \boldsymbol{E}_0 f(\theta) \tag{2.23}$$

A lossless, isotropic, and homogeneous behaviour is assumed for the PRS. The reflection coefficient of the PRS is modelled as $R = re^{j\varphi}$. It depends on the angle of incidence θ. A complex amplitude $\boldsymbol{A_n}$ is present in each ray transmitted through the PRS as per the derivation of [39]. The total number of bounces between the PRS and the ground plane is represented by the sub-index n. The first transmitted ray can be expressed as [110]:

$$\boldsymbol{A}_0 = \boldsymbol{E}_0\, f(\theta)\sqrt{(1-R^2)}e^{-jk\frac{D}{cos\theta}} \tag{2.24}$$

where k is the wavenumber. So, the amplitude of any ray at the same wavefront is given by [110]:

$$\boldsymbol{A_n} = \boldsymbol{A}_0\left(-Re^{-jk2Dcos\theta}\right)^n \tag{2.25}$$

Hence, the summation of all these partial rays can produce the total electric field $\boldsymbol{E_T}$. In farfield, its expression is [110]:

$$\boldsymbol{E_T}(\omega,\theta) = \sum_{n=0}^{\infty} \boldsymbol{A_n} = \boldsymbol{E}_0 f(\theta)\frac{\sqrt{(1-R^2)}e^{-jk\frac{D}{cos\theta}}}{1+Re^{-jk2Dcos\theta}} \tag{2.26}$$

Therefore, transmissivity, i.e., the ratio between the cavity radiated power and the source delivered power, can be expressed as [110]:

$$\frac{|\boldsymbol{E_T}(\omega,\theta)|^2}{|\boldsymbol{E}_0|^2} = \frac{(1-r^2)f^2(\theta)}{1+2rcos\left(\varphi+\pi-\frac{4\pi}{\lambda}Dcos\theta\right)+r^2} \tag{2.27}$$

It is noted that the antenna directivity is not the same thing as the transmissivity. Though based on the radiation pattern for each frequency, both are related by a

scale factor. At broadside direction (θ = 0°), the maximum power is obtained at the following condition [110]:

$$\varphi + \pi - \frac{4\pi}{\lambda} D = 0 \tag{2.28}$$

Consequently, the resonance distance D_r between the PRS and the ground plane can be obtained as follows [110]:

$$D_r = \left(\frac{\varphi}{\pi} + 1\right)\frac{\lambda_r}{4} + N\frac{\lambda_r}{2}; \qquad N \in \mathbb{Z} \tag{2.29}$$

Here, the desired cavity resonance wavelength is λ_r. Furthermore, for the resonance distance D_r , the maximum transmissivity can be obtained from the expressions (2.27) and (2.28):

$$\frac{|\boldsymbol{E_T}(\omega, 0^0)|^2}{|\boldsymbol{E_{source}}(\omega, 0^0)|^2} = \frac{1 - r^2}{(1 - r)^2} = \frac{1 + r}{1 - r} \tag{2.30}$$

An expression for the half-power fractional bandwidth is attained [110]:

$$FBW = \frac{\Delta\lambda_{-3dB}}{\lambda_r} = \frac{2}{\varphi + r}\operatorname{acos}\left[1 - \frac{1}{2}\frac{(1 - r)^2}{r}\right] \tag{2.31}$$

The usual resonant structure behaviour can be analysed from these expressions. Increasing the PRS reflectivity enhances the maximum cavity transmissivity, with the shortcoming of a narrower bandwidth.

2.4 Working principle of magnetoelectric (ME) dipole antenna

One of the important parts of this thesis is based on novel design of high gain, wideband ME dipole antennas. These ME dipole antenna features result from the cooperation of the electric dipole mode and magnetic dipole mode. To understand the performance of ME dipole antennas, initially the basic features of electric dipole and magnetic dipole will be discussed in this section.

An electric dipole is known as cost-effective simple structured antenna which is used widely for ease of fabrication [70]. One of the most used dipoles is the half-wavelength dipole [16]. A traditional half-wavelength electric dipole antenna is shown in Figure 2.4.

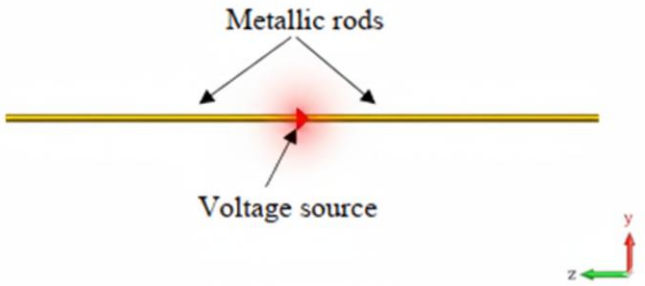

Figure 2.4 The geometry of a half-wavelength dipole [16].

Two metallic rods and a voltage source connecting the two metallic rods forms this antenna. The two open ends of the half-wave-dipole antenna could be considered as open circuit transmission lines if a voltage source is added in the gap

between the two metallic rods. Ideally, the current will be $I = 0\ A$ at the ends of the rods. The current will add in-phase and has the maximum magnitude at the dipole center If the total length of the antenna is about $L = \lambda_0/2$. The radiation pattern of the half-wavelength dipole is shown in Figure 2.5. It shows that the H-plane has an "o" shape, omni-directional and the E-plane has a "inverted-8" shape pattern [16].

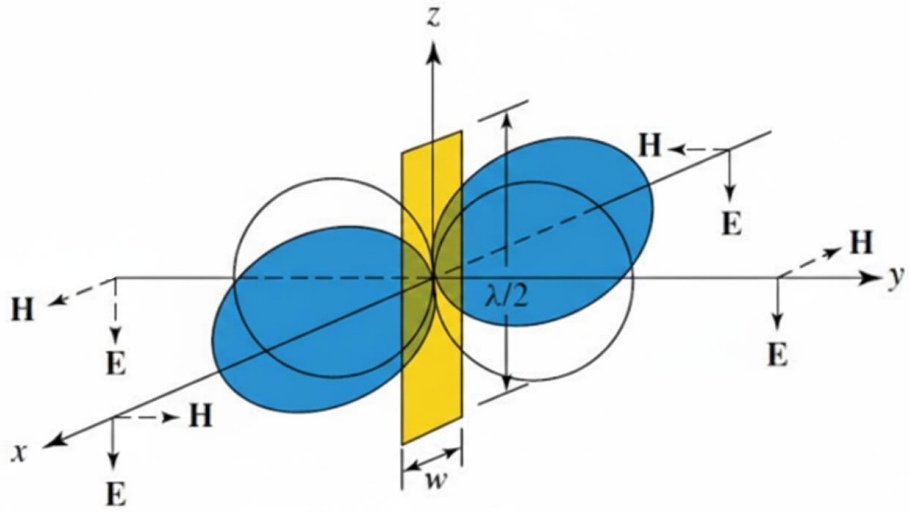

Figure 2.5 The radiation pattern of a half-wave dipole [16].

Another widely used primary antenna is magnetic dipole. A simple slot antenna can be treated as a magnetic dipole. The rectangular slot antenna having the slot length around $L_1 = \lambda_0/2$ is shown in Figure 2.6. A discrete port is placed across the shorted end of the slot antenna. This antenna will generate an linearly polarized omnidirectional radiation pattern if the aperture is excited with an appropriate field.

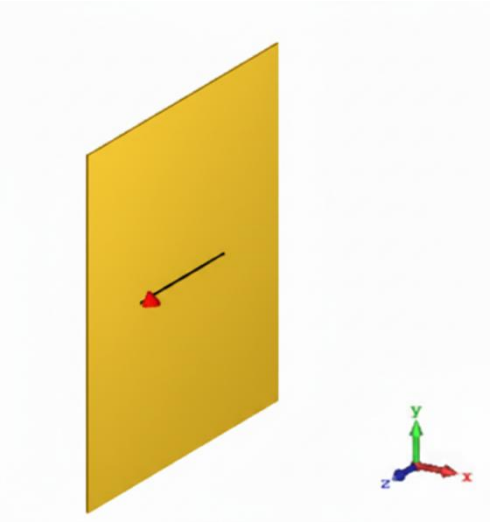

Figure 2.6 The geometry of a magnetic dipole [16].

The radiation pattern of this magnetic dipole antenna (rectangular slot antenna) is shown in Figure 2.7. The H plane has an " inverted-8" shape and the E-plane has an "o" shape omni-directional pattern [16].

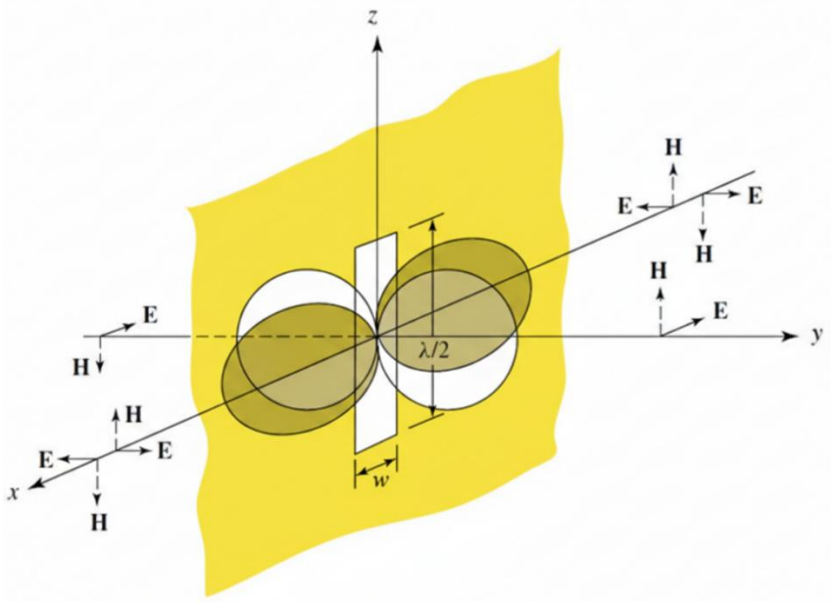

Figure 2.7 Radiation fields of a magnetic dipole [16].

Both the magnetic dipole and the electric dipole produce the same radiation pattern though the E and H-fields are swapped [16]. Consequently, to add up the electric field of both antennas, the magnetic dipole can be placed in a perpendicular position of the electric dipole.

The combination of the radiation patterns of complementary dipoles or the ME dipole antenna is shown in Figure 2.8. In this case, both dipoles are operating at the same frequency. In the broadside direction, the radiating power is added though in the backside, the total power is suppressed [69]. Therefore, 'cardio' shape radiation patterns in E- and H-plane is found due to this combination of complementary dipoles. Furthermore, wide operating bandwidth and stable high

gain could be obtained if the operating frequency of two complementary sources has a slight difference.

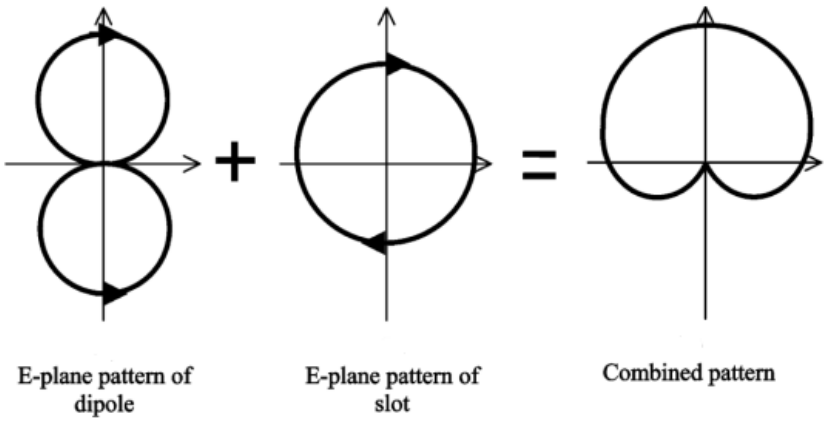

Figure 2.8 E-plane radiation pattern of combined electric dipole and magnetic dipole [69].

2.5 Analytical analysis of artificial magnetic conductor

This section of this chapter reviewed the theory of the artificial magnetic conductor (AMC) to find its resonance condition. Figure 2.9 shows the AMC studied here. The thickness of metal-backed dielectric slab is d, and the relative permittivity is ϵ_r. Patch arrays are placed on the top of the dielectric slab.

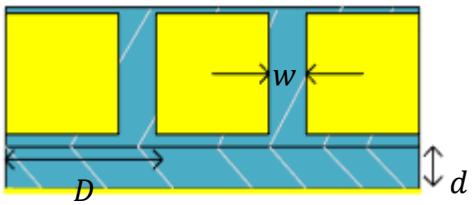

Figure 2.9 A high-impedance structure consisting of an array of patches on top of a metal-backed dielectric slab [111].

As the grid impedance $Z_{g'}$ is in parallel connection with the surface impedance of the grounded dielectric layer Z_S, so the input (surface) impedance can be found from the following equation [111]:

$$Z_i^{-1} = Z_{g'}^{-1} + Z_S^{-1} \tag{2.32}$$

For the oblique incidence, the surface impedance of the grounded dielectric layer Z_S can be written in the dyadic form [111]:

$$\bar{\bar{Z}}_S = \mathrm{j}\omega\mu \frac{\tan(\beta d)}{\beta}\left(\bar{\bar{I}}_t - \frac{\boldsymbol{k_t k_t}}{k^2}\right) \tag{2.33}$$

Here the absolute permeability of the substrate is represented by μ, the propagation constant is represented by $\beta = \sqrt{k^2 - k_t^2}$, the wave number in the substrate material is $k = k_0\sqrt{\epsilon_r}$, and the tangential wave number component is $\boldsymbol{k_t}$.

For both TE/TM polarizations the expression of grid impedance for the capacitive patch array is given bellow:[111]:

$$Z_{g'}^{TM} = -j\,\frac{\eta_{eff}}{2\alpha} \tag{2.34}$$

$$Z_{g'}^{TE} = -j\,\frac{\eta_{eff}}{2\alpha}\frac{1}{\left(1-\frac{k_0^2}{k_{eff}^2}sin^2\theta\right)} \tag{2.35}$$

Here, α is the grid parameter which can be written as [111]:

$$\alpha = \frac{k_{eff}D}{\pi}\ln\left(\frac{1}{sin\frac{\pi w}{2D}}\right)$$

and η_{eff} is the wave impedance of the uniform host medium which is expressed as[111]:

$$\eta_{eff} = \sqrt{\frac{\mu_0}{\epsilon_0\epsilon_{eff}}}$$

and k_{eff} is the wave number of the incident wave vector which is written as follows [111]:

$$k_{eff} = k_0\sqrt{\epsilon_{eff}}$$

From (2.34), (2.35), and (2.33), it can be written:

$$Z_i^{TM} = \frac{\mathrm{j}\omega\mu\frac{\tan(\beta d)}{\beta}cos^2\theta_2}{1-2k_{eff}\alpha\frac{\tan(\beta d)}{\beta}cos^2\theta_2} \tag{2.35}$$

$$Z_i^{TE} = \frac{\mathrm{j}\omega\mu\frac{\tan(\beta d)}{\beta}}{1-2k_{eff}\alpha\frac{\tan(\beta d)}{\beta}\left(1-\frac{2}{\epsilon_r+1}\sin^2\theta\right)} \tag{2.36}$$

Now,θ_2 can be calculated from the angle of incidence θ using the law of refraction as [111]:

$$\theta_2 = \arcsin\left(\frac{sin\theta}{\sqrt{\epsilon_r}}\right)$$

Now the 0° reflection phase condition can be achieved if the capacitive patch array and the inductive grounded substrate resonate. It is possible only if the denominator of the TE/TM input impedance Z_i equals zero resulting the AMC impedance becomes infinite.

As the near-normal incidence is the dominant case, so:

$$\theta = 0 \Rightarrow \cos^2\theta = 1, \sin^2\theta = 0$$

Hence, for both TE and TM cases,

$$2k_{eff}\alpha\frac{\tan(\beta d)}{\beta} = 1$$

This is the AMC resonance condition.

2.6 Analytical analysis of electromagnetic bandgap structure

Electromagnetic band gap (EBG) structures consist of mushroom shaped elements having high surface impedance useful for side lobe reduction of the antenna by suppressing unwanted surface wave. Like as a perfect magnetic conductor (PMC), EBG structure also provides 0º reflection to the electric field parallel to the EBG surface at the resonant frequency. Figure 2.10(a) shows the physical parameters of the EBG cell. The radius of the conducting via is r and

the height of the via is h. The equivalent inductance 'L' and capacitance 'C' are shown in Figure 2.10(b).

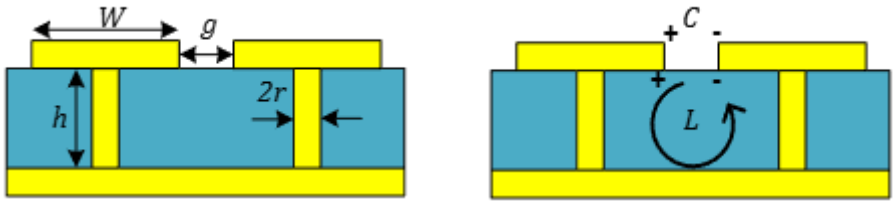

(a) (b)

Figure 2.10 (a) Physical parameters of the EBG cell and (b) Equivalent LC model [112].

Let Z_S be the surface impedance of the EBG structure. The reflection coefficient can be computed as [112]:

$$Z_S = jX \tag{2.37}$$

$$\Gamma = \frac{Z_S - \eta_0}{Z_S + \eta_0} \tag{2.38}$$

$$|\Gamma| = 1 \tag{2.39}$$

$$\angle\Gamma = \pi - 2\tan^{-1}\left(\frac{X}{\eta_0}\right) \tag{2.40}$$

The EBG structure supported bandwidth is estimated by searching those frequencies where the reflection phase $\angle\Gamma$ varies within the range of +90° to −90°. The surface bandwidth condition is written as follows [112]:

$$-90^0 \leq \angle\Gamma \leq +90^0 \tag{2.41}$$

Using Equations 2.40 and 2.41, it can be written as [112]:

$$-\eta_0 \leq \angle X \leq +\eta_0 \tag{2.42}$$

Case I: For $X = \eta_0$, the angular frequency is ω_1. So, the surface impedance [112]:

$$Z_S = j\eta_0 \tag{2.43}$$

$$Z_S = \frac{j\omega_1 L}{1 - \left(\frac{\omega_1}{\omega_0}\right)^2} \tag{2.44}$$

$$\omega_0^2 - \omega_1^2 = \frac{\omega_0^2 L \omega_1}{\eta_0} \tag{2.45}$$

Case II: For $X = -\eta_0$, the angular frequency is ω_2. Similarly,

$$\omega_0^2 - \omega_2^2 = \frac{-\omega_0^2 L \omega_2}{\eta_0} \tag{2.46}$$

From Equations 2.45 and 2.46:

$$BW = \omega_2 - \omega_1 = \frac{\omega_0^2 L}{\eta_0} = \frac{1}{120\pi}\sqrt{\frac{L}{C}} \tag{2.47}$$

The bandwidth, resonant frequency, and the surface impedance are considered as the important parameters of the EBG structure which can be found from the equations (2.37)–(2.47).

2.7 Conclusion

This chapter presents the theoretical study and modelling of the transmitarray antenna using the ray tracing technique. Through this technique, different efficiencies are calculated, which are essential for transmitarray evaluation. Also, the theoretical analysis of a single-layer FSS is performed to analyse its scattering parameter. Next, the working principle of a magnetoelectric dipole antenna is discussed. After that, a PRS-based Fabry Perot cavity antenna is also modelled through ray model analysis, through which the relation between the transmissivity and PRS reflectivity is realized. Finally, AMC and EBG structures are also analysed analytically to find the AMC resonance condition and the bandwidth of the EBG respectively.

3 Dual polarized beam steering transmitarray

The transmitarray is useful for satellite communications and radar applications as it provides lightweight, flat-profile alternative to bulky dishes while enabling high gain. Moreover, for rapid beam pointing, the beam steering capability of a transmitarray is required to control the radiation pattern dynamically. This chapter presents the Ph.D. research related to transmitarray design and fabrication for dual polarized beam steering applications.

3.1 Introduction

Nowadays, directive antennas are quite demanding in high frequency wireless networks as those can enhance the information channel capacity by controlling the beam forming and beam steering. The common application areas of these antennas are 5G networks, wireless power transmission and satellite systems. Among the directive antennas, phased array antennas are studied in different application areas though complex feed networks requirement makes it complicated [113],[114],[115],[116],[117],[118],[119]. Also, prominent losses are expected in these high-gain applications, as the insertion loss and complexity of the feed network increase when the number of radiating elements is high. Furthermore, the employment of numerous phase shifters raises losses and costs. For solving this problem, several studies proposed transmitarray antennas as a promising alternative to conventional phased array antennas [120],[121],[122],[123],

[124],[125],[126],[127],[128]. Generally, a metasurface capable of controlling the phase and amplitude of the incident signal and a single feed antenna forms a transmitarray (TA). For effective beam forming, a TA system can be used as the metasurface of this system can control 360° transmission phase with low loss transmission. The uses of active elements such as varactors, diodes, MEMS, and liquid crystals (LC) in metasurface are common for steering the beam in a desired direction, though the fabrication complexity and losses increase due to these electronic components [129],[130],[131],[132]. Another way of doing beam steering is the mechanical movement, i.e. the position shifting of the feed [133],[134],[135]. Two essential factors determine the performance of the TA. One is the focal distance (F) of the metasurface, and the other is the size of the metasurface (D). The power transfer to the metasurface is influenced by the ratio of F/D [136]. Consequently, this ration also controls the product of the spillover and taper efficiency. To increase the spillover efficiency, the size of the metasurface (D) can be enlarged though it makes the metasurface bulky. On the other hand, the taper efficiency can be enhanced by increasing the focal distance (F) with a penalty of spillover efficiency reduction. The design of phase gradient metasurface can be useful for low-profile beam-steering TA antenna. For example, beam-steering TAs with low-profile architecture were developed with multiple feed horn antennas for 5G mm-wave communication [137],[138],[139],[140],[141]. The dual-polarized operation is another important feature of next-generation wireless communication systems as it enhances the overall system capacity and increases the reliability of the radio link. Several researchers work on dual-polarized TAs having continuous phase tuning based on dual-frequency selective surface layers [142],[143],[144],[145],[146],the cascade of three metallic layers [147],[148],[149],[150], and quantized phase compensation [151],[152],[153],[154],[155].

The design of a novel monolithic unit cell is illustrated in this chapter. It attains dual-polarized operation with low profile architecture, minimal transmission loss and 3-bit phase compensation. These characteristics help to attain higher gain, lower side lobe levels and scan loss in comparison with the state of the art. The unit cell is intrinsically suitable for dual polarized radiation as it is based on a novel symmetrical geometry. To understand the working principle, an equivalent circuit model (ECM) of the proposed UC is then developed. Next, that model is used to derive the scattering parameters. A good match between the full-3D numerical simulated results and the ECM model derived results is monitored. A proof-of-principle test TA is designed and fabricated based on the developed UC. The expected gain and side lobe levels are observed after the characterization of the TA. Besides, the proposed TA has potential for advanced beam-forming applications as it enables efficient beam steering over tens of angular degrees with minimal scan loss.

The organization of this chapter is as follows: after the Introduction, the UC design and its simulated performance are discussed in Section 3.2. The ECM development and the result comparison of the corresponding scattering parameters with those calculated via the full-3D numerical simulation are illustrated in Section 3.3. Section 3.4 figures the TA antenna design procedure, while Section 3.5 compares the simulated and the experimental results. The comparison of the performance of the proposed TA with recent research works is shown in Section 3.6. Lastly, Section 3.7 specifies the concluding remarks.

3.2 Unit cell design of the transmitarray

The detailed design of a novel UC is exhibited in this section. Figure 3.1 illustrates the top and side view of the proposed UC, the yellow color representing the metal and the blue color is for the substrate [156]. The UC comprised of three identical layers used for the phase compensation of the source incident ray. For allowing the dual polarization operation, a symmetric geometry is chosen intentionally. A metal ring, with an outer radius R_1 and inner radius R_2, and an inner circle of radius R_3 constitute the metal layer.

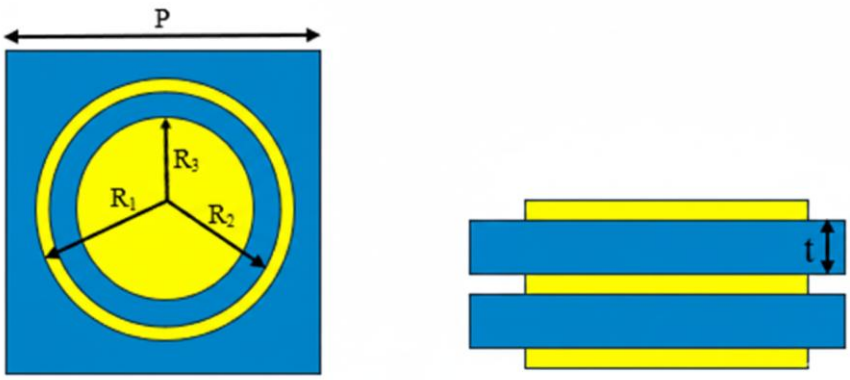

Figure 3.1 (a) Top and (b) side views of proposed monolithic UC, consisting of three identical metal layers. Yellow part represents metal, and blue part is substrate [156].

Table 3.1 listed the ranges for searching the optimized dimensions of this design. After the preliminary simulations, they are found. To achieve 3-bit phase with low transmission loss, eight UCs are designed by changing the values of R_1, R_2, and R_3. The corresponding transmission magnitude and phase with the specific dimensions of the eight UCs are listed in Table 3.2.

TABLE 3.1 RANGE FOR GEOMETRICAL PARAMETER OPTIMIZATION [156].

Parameter	**Symbol**	**Value (mm)**
Periodicity	P	8.650
Outer radius	R_1	3.800–4.325
Inner radius	R_2	3.700–4.225
Inner circle radius	R_3	2.550–4.110
Thickness	T	1.575

TABLE 3.2 GEOMETRICAL DIMENSIONS FOR 3-BIT PHASES AND CORRESPONDING MAGNITUDES AT THE FREQUENCY f_0 = 12 GHz [156].

UC No.	f_0 (GHz)	R_1 (mm)	R_2 (mm)	R_3 (mm)	$\lvert S_{2,1}\rvert$ (dB)	$\angle S_{2,1}$ (deg)
1	12	4.325	4.225	4.110	−0.860	46.0
2	12	4.325	4.225	4.070	−0.580	89.0
3	12	4.325	4.225	3.960	−0.920	136.0
4	12	4.200	4.100	3.830	−0.200	179.3
5	12	4.250	4.150	3.600	−0.710	225.0
6	12	4.325	4.200	3.070	−1.230	270.6
7	12	4.200	4.100	2.630	−0.170	314.0
8	12	4.325	4.225	4.110	−1.160	359.6

Rogers RT/duroid 5880 (ε_r = 2.2, tanδ = 0.0009) is used as the substrate with a thickness of t = 1.575 mm (0.063λ_0) whereas the thickness of the metal is 35 μm. The UC periodicity is P = 8.65 mm (0.346λ_0). The central wavelength at the frequency f_0 = 12 GHz is λ_0 = 25 mm.

Equation (1) shows the expression of an incident wave's electric field with arbitrary linear polarization on the UC [157]:

$$\overline{E}_{inc} = E_x\bar{x} + E_y\bar{y} \tag{3.1}$$

Here the incident electric field components along the orthogonal linear polarizations are E_x and E_y. The following 2 × 2 transmission matrix shows the relation between the input and output fields for each UC [157]:

$$\begin{pmatrix} \overline{E}_{x,out} \\ \overline{E}_{y,out} \end{pmatrix} = \begin{pmatrix} T_{xx} & T_{xy} \\ T_{yx} & T_{yy} \end{pmatrix} \begin{pmatrix} \overline{E}_{x,in} \\ \overline{E}_{y,in} \end{pmatrix} \tag{3.2}$$

Here, the co-polar and cross-polar transmission coefficients are T_{xx}, T_{yy} and T_{xy}, T_{yx} correspondingly. The dual-polarized operation can be expected if the off-diagonal terms T_{xy}, T_{yx} are null.

So, the required transmission matrix T for dual-polarized operation is [157]:

$$T = \begin{pmatrix} |T_{xx}|e^{j\angle T_{xx}} & 0 \\ 0 & |T_{yy}|e^{j\angle T_{yy}} \end{pmatrix} \tag{3.3}$$

Here, the phase shifts applied to x- and y-polarized waves are $\angle T_{xx}$ and $\angle T_{yy}$ respectively.

For each of the eight UCs, the magnitude (T_{xx} and T_{yy}), and the phase ($\angle T_{xx}$ and $\angle T_{yy}$), of the transmission coefficient for co-polarized signal components xx or yy, respectively, are simulated by the CST Studio suite software. To define the transmission behaviour between ports 1 and 2, these coefficients are used to represent the scattering parameter's magnitude $|S_{2,1}|$ and phase $\angle S_{2,1}$, correspondingly. Furthermore, the x- and y-polarized transmission coefficients are identical due to the symmetry. To simulate an infinite array, UC boundary conditions are

applied along the x and y directions, in Floquet port configuration, as illustrated in Figure 3.2. The open boundaries are imposed along the z direction. For exciting plane waves, the Floquet ports along the *z*-axis are used.

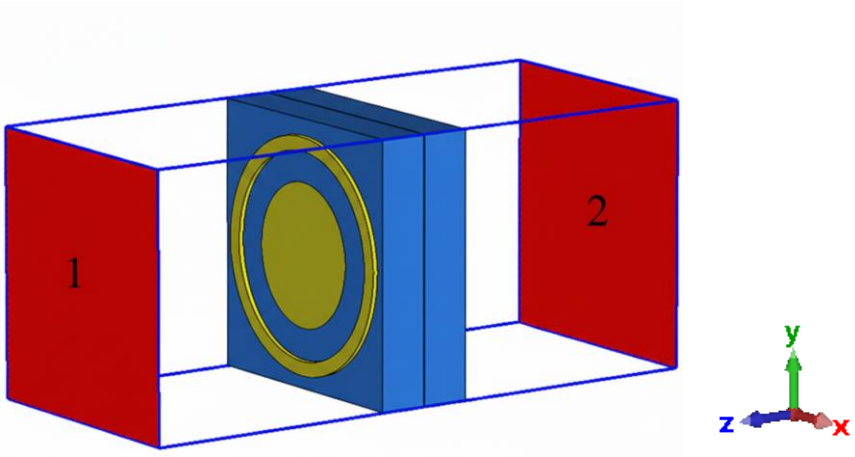

Figure 3.2 UC simulation by assigning Floquet ports [156].

Figure 3.3(a) shows the simulated results of transmission magnitude $|S_{2,1}|$ for the different UC_i. The highest transmission loss is $\alpha_T = 1.23$ dB, found at UC_6, obtained at the frequency $f_0 = 12$ GHz. Eight UCs cover the 3-bit phases required for co-polarized components at the frequency f_0, shown in Figure 3.3(b). Furthermore, investigating the performance of the UC for different incidence angles θ is also important for TA design. For different incidence angles θ, the transmission magnitude and phase of the co-polarized components are simulated for this purpose.

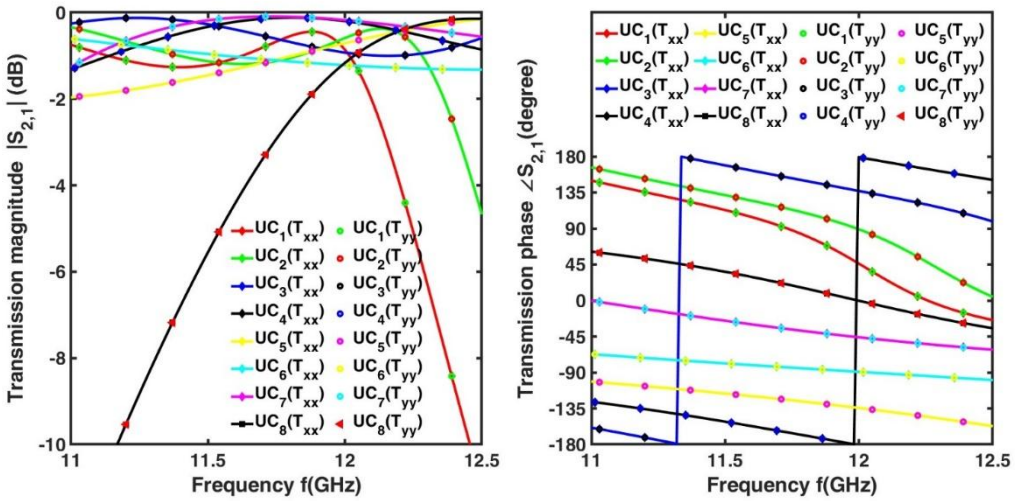

(a) (b)

Figure 3.3 (a) Transmission magnitude $|S_{2,1}|$ as a function of the frequency f for co-polarized components; (b) Transmission phase $\angle S_{2,1}$ as a function of the frequency f for co-polarized components [156].

For an incidence angle $\theta = 30°$, the transmission loss α_T for co-polarized components is less than 1.9 dB illustrated in Figure 3.4(a). For co-polarized components, the transmission phases $\angle T_{xx}$ and $\angle T_{yy}$ at $f_0 = 12$ GHz are shown in Figure 3.4(b). The transmission phase obtained at $\theta = 30°$ is close to the value obtained at $\theta = 0°$ with a maximum simulated deviation of about $\triangle P = 20°$.

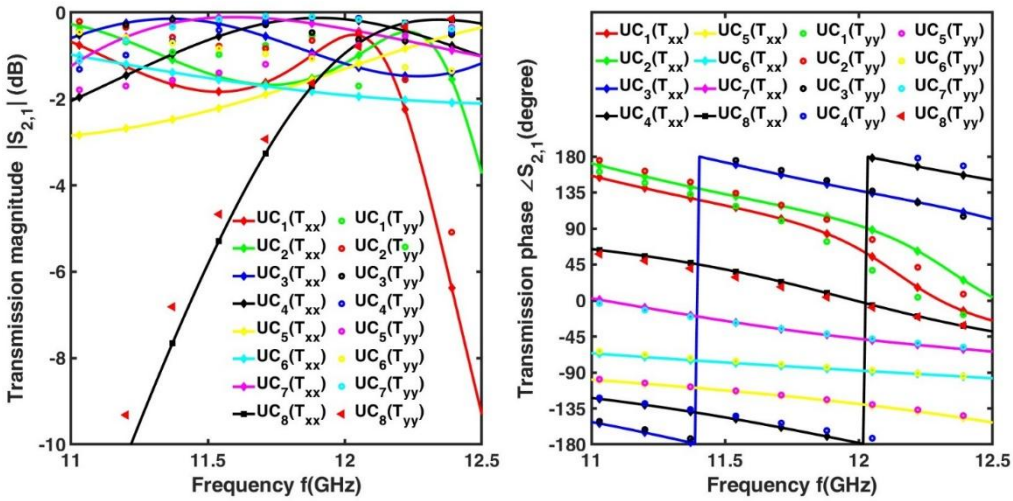

(a) (b)

Figure 3.4 (a) Transmission magnitude $|S_{2,1}|$ as a function of frequency f for co-polarized components for θ = 30°; (b) Transmission phase $\angle S_{2,1}$ as a function of frequency f for co-polarized components for θ = 30°[156].

The UCs transmit the incidence ray in the accurate direction with low transmission loss in all cases. The investigation is also carried out about the behavior of these UCs for cross-polarized components xy, yx. Figure 3.5 shows the transmission magnitude T_{xy} and T_{yx} of all UCs, as a function of the frequency f for the cross-polarized components. The cross-polarized transmission is remarkably low, peaking at $T_{max} = -51$ dB across all evaluated components.

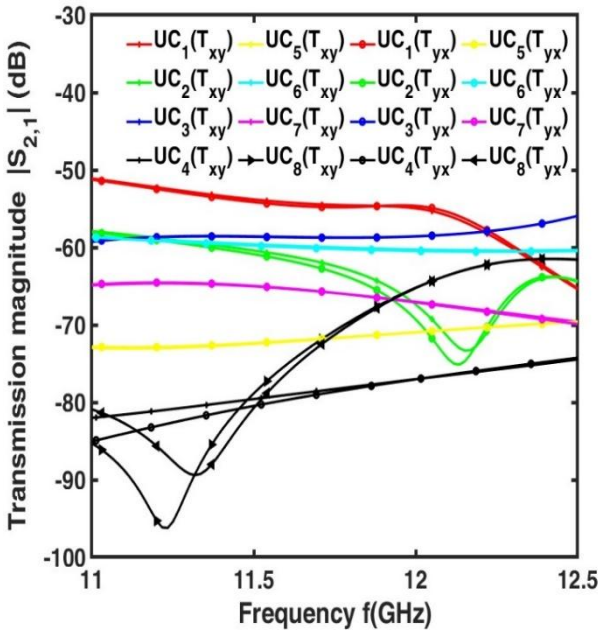

Figure 3.5 Transmission magnitude $|S_{2,1}|$ as a function of frequency f for cross-polarized components [156].

3.3 Equivalent Circuit Analysis of the UC

In order to understand the operation of the UC, the ECM is developed using the same procedure developed in the research [158]. After that, the Advanced Design System (ADS) software is used to simulate the ECM. The ADS software provides the simulated S parameter values which are compared with CST simu-

lated corresponding results. Two adjacent UCs and the ECM are shown in Figure 3.6.

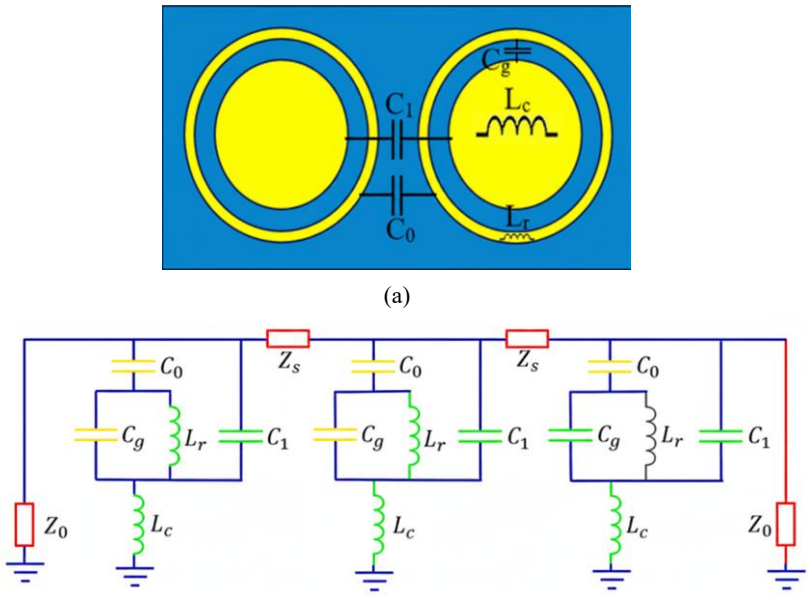

Figure 3.6 (a) Top layer of two adjacent UCs and (b) ECM of a single UC [156].

The discrete components such as capacitors or inductors are used to represent the inductive and the capacitive behavior of the different parts of the metallic pattern, derived from the UC geometry. For example, inductors L_c and L_r represent the inductances of the inner circular metal portion and the outer ring, correspondingly. The capacitor C_g is used to represent the gap between the metal circle and the outer ring while C_1 represents the capacitance formed between the metallic circles of two adjacent cells. In a similar way, C_0 corresponds to the capacitance formed between the outer metal rings of two adjacent cells. The

transmission line theory is used to model the substrate. The model utilize a transmission line with impedance of $Z_S = Z_0/\sqrt{\varepsilon_r} = 255\ \Omega$, where $Z_0 = 377\ \Omega$ and $\varepsilon_r = 2.2$ denote is the free space characteristic impedance and the substrate's relative permittivity, respectively. Z_0 is the characteristic impedance of free space and Z_s represents the substrate impedance. Capacitance and inductance values remain consistent across all three metal layers as all the metal layers are identical. For computing the circuit component values of ECM, UC_6 is chosen. The outer radius of the metal ring, the inner radius of the metal ring, and the radius of the inner circle, are R_1 = 4.325 mm, R_2 = 4.20 mm, and R_3 = 3.07 mm respectively for UC_6, having $\angle S_{2,1} = 270°$ transmission. Table 3.3 shows the circuit component values of the ECM for UC_6.

TABLE 3.3 VALUES OF CIRCUIT COMPONENTS OF UC_6 ECM [156].

Parameter	Value	Unit
C_0	0.323	pF
C_g	0.042	pF
C_1	0.019	pF
L_r	3.727	nH
L_c	1.729	nH

Gradient-based optimization method is used to compute these values by the ADS software. By tuning the values of the circuit components this optimization match the magnitude $|S_{2,1}|$, and phase $\angle S_{2,1}$ values of the scattering parameters with the respective simulated result obtained by the CST at the corresponding frequencies

f. The values of the capacitors and the inductors mainly determine the transmission phases of the UC. A comparison between CST simulation and ECM calculation regarding the magnitude and phase values of scattering parameter $S_{2,1}$ of UC_6 is illustrated in Figure 3.7. An excellent match is observed.

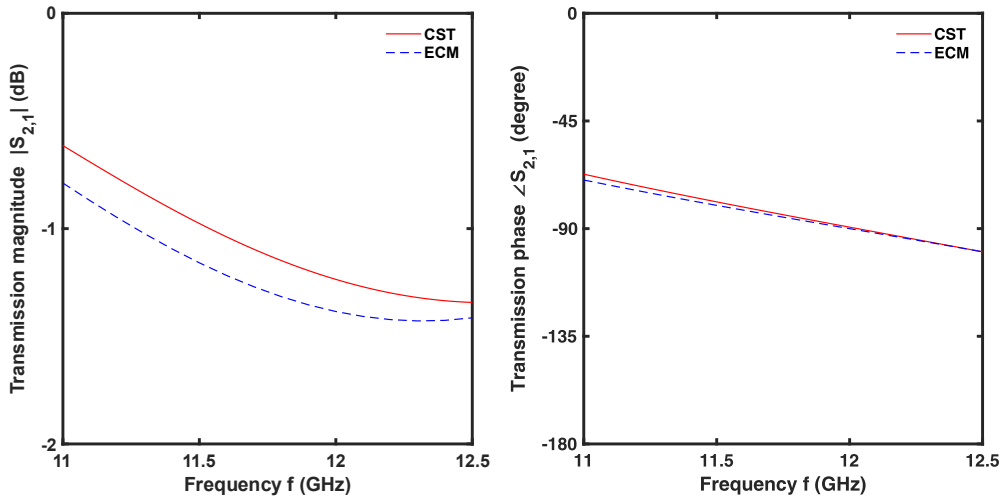

(a) (b)

Figure 3.7 Transmission magnitude $|S_{2,1}|$ and transmission phase $\angle S_{2,1}$ of UC_6 as a function of frequency f, obtained by CST and ECM simulation. (a) Transmission magnitude; (b) transmission phase [156].

3.4 The TA Antenna

For this design, a maximum D size of 200 mm was considered and a focal length-to-diameter ratio (F/D) of 0.6 was chosen. a suitable feed antenna was selected

based on this requirement. Specifically, a 2 × 2 array antenna [159] based on substrate integrated waveguide (SIW) was used. Figure 3.8 shows the feed antenna array. Two Rogers RT/duroid 5880 substrates (ε_r = 2.2, tanδ = 0.0009) form this array. The thicknesses of the first and second substrates are T_1 = 0.381 mm, and T_2 = 1.575 mm, respectively.

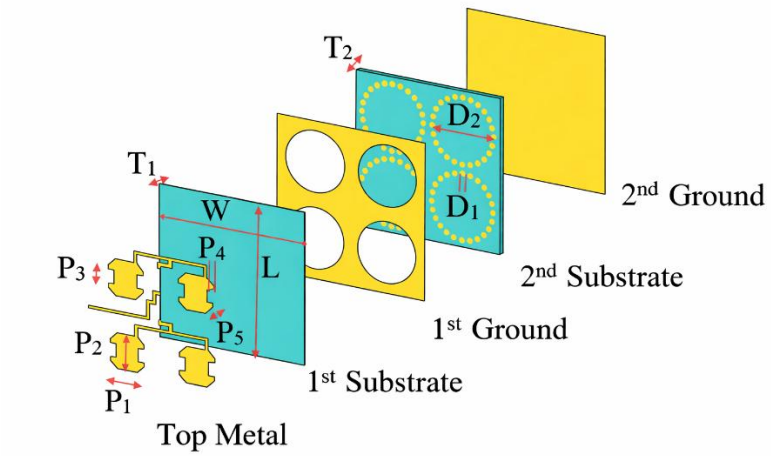

Figure 3.8 Feed antenna array stack up with dimensions (P_1 = 7.70 mm, P_2 = 7.70 mm, P_3 = 2.75 mm, P_4 = 1.44 mm, P_5 = 2.18 mm, D_1 = 0.62 mm, D_2 = 15.05 mm, T_1 = 0.381 mm, T_2 = 1.575 mm, L = 35 mm, W = 35 mm); metal portion and substrate 1 and 2 are represented by yellow and blue colors, respectively.

The feed antenna array has a dimension of L = 35 mm and a width of W = 35 mm. The vias connecting both grounds have a diameter of D_1 = 0.62 mm. The diameter of the circular slot in the first ground is D_2 = 15.05 mm. Figure 3.8 shows the dimensions of the patch. The width and length of the patch are P_1 =

7.7 mm, P_2 = 7.7 mm respectively. The dimensions regarding lateral and corner slot in the patch are P_3 = 2.75 mm, P_4 = 1.44 mm, and P_5 = 2.18 mm, respectively. Particularly, the SIW based 2 × 2 antenna array in [159] is selected as feed because the chosen F/D ratio and the target D size of the TA align with the −10 dB beamwidth which is of approximately 66°. The array operates over a BW = 2.5 GHz frequency span from f_L = 10 GHz to f_H = 12.5 GHz, offering an impedance bandwidth of BW_z = 20.83% while delivering a maximum gain of G_{f0} = 12.93 dB at 12 GHz and G_{f1} = 12.83 dB at 12.4 GHz, respectively [159].

By using the proposed UC, a 484 (22 × 22) element based TA is designed and implemented. The width of the TA is D = 22 × 8.65 mm = 190.3 mm and the focal distance is F = 0.6 × D = 114.18 mm are finalized as per the design approach. For beam forming and beam steering in the desired direction, the transmission phase of the UC of the TA needs to be adjusted. The spatial phase delay, which is introduced due to the distance, d_p, between the feed antenna and the corresponding p^{th} UC (shown also in Figure 3.9(a)) is compensated by the phase adjustment of the UC. The required phase shift across the TA for optimal beam forming in the targeted direction, (θ_0,φ_0), is computed as follows. For the p^{th} UC, the phase of the transmitted electric field is [160]:

$$\psi(x_P, y_P) = -k_0 x_P \sin\theta_0 \cos\varphi_0 - k_0 y_P \sin\theta_0 \sin\varphi_0 \tag{3.4}$$

Here k_0 is the free space wavenumbers and (x_P, y_P) is the coordinate of the p^{th} UC. By summating the phase of the incident electric field and the transmission phase shift of the UC, the total phase of the transmitted electric field of pth UC can be calculated [160]:

$$\psi(x_P, y_P) = -k_0 d_P + \psi_n(x_P, y_P) \tag{3.5}$$

The distance between any surface point of TA having the coordinates (x_P,y_P,z_P) and the feed point having the coordinates (x_f,y_f,z_f) is represented by d_P. The expression of d_P is [160]:

$$d_P = \sqrt{(x_P - x_f)^2 + (y_P - y_f)^2 + (z_p - z_f)^2} \tag{3.6}$$

Ultimately, the Equations (4) and (5) are used to calculate the required phase shift ψ_n for the generic UC of the planar TA, located at (x_P,y_P,z_P) [161]:

$$\psi_n = k_0(d_P - (x_P \sin\theta_0 \cos\varphi_0 + y_P \sin\theta_0 \sin\varphi_0)) \tag{3.7}$$

The following expression quantifies the 3-bit phase compensation:

$$\psi_n = \begin{cases} 0°, & 0° \le \psi_n < 45° \\ 45°, & 45° \le \psi_n < 90° \\ 90°, & 90° \le \psi_n < 135° \\ 135°, & 135° \le \psi_n < 180° \\ 180°, & 180° \le \psi_n < 225° \\ 225°, & 225° \le \psi_n < 270° \\ 270°, & 270° \le \psi_n < 315° \\ 315°, & 315° \le \psi_n < 360° \end{cases} \tag{3.8}$$

To calculate the 3-bit phase distribution of the TA for a focal distance of F = 114.18 mm, a home-made software is used. For directing the beam in broadside direction $(\theta_0,\varphi_0) = (0°,0°)$, the required phase compensation is shown in Figure 3.9(b). Different transmission phases of the UCs are indicated by the distinct colors in the colorimetric scale.

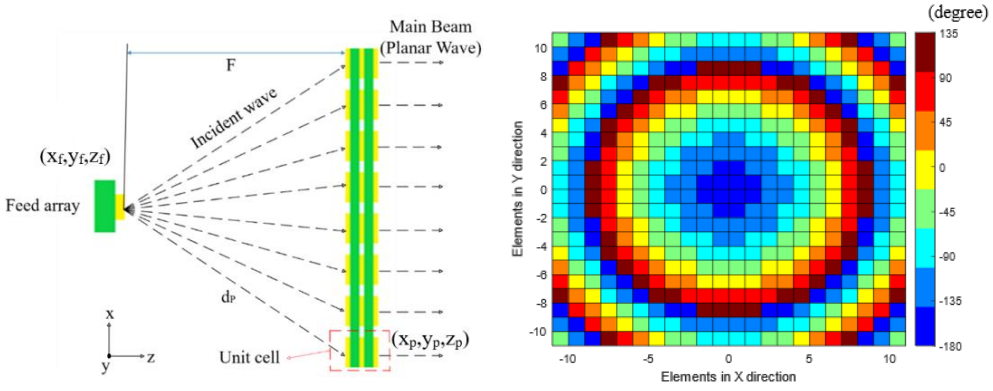

(a) (b)

Figure 3.9 (a) Ray transmission through TA; (b) phase compensation obtained at $f_0 = 12$ GHz for focal distance F to diameter D ratio of 0.6 [156].

3.5 Simulation and Experimental Results

The previously described design procedure of the TA does not consider the phase discretization, the feed's primary pattern, UC's mutual coupling or transmission losses. Full wave simulations with CST have been carried out to accurately assess these effects. The TA is fabricated and characterized. The fabricated prototype and the measurement setup in the anechoic chamber is illustrated in Figure 3.10.

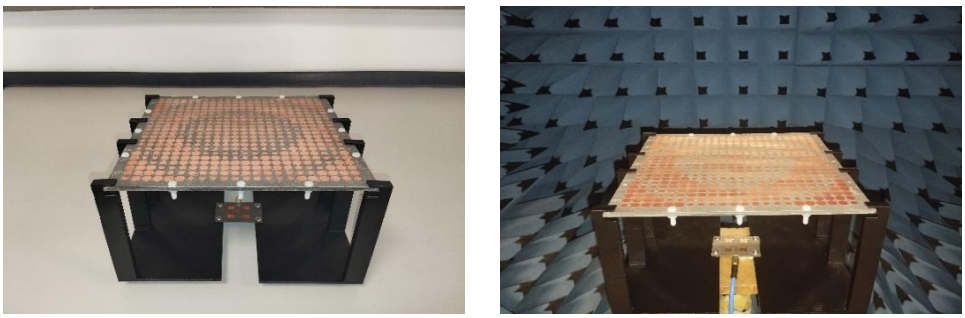

(a) (b)

Figure 3.10 (a) Fabricated prototype with a support structure; (b) measurement setup in anechoic chamber [156].

The difference between simulated and measured peak gain of the feed antenna along with the measured aperture efficiency is highlighted in Figure 3.11. From the Figure 3.11, it is observed that, at f_0 = 12 GHz, the measured peak gain is G_{m0} = 21 dB, whereas the simulated realized peak gain is G_{s0} = 23.35 dB. The measured and simulated peak gain of this TA are G_{m1} = 19.97 dB and G_{s1} = 22.46 dB, respectively at f_1 = 12.4 GHz. The aperture efficiency is η_0 = 17% and η_1 = 13% for f_0 = 12 GHz and f_1 = 12.4 GHz, respectively though the maximum value of the aperture efficiency is η_{max} = 19% found at f_2 = 11.2 GHz. The 1-dB gain bandwidth is found to be BW_g = 10.8%, ranging from f_G = 11.1 GHz to f_1 = 12.4 GHz. For E and H plane, the radiation pattern at f_0 = 12 GHz and f_1 = 12.4 GHz, respectively are shown in Figure 3.12. The difference between the simulated and measured peak gains at f_0 = 12 GHz and f_1 = 12.4 GHz are $\triangle G_0$ = 2.35 dB and $\triangle G_1$ = 2.03 dB for both E and H plane, respectively. Due to thin air layer in between the substrates that have not been bonded together with prepreg, larger insertion loss, and other fabrication tolerances ascribe this deviation. It is also

observed that, at f_0 = 12 GHz and f_1 = 12.4 GHz the measured peak side lobe levels are SLL_0 = −20.8 dB and SLL_1 = −18.5 dB, correspondingly.

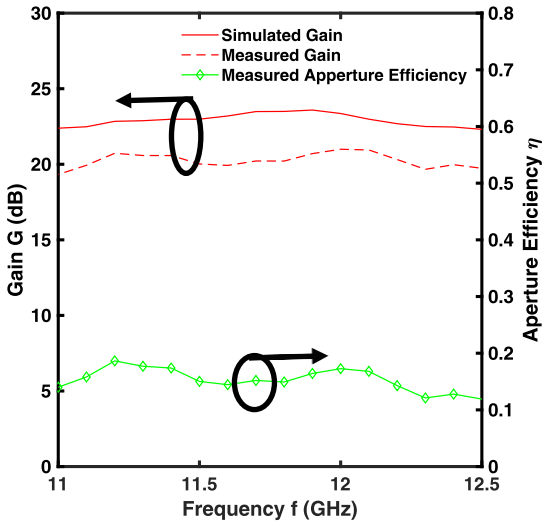

Figure 3.11 Simulated and measured maximum gain and measured aperture efficiency of TA antenna [156].

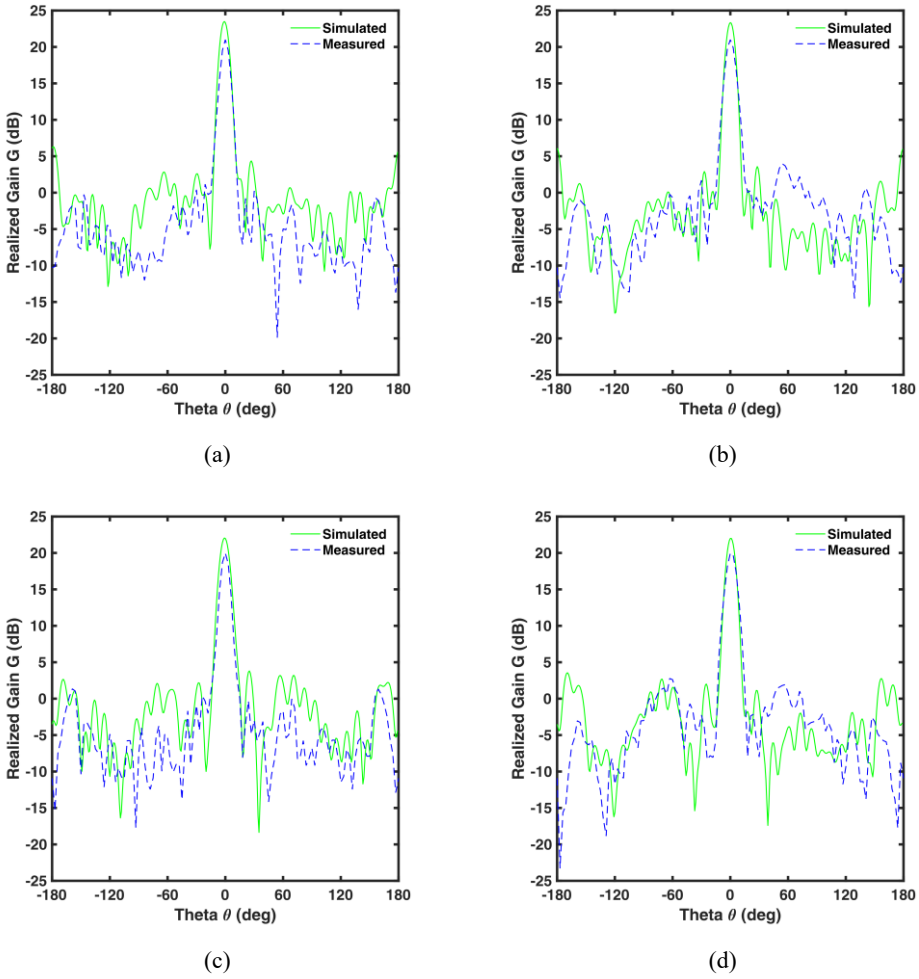

Figure 3.12 Simulated and measured realized gain of TA antenna. (a) E plane at f_0 = 12 GHz; (b) H plane at f_0 = 12 GHz; (c) E plane at f_1 = 12.4 GHz; (d) H plane at f_1 = 12.4 GHz [156].

Several simulations have been performed to evaluate the effects of the fabrication tolerances. Specifically, geometrical changes are performed in all the optimized cells, by increasing of external radius values $\Delta R_1 = 7.5$ µm and a decreasing of internal radius values $\Delta R_2 = -7.5$ µm results a variation of $\Delta G_{s0} = -0.5$ dB in the obtained gain in broadside direction. Besides, the position of the feed antenna array is also varied, i.e., along the z direction, the displacement of the focal distance F of the feed antenna has been changed. The maximum gain is reduced of $G_{s0} = -0.3$ dB and the main beam direction tilts of about $\Delta\theta = -1°$, for a variation of $\Delta F = \pm 4$ mm. It is worth mentioning that, the substrates are deemed completely adherent in the design. The influence of an air-gap with a thickness $t_a = 50$ µm between substrates in the unit cell has been investigated, since Teflon screws are used after the prototype fabrication to assemble the substrate layers of TA. It is noted that, a transmission coefficient variation $\Delta S_{2,1} = -0.12$ dB and phase shifting variation of $\Delta\phi = 1.3°$ with a gain variation of approximately $\Delta G_{s0} = -0.6$ dB in broadside direction is obtained. An ultraviolet laser writing equipment named LPKF Protolaser U3, is employed to fabricate the prototype as it has a scanning beam resolution of SBR = 2 µm, allowing a very good fabrication tolerance. The conducted investigation shows that the reproducibility can be increased by placing a more precise mechanical positioner of the feed antenna and considering a prepreg sheet to assemble the substrates.

Still, low profile TAs can experience a low aperture efficiency, as reported in [162],[163],[164],[165]. Furthermore, the reason for obtaining limited aperture efficiency can be the unmodeled fabrication imperfections. One way of improving aperture efficiency is to employ better amplitude–phase balance by reducing loss mechanisms through optimization strategy such as UC geometry refinement.

Next, the performance of TA beam-steering is examined by shifting the 2 × 2 SIW-based patch antenna array. A feed-shifting length (FSL) of 65 mm is applied to shift the feed antenna along both the positive and negative directions of the x-axis as shown in Figure 3.9(a). Figures 3.13 and 3.14 shows the plots of the farfield gain patterns at f_0 = 12 GHz and f_1 = 12.4 GHz, respectively for the feed coordinates (x,y) = (0 mm,0 mm); (x,y) = (+26 mm,0 mm); (x,y) = (+45 mm,0 mm); (x,y) = (+65 mm,0 mm); (x,y) = (−26 mm,0 mm); (x,y) = (−45 mm,0 mm); (x,y) = (−65 mm,0 mm). Excellent qualitative agreement is observed between the simulated and measured patterns. It is noted that, the maximum beam-steering angle $\gamma_{max} = \pm 30°$ is achieved.

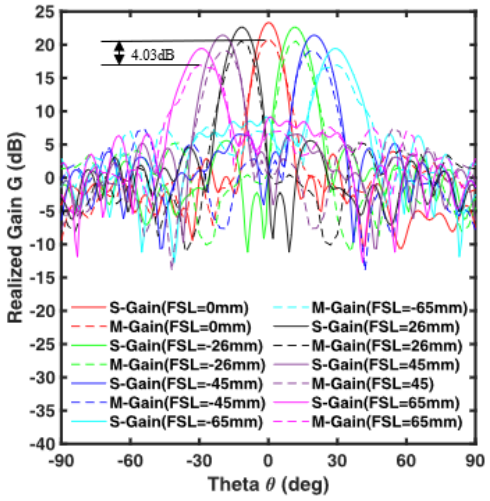

Figure 3.13 Simulated (solid lines) and measured (dashed lines) beam-steering performance at f_0 = 12 GHz [156].

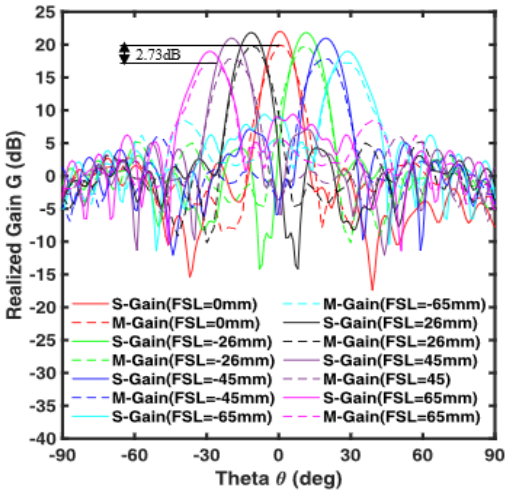

Figure 3.14 Simulated (solid lines) and measured (dashed lines) beam-steering performance at $f_0 = 12$ GHz [156].

But the simulated gain is slightly higher than the measured one in every case, as similar as observed and discussed for the broadside pointing direction previously. Likely, fabrication errors are attributed to this disagreement. For instance, in some UCs, the width of the circular ring is $R_1–R_2 = 0.1$ mm which requires a tight tolerance. The simulated scan losses are $\triangle G_{SSL0} = 3.9$ dB and $\triangle G_{SSL1} = 3.03$ dB for $\gamma_{max} = \pm 30°$ beam steering at $f_0 = 12$ GHz and $f_1 = 12.4$ GHz, respectively. Though the measured scan loss for $\gamma_{max} = \pm 30°$ steering is $\triangle G_{MSL0} = 4.03$ dB at $f_0 = 12$ GHz and $\triangle G_{MSL1} = 2.73$ dB at $f_1 = 12.4$ GHz respectively. Furthermore, during beam steering operation, the actual position of the feed antenna in the experiment is slightly changed regarding the simulated one. As a result, the

measured gain is found to be slightly lower than the simulated gain. Besides, during simulation, the air gap between the substrates is not modeled, which contributes to the difference between the simulated and measured scan loss. It can be inferred that, the TA provides a higher gain enhancement at f_0 = 12 GHz, compared to its performance at f_1 = 12.4 GHz. Though, the latter frequency demonstrates superior performance in terms of scan loss ($\triangle$G) with respect to beam steering capability. In case of measurement, the feed antenna array is only shifted along the x axis for beam steering operation. Due to the symmetrical nature of this TA, similar results are obtained by shifting the feed antenna along the y axis.

Mechanical feed displacement for beam steering works well in this work though it is not feasible for some applications. To overcome the limitations associated with mechanical feed displacement, the integration of reconfigurable elements, such as varactor diodes or tunable materials, within the UC architecture can be explored for beam steering operation. For electronic beam steering, dynamic phase control across the aperture is necessary. Incorporation of electronic tunable components can be a good solution. Moreover, better control of polarization, adaptive beam shaping, and multi-beam operation can be achieved by this evolution to make the TA suitable for real-world applications.

3.6 Comparison with Other Works

Evaluation of the performance of proposed TA against previously reported works is done, as summarized in Table 4. The proposed TA has a thickness of ρ = $0.126\lambda_{0,}$ which is lower in comparison with other works

[162],[163],[164],[165]. Three layers-based TA having the reduced array size of $A = 57.9\lambda_0^2$ indicates it low profile features [162],[164],[166]. Other important characteristics of this proposed TA are improved robustness, compactness, and ease of fabrication as there is no need of an air gap between the substrates in this design. Another indication of compactness of this TA is the lower F/D = 0.6 [164],[165]. Furthermore, dual linear polarized operation with 3-bit phase compensation having the transmission loss less than $\alpha_T = 1.3$ dB is not accomplished in [162],[163],[166]. The maximum beam steering angle of [162],[166] is lower than the proposed TA as it can scan up to $\gamma_{max} = \pm 30°$. In case of scan loss, this work shows best performance ($\triangle G_{MSL1} = 2.73$ dB at $f_l = 12.4$ GHz) among the reference works [162],[163],[164],[165],[166]. Though, in comparison with the reference papers reported in Table 4, the proposed TA exhibits lowest aperture efficiency η except [166]. Finally, it can be said that the proposed TA achieves lower profile at the expense of gain G or aperture efficiency η.

Taking all these aspects into account, the proposed TA validates several significant merits: (i) a novel configuration based on circular metallic patterns, (ii) a low-profile structure while maintaining comparable performance, (iii) dual-polarized operation, (iv) satisfactory scan-loss performance at 12.4 GHz, (v) an improved beam-steering range, and (vi) ease of fabrication.

TABLE 3.4 COMPARISON OF PROPOSED TA WITH OTHER WORKS [156].

Ref.	[162]	[163]	[164]	[165]	[166]	This Work	
Frequency f (GHz)	27.5	10	12	15	12.5	12	12.4
No. of layers	2	3	5	3	3	3	3
Thickness ρ (λ_0)	0.18	0.133	0.582	0.165	0.083	0.126	0.13
Array size A (λ_0^2)	86.06	16.0	64.0	38.48	90.9	57.9	62.35
Gain G (dB)	24.2	19.3	23.0	23.06	22.7	21.0	19.97
Scan range γ_{max} (degree)	±27	+60	±35	±30	±21	±30	±30
Scan loss △G (dB)	3.7	4.15	3.0	3.6	2.7	4.03	2.73
F/D	0.50	0.60	0.78	0.75	0.59	0.60	0.60
Polarization	DLP[£]	SCP[$]	Ins*	DLP[£] & DCP[$]	SLP[£]	DLP[£]	DLP[£]
Side Lobe Level SLL (dB)	−18.4	−17.7	−15.0	−35.0	−15.0	−20.8	−18.5
Phase states	240°	180°	360°	360°	360°	360°	360°
Air gap	Yes	No	No	Yes	No	No	No
Aperture Efficiency η (%)	24.5	40.2	34.64	42.3	15.2	17.0	13.0

Ins* = Insensitive, DLP[£] = Dual linear polarized, DCP[$] = Dual circular polarized, SCP[$]= Single circular polarized. SLP[£] = Single linear polarized.

3.7 Conclusion

In this chapter, a low profile, dual-polarized 3-bit TA is proposed, simulated, and tested. This TA supports dual-polarized operation and offers a compact design with a low profile ($0.126\lambda_0$). Besides, efficient beam steering up to ±30° with minimal scan loss makes it demanding. The 1 dB gain bandwidth of BW_g = 10.8% (11.1–12.4 GHz), and a measured peak side lobe level of $SLL_1 = -20.8$ dB at $f_0 = 12$ GHz is also observed. Moreover, at $f_0 = 12$ GHz and $f_1 = 12.4$ GHz, a measured scan loss of $\triangle G_{MSL0} = 4.03$ dB and $\triangle G_{MSL1} = 2.73$ dB is achieved respectively. The aperture efficiency and measured gain at $f_0 = 12$ GHz are G_{m0} = 21 dB and $\eta_0 = 17\%$ respectively. However, at $f_2 = 11.2$ GHz, the maximum aperture efficiency $\eta_{max} = 19\%$ is observed. Considering all these characteristics, it can be concluded that, this proposed TA is suitable for Ku-band satellite applications.

4 Metasurface based antennas

The use of advanced metasurface-based radiating structures is necessary to fulfil the growing demand for high-performance, compact, and directive antennas in modern wireless and millimeter-wave systems. The design and performance analysis of three metasurface-inspired antennas is presented in this chapter. To enhance gain, bandwidth, radiation characteristics, and structural compactness these metasurface based antennas are developed. Firstly, a Fabry–Perot resonator antenna based on a Partially Reflective Surface (PRS) operating in the 7–9.5 GHz band is designed. Through constructive cavity resonance high gain is achieved by this antenna. Secondly, a Magneto-Electric (ME) dipole antenna integrated with Electromagnetic Band Gap (EBG) structure functioning in the 24–40 GHz range is designed to reduce side-lobe levels significantly by suppressing surface waves through metasurface. Thirdly, a ME dipole antenna operating at 24–30 GHz based on Artificial Magnetic Conductor (AMC) is presented. The profile of this antenna is minimized by employing a metasurface ground plane while maintaining radiation efficiency. In summary, the strategical utilization of engineered metasurfaces across microwave and millimeter-wave frequency bands for improving gain, radiation control, and compactness is demonstrated by these three designs.

4.1 PRS based Fabry Pérot Antenna

Due to the expansion of wireless communication systems and services such as Internet of Things and wearable devices, the demand for cost-effective, compact, and lightweight antennas is rapidly increasing. For this reason, conductive inkjet printing is considered as an effective and viable technique for the fabrication of antennas [167], [168]. The accurate placement of conductive inks into prede-

fined patterns, additive manufacturing capability and economic efficiency are the key benefits of this method [167], [168]. For the construction of conventional antenna, like in [168], [169], [170], conductive inkjet printing has been successfully utilized though the investigation related to its use for frequency selective surface- or metamaterial-based antennas is not conducted. Due to high directivity, and low-profile features, the Fabry–Pérot resonator antennas (FPRAs) have gained significant attention among various structures in the past decade [171]. By leveraging multiple in-phase reflections between a total reflector and a PRS, the broadside directivity of a simple radiator placed in the cavity can be increased [172]. The reflective properties, both magnitude and phase, of the PRS is related to this improvement [172]. Different strategies can be considered to design the latter one. For this purpose, 2-D metalized (printed) frequency selective surfaces (FSSs) [171], [173], non-metalized (unprinted) all-dielectric slabs [174], [175], and 3-D electromagnetic bandgap structures [176] can be utilized.

In the first part of this chapter, a novel FPRA is proposed with an unconventional fabrication technique. Specifically, this work employs a V-slot loaded patch antenna as a feed. This patch is fabricated through inkjet printing on two ultrathin PET substrates. One substrate is allocated to contain the radiating patch where the other one is for the ground plane. For phase manipulation, this works utilizes a double-layer based PRS. Two closely spaced PRSs form the structure, where each layer contains two single-sided ultrathin PET layers. To improve the PRS reflection phase response φ, a PETG layer is placed in between these two layers. A double-layer PRS with a tailored reflection phase response as a function of frequency is demonstrated for the first time. 3-D-printed PETG layers along with inkjet-printed PET layers is utilized for the design of the PRS. The operating frequency range of the optimized FPRA is 7.0 GHz to 9.5 GHz. A good agree-

ment between the simulation and the experimental results is observed which validates the concept of applying inkjet printing method for fabricating complex antenna having comparable performance in the examined frequency range achieved through conventional fabrication methods.

4.1.1 Design and simulation of the FPRA

Two main goals govern the design of the PRS unit cell:

i) achieving a suitable magnitude of the reflection coefficient ρ, and
ii) ensuring the desired phase response $\varphi_{I.}$

For obtaining good improvement of the directivity this is important. In a frequency band around the PRS resonance frequency, a positive phase gradient can be achieved because the associated positive phase gradient becomes more pronounced and steeper when the resonance strength raises [177]. It is worth to mention that the strong resonance is undesirable because the reflection coefficient magnitude ρ would be too low to obtain a good directivity even if the resonance condition may be satisfied. The sketch of the proposed FPRA consists of a double-layer PRS and a V-slot loaded patch is illustrated in Figure 4.1(a), whereas the sketch of the unit cell and the top layer of the V-slot loaded patch are reported in Figure 4.1(b) and Figure 4.1(c) [178].

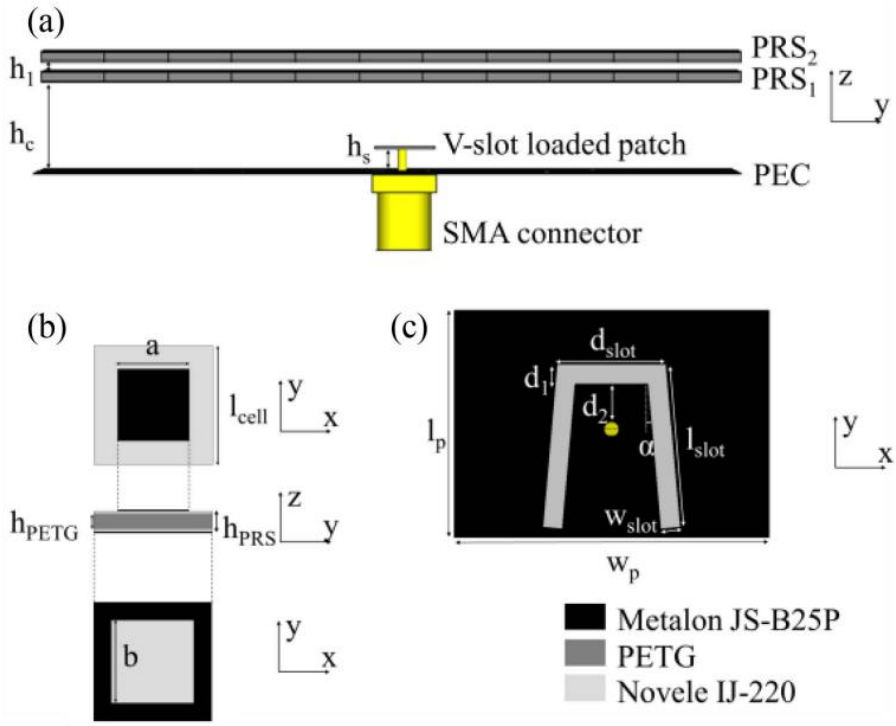

Figure 4.1 (a) Sketch of the FPRA, composed of a feed antenna, i.e., V-slot loaded patch with ground plane and radiating layer, and a double-layer PRS [178]; (b) sketch of the unit cell of a single layer of the double-layer PRS, composed of a square patch, a square aperture, both printed on two Novele IJ-220 substrates and an embedded all-dielectric PETG substrate [178]; and (c) sketch of the V-slot of the feed antenna [178].

Two PRSs, namely PRS_1 and PRS_2, ordered going upwards along the z-axis, represent the double-layer PRS in this design. Three sublayers compose each layer: a thicker PETG substrate, which sandwiched between two ultrathin PET substrates with a mesoporous coating, i.e., Novele1 IJ-220. A complimentary

FSS is constituted by depositing the conductive ink on Novele IJ-220 substrates with a printed periodic array of square patches (capacitive element) on one side and square apertures (inductive element) on the other side [177], [179], [180]. Thus, the antenna operation is contributed by both PRS_1 and PRS_2 through a resonance ignition. To further control and optimize the PRS reflection phase φ, the 3-D-printed PETG inside the two single-sided Novele IJ-220 substrates is introduced. The equivalent circuit of the double-layer PRS is illustrated in Figure 4.2 [181].

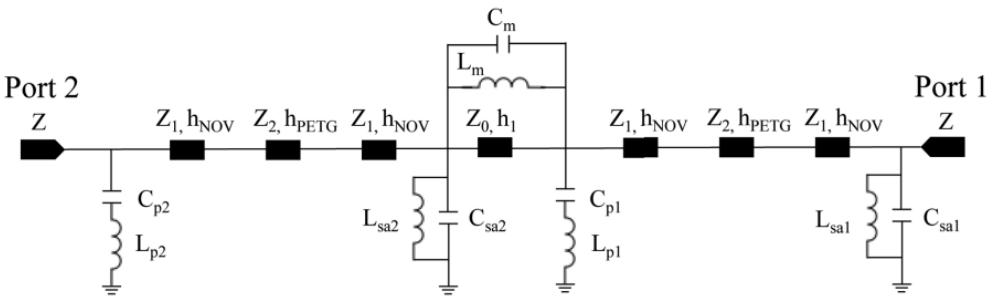

Figure 4.2 Equivalent circuit of the proposed double-layer PRS [178].

CST Microwave Studio Suite software is utilized to optimize the unit cell of the double-layer PRS through full-wave electromagnetic simulations in the frequency domain. In the four walls of the unit cell periodic boundary conditions are applied. The operating band of this proposed antenna started from about 7 GHz and ended about 9.5 GHz. In this frequency range , the phase gradient must be positive. Deembedding for the Floquet ports is taken into account to ensure accurate reflection phase evaluation, with the phase referenced at the square ap-

erture of PRS_1. The height of the employed PET-based substrate Novele IJ-220 is $h_{NOV} = 0.14$ mm. The dielectric constant of this substrate is $\varepsilon_r = 2.95$, and loss tangent is $\tan\delta = 0.025$ [182]. PETG is characterized with dielectric constant $\varepsilon_r = 2.85$, and loss tangent $\tan\delta = 0.025$ [183]. For the design optimization, the following parameters have been considered: lengths of the square apertures (a_1, and a_2, ordered going upwards along z-axis); length of the unit cell (L_{cell}, equal for the two PRSs); lengths of square patches (b_1, and b_2, ordered going upwards along z-axis); distance between PRS_1 and PRS_2 (h_1), and PETG thickness (h_{PETG}, equal for the two PRSs). The optimized dimensions of the PRS are: $a_1 = 8.6$ mm, $a_2 = 7.7$ mm, $b_1 = 8.8$ mm, $b_2 = 9.2$ mm, $h_{PETG} = 1.2$ mm, $h_{PRS} = 1.48$ mm, $h_1 = 2.52$ mm, $L_{cell} = 11.2$ mm. For incidence angle $\theta = 0^\circ$ (solid line) and $\theta = 20^\circ$ (dashed line), the simulated reflection coefficient magnitude ρ and phase φ of the double-layer PRS is shown in Figure 4.3. For a cavity height $h_{cav} = 19.70$ mm which is equal to half wavelength at the frequency $f = 7.6$ GHz, the ideal reflection phase φ_I is also showed. It is noted that the FPRA can resonate with high directivity D_{FPRA} also in case of angled incidence as the reflection amplitude coefficient is higher than 0.5 and a positive phase slope of PRS reflection coefficient is observed. To understand how the structure leads to a reflection phase with a positive slope as a function of the frequency, the equivalent circuit analysis has also been performed on the double-layer PRS. For an excellent agreement with the full wave unit cell simulations, the following values are employed: $Z = 377\ \Omega$, $Z_1 = 219.5\ \Omega$, $Z_2 = 223.3\ \Omega$, $C_{sa1} = 0.055$ pF, $C_{p1} = 0.1$ pF, $L_{sa1} = 1.97$ nH, $L_{p1} = 0.31$ nH, $C_{sa2} = 0.019$ pF, $C_{p2} = 0.074$ pF, $L_{sa2} = 2.76$ nH, $L_{p2} = 0.4$ nH, $C_m = 0.039$ pF, $L_m = 4$ nH. Based on this PRS, a practical finite-size antenna is developed.

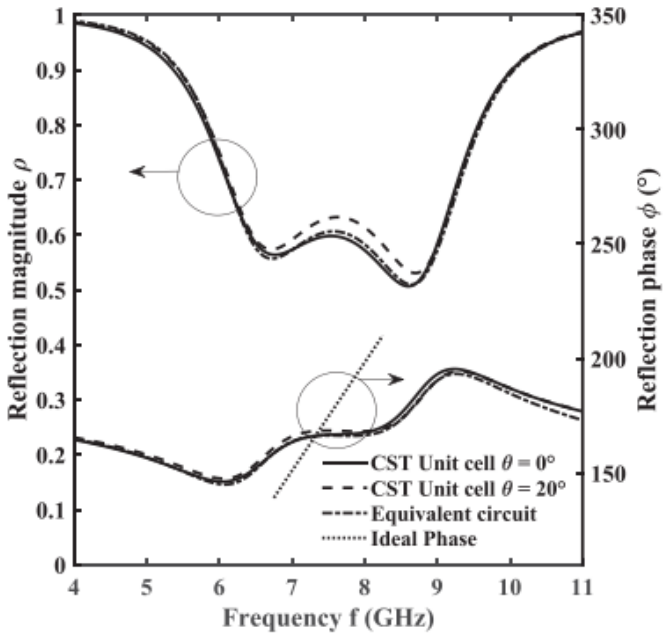

Figure 4.3 Reflection magnitude ρ and reflection phase φ of the double-layer PRS via: (i) CST Microwave Studio full-wave unit cell simulation, for incidence angle θ = 0° (solid line) and θ = 20° (dashed line); (ii) equivalent circuit model (dash-dotted line). Ideal reflection phase for an FPRA with cavity height h_c = 19.7 mm (dotted line) [178].

In order to increase the bandwidth of the primary radiator, a V-slot is introduced in the pin-fed optimized rectangular patch antenna [184]. The values of the following parameters show the optimized dimensions: d_1 = 1.15 mm, d_2 = 1.65 mm, d_{slot} = 6.45 mm, α = 5°, w_{slot} = 1.15 mm, w_p = 18.7 mm, l_p = 13.5 mm, l_{slot} = 9.7 mm. At the center frequency, the array size of the PRS is approximately 2.2 λ_0 × 2.2 λ_0 × 0.70 λ_0 i.e., 78.4 mm × 78.4 mm. For the ground the same dimensions are chosen. The optimized distance between the ground and the patch is h_s = 3.3

mm while the cavity height is h_c = 19.7 mm. The simulated input reflection coefficient $|S_{11}|$ along with the realized gain G for the antenna with (w/) PRS (dashed line) and without (w/o) PRS (solid line) is reported in Figure 4.4. Due to the Fabry–Pérot resonance, an improvement of the realized gain G is obtained while maintaining almost entirely the bandwidth of the primary radiator.

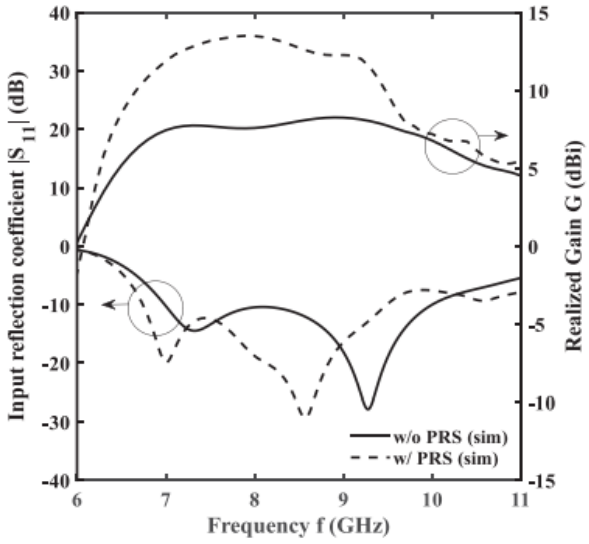

Figure 4.4 Simulated input reflection coefficient $|S_{11}|$ and realized gain G of the antenna w/o PRS (solid line) and w/ 7 × 7 PRS array size (dashed line) [178].

4.1.2 Fabrication and characterization of the FPRA

The pattern has printed on the Novele IJ-220 substrate using the conductive inkjet Metalon JS-B25P through an inkjet printer EPSON Ecotank ET-M1170. The thickness of PETG is freely optimized as it is obtained via 3-D printing.

Metalon JS-B25P with silver content of 25 wt% is used as the conductive ink. The gluing of the SMA connector is achieved by applying MG Chemicals 8331S silver-filled conductive epoxy, followed by thermal curing at 65 °C for 2 hours. For printing the PETG at 100% infill density, a low-cost Creality K1C 3-D printer, based on fused deposition modelling is used. A nozzle with a 0.2 mm diameter is utilized as spacer. Figure 4.5 depicts pictures of the fabricated prototype: (a) the V-slot loaded patch antenna (Top layer); (b) Dino-Lite Digital Microscope assisted image; (c) an illustration of square apertures as a periodic array of PRS_2; (d) an illustration of square patches as a periodic array of PRS_2; (e) the complete prototype of the proposed FPRA during characterization in the anechoic chamber.

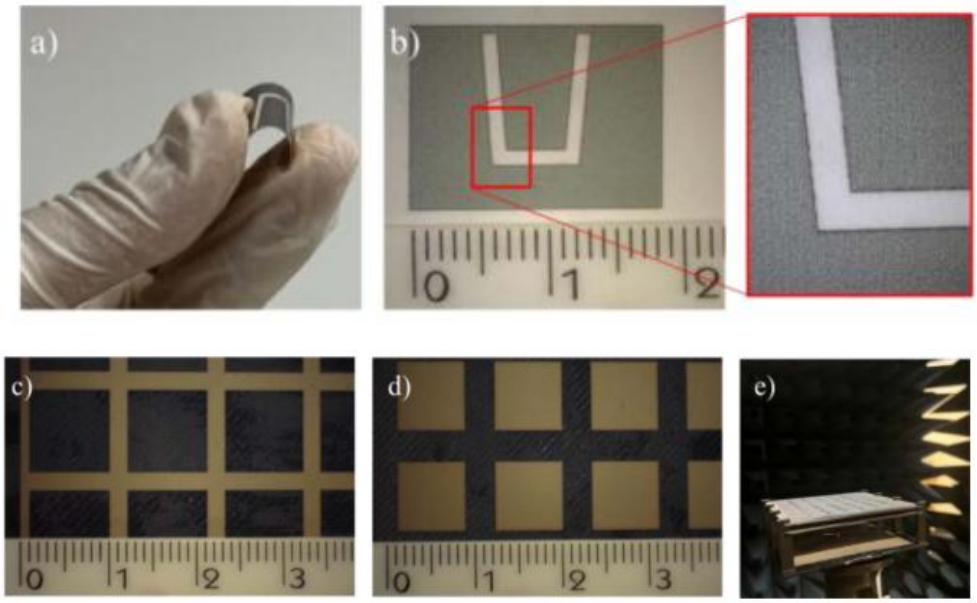

Figure 4.5 (a) Picture of the fabricated V-slot loaded patch via conductive inkjet printing [178]. (b) Microscope image of the fabricated V-slot loaded patch via conductive inkjet printing with an enlargement [178]. (c) Enlargement of the periodic array of square apertures, bottom layer of PRS_2 [178]. (d) Enlargement of the periodic array of square patches, top layer of PRS_2 [178]. (e) Mounted FPRA with V-slot loaded patch and double-layer PRS in the anechoic chamber [178].

In comparison with the cost of conventional materials and fabricating technologies, the overall cost for the FPRA fabrication is very low as it costs only a few percent of the expense of traditional techniques. Presently, the cost incurred of is: i) around 5.0 $ attributed to the needed volume of conductive ink; ii) nearly 1.0 $ for the PETG substrates and mechanical support; iii) about 0.5 $ for a single ultrathin PET sheet. The total weight of the proposed FPRA is 52 g which includes the weight of the SMA connector also. The Agilent Technologies N5224A PNA Network Analyzer is used to measure the scattering parameter S_{11}

of the antenna w/o and w/ the PRS conditions. The anechoic chamber StarLab SATIMO is used to accomplish the radiation performance measurement of the antenna w/o and w/ the PRS. The comparison between the simulated (solid line) and measured (dashed line) input reflection coefficient $|S_{11}|$ of the antenna w/o PRS (black line) and w/ PRS (red line) conditions is reported in Figure 4.6(a).

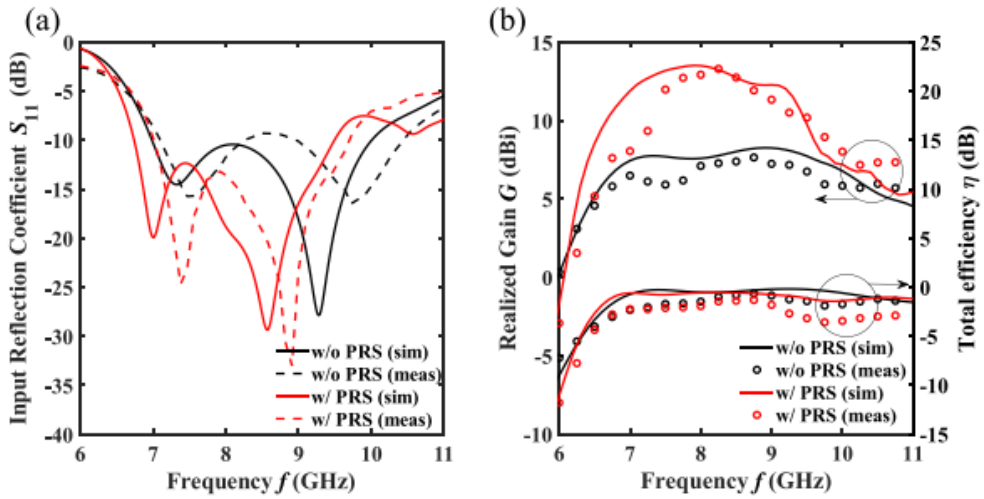

Figure 4.6 (a) Simulated (solid line) and measured (dashed line) input reflection coefficient $|S_{11}|$ of the antenna w/o PRS (black line) and w/ PRS (red line) [178] and (b) simulated (solid line) and measured (circle markers) realized gain G and total efficiency η of the antenna w/o PRS (black) and w/ PRS (red) [178].

Apart from a slight shift towards higher frequency, a good agreement between simulation and measurement result is observed. For exhibiting a good degree of repeatability, a set of ten FPRAs has been constructed. The connector gluing

may have an effect on the frequency shift. Simulation result show that variations in the dielectric constant have minimal influence on the input reflection coefficient of the patch antenna, as the thickness of the PET substrates is very thin. From the measured result, it can be noted that the impedance bandwidth of the FPRA's spans from 7.0 GHz to 9.6 GHz. The measured (circle markers) and the simulated (solid line) realized gain G along with total efficiency η of the antenna w/o PRS (black) and w/ PRS (red) conditions are illustrated in Figure 4.6(b). At the frequency f = 8.2 GHz, a high measured gain of G_M = 13.2 dBi is provided by the FPRA. Within the impedance bandwidth of the FPRA, the measured 3 dB gain bandwidth of the FPRA is BW_G = 24.5%. Moreover, the aperture efficiency in measurement is noted 35.3% approximately. The simulated and measured radiation patterns of the antenna with PRS for both the H-plane, and the E-plane at the frequency f = 8 GHz are illustrated in Figure 4.7. The measured radiation pattern of this proposed antenna indicates about its capability of transmitting single broadside main lobe with acceptable cross polar discrimination and low side lobe level.

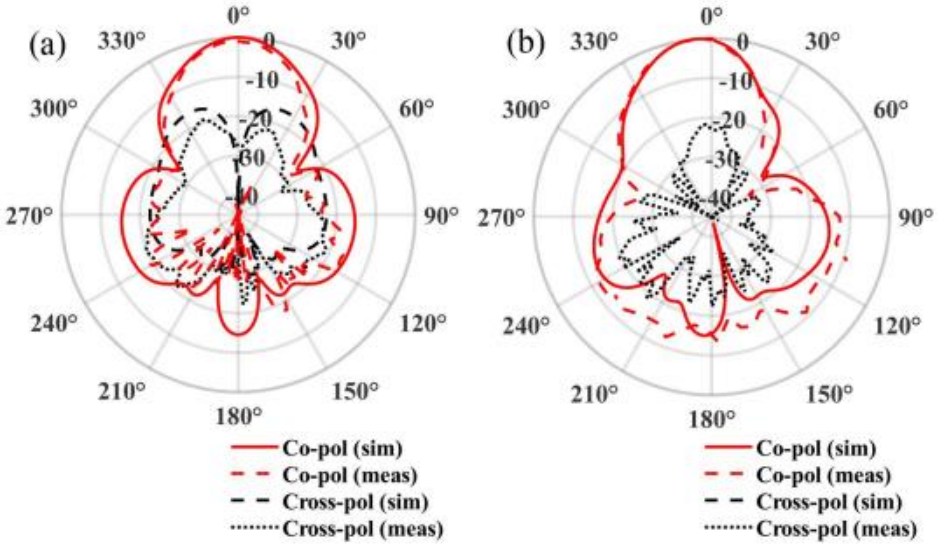

Figure 4.7 Simulated and measured normalized radiation patterns at the frequency f = 8 GHz of the antenna with PRS: (a) H-plane [12] and (b) E-plane [178].

4.1.3 Performance comparison with literature

Some probable reasons responsible for small variations between the simulation and measurement result are as follows: i) the inaccurate fabrication process, considering the precision of the inkjet printing, ii) the position mitch match of the SMA pin in simulation and in practical prototype, iii) misalignment of the four PET layers in the PRS, iv) tilting of the patch top layer slightly, v) conductive glue utilization in order to solder the connector, etc. However, the flexibility offered by the fabrication process is more important than the minor performance reduction in some applications. The comparison between the proposed FPRA to

other printed circuit board (PCB) technology based FPRAs is shown in Table 4.1. The gain and impedance performance are similar with the FPRAs in [177], [185], and [186]. The proposed one exhibits a lower profile compared with the FPRAs in [172], [173], [181], and [187]. Table 4.2 provides the comparison between the proposed FPRA to other conductive inkjet printed antennas. The proposed antenna exhibits a lower planar size in comparison to [167] and free from complex feeding network also. The wideband performance is obtained with higher gain with reference to [168], and [188].

TABLE 4.1 PROPOSED FPRA COMPARED TO LITERATURE FPRAS [178].

Ref. no.	**Size (W×L×H)**	**Imped. BW(%)**	**3-dB BW(%)**	**Max Gain (dBi)**	**Aperture Efficiency (%)**
[172]	$1.5\lambda_0 \times 1.5\ \lambda_0 \times 1.7\ \lambda_0$	> 30	21.7	18.2	58.4
[173]	$3.9\ \lambda_0 \times 3.9\ \lambda_0 \times 1.7\ \lambda_0$	15.1	15.0	20.0	53.1
[177]	$2.4\ \lambda_0 \times 2.4\ \lambda_0 \times 0.66\ \lambda_0$	37.0	32.3	14.0	31.9
[181]	$2.3\ \lambda_0 \times 2.3\ \lambda_0 \times 1.34\ \lambda_0$	31.7	25.8	15.0	47.6
[185]	$3.7\ \lambda_0 \times 3.7\ \lambda_0 \times 0.76\ \lambda_0$	10.9	10.9	16.3	25.4
[186]	$2.2\ \lambda_0 \times 2.2\ \lambda_0 \times 0.54\ \lambda_0$	25.1	33.5	13.9	40.4
[187]	$3.0\ \lambda_0 \times 3.6\ \lambda_0 \times 1.3\ \lambda_0$	20.4	12.2	15.6	26.8
This work	$2.2\ \lambda_0 \times 2.2\ \lambda_0 \times 0.70\ \lambda_0$	31.3	24.7	13.2	36.2

TABLE 4.2 PROPOSED FPRA COMPARED TO LITERATURE INKJET PRINTED ANTENNAS [178].

Ref. no.	Size (W×L×H)	Imped. BW(%)	3-dB BW(%)	Max Gain (dBi)	Aperture Efficiency (%)*
[167]	2.5 λ_0×2.5 λ_0×0.05 λ_0	7.5	7.5	16.7	59.6
[168]	1.6 λ_0×1.9 λ_0× N.A.	133.0	> 90	7.8	7.0
[188]	1.3 λ_0×1.2 λ_0×0.01 λ_0	> 34	> 42	8.5	36.1
[189]	1.0 λ_0×1.0 λ_0×0.04 λ_0	11.6	12.0	9.2	54.6
This work	2.2 λ_0×2.2 λ_0×0.70 λ_0	31.3	24.7	13.2	36.2

* The aperture efficiency is evaluated at the frequency corresponding to the max gain.

The proposed antenna shows better performance in terms of both bandwidth and gain than the antenna reported in [189].

4.1.4 Summary

This work proposes low cost lightweight PRS based high gain Fabry-Pérot antenna. A hybrid fabrication technique consisting of both inkjet printing and 3D printing is considered for constructing the prototype. Particularly, the primary radiator and the PRS consists of printed array of square patches and apertures, were obtained by depositing conductive ink on single layer mesoporous coated ultra-thin PET substrates. Though, fused deposition modelling 3D printing is used for obtaining the dielectric PETG layers required for the PRS, and the spacers. A maximum measured gain of G_M = 13.2 dBi is obtained at f = 8.2 GHz which maintains a good agreement with the simulated result. In measurement, the impedance bandwidth and the 3 dB gain bandwidth of $BW_{\%}$ = 31.3 % and BW_G = 24.5% found respectively. The 3 dB gain bandwidth resides within the impedance bandwidth range. The promising result indicates the potential for re-

alizing complex antenna though low-cost and fast prototyping techniques utilization. Study of conformal Fabry-Pérot cavities, flexible metasurfaces and antenna of unconventional shape difficult to fabricate through traditional techniques can be good directions of future research.

4.2 EBG based wideband Millimeter wave antenna

Recently, huge rise in global data traffic has been observed, reaching an annual growth rate of approximately 79% [190]. Fifth-generation (5G) mobile communication systems are anticipated to provide an efficient solution to address the resulting network congestion [191]. To achieve available bandwidth, the 5G standard for licensed usage of the 28 and 39 GHz frequency bands are introduced by the Federal Communications Commission (FCC) [191]. Hence, millimeter wave (mm-wave) antenna having wideband response covering both 28 GHz and 39 GHz is utterly popular. To compensate the air propagation loss at mm-wave frequencies a satisfactory high gain performance is another critical requirement for this kind of antenna. Specifically, stable radiation pattern and a constant gain over the entire bandwidth are necessary. At mm-wave frequencies, the employment of simple patch antennas is shown by some research [192],[193], though highest 30% impedance bandwidth is provided by the multilayered patch [194],[195].

A possible approach to meet these requirements is the use of a magneto-electric (ME) dipole antenna, which offers wide bandwidth characteristics [70] and can

be realized through substrate-integrated waveguide (SIW) techniques [80] or 3D-printed waveguide technology [196]. Due to the cutoff frequency characteristics, the bandwidth of the SIW feed based ME dipole antenna is generally not greater than 35% [197]. However, ME dipole antenna based on low temperature cofired ceramic (LTCC) technology proposed in [198] provides an impedance bandwidth over 45% [198], though in comparison with the printed circuit board (PCB) based antenna, this technology is not preferable for the high fabrication cost. ME dipole antenna based on the gap waveguide (GWG) based feed is proposed in [82],[199], as GWG is effective due to low loss and high efficiency features [200]. Though, for mm-wave antenna designs, the fabrication process of GWG is complicated as it relies on fully metallic configuration. In [201], a ME dipole antenna array based on microstrip line feed is proposed. A reduced impedance bandwidth of 16.7% is provided by this antenna array though it is based on a very simple fabrication technology. This research presents a high-performance based ME dipole antenna based on microstrip line feed. For achieving large bandwidth and low side lobe level (SLL), this multi-stacked aperture coupled antenna is integrated with an electromagnetic bandgap (EBG) structure. A simulated -10 dB impedance bandwidth of BW = 45.8% (25.1-40 GHz) and high radiation efficiency $\eta > 0.91$ over the gain bandwidth is provided by the proposed mm-wave ME dipole antenna. The design employs a multilayer PCB platform for low-cost fabrication and easy integration with printed electronics.

4.2.1 Antenna Structure

The antenna stack up is illustrated in Figure 4.8. Four dielectric substrates and a bondply layer form this proposed antenna. Rogers RT/Duroid 5880 ($\epsilon_s = 2.2$, $\tan\delta_s = 0.0009$) is the material of all the substrates whereas the bondply is made of Rogers 4450F ($\epsilon_b = 3.52$, $\tan\delta_b = 0.004$).

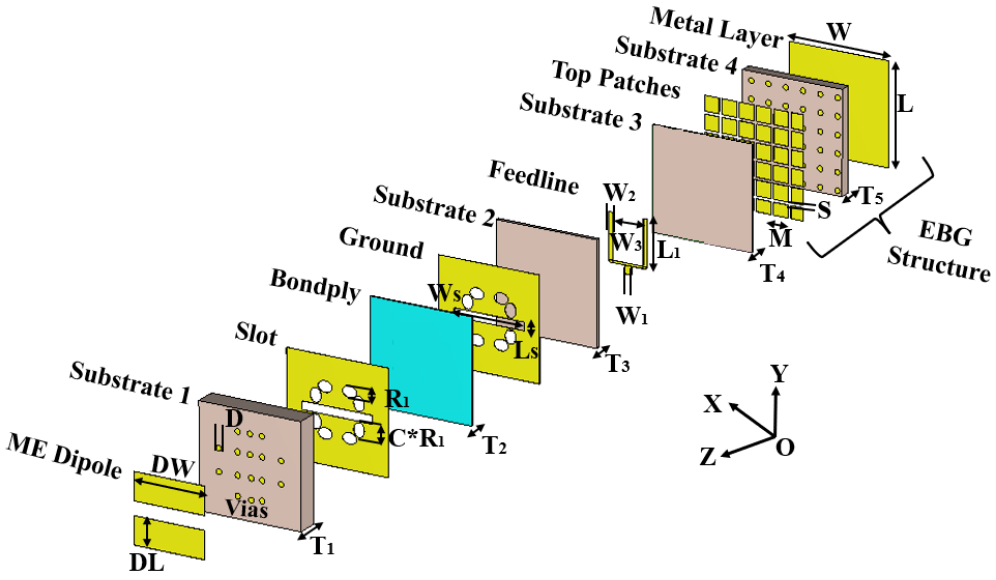

Figure 4.8 Sketch of the antenna stack up [202].

The ME dipole is excited through an aperture couple feeding method. Several elliptical and one rectangular slots are created in the lower metal layer of the substrate 1 and the ground plane. Additionally, below substrate 3, one EBG structure is placed. The antenna has an overall height of h = 0.25 λ_L, where the wavelength λ_L = 11.95 mm corresponds to the frequency f_L = 25.1 GHz. In order to maximize the gain and to enlarge the bandwidth, a number of simulations were performed by changing the following parameters: width of the rectangular slot (W_s), length of the rectangular slot (L_s), minor axis width parameter of the elliptical slot (R_1) and major axis width parameter of the elliptical slot (C). Table 4.3 listed the optimized values obtained for producing the best result in terms of gain and bandwidth.

TABLE 4.3 OPTIMIZED DIMENSION [202].

Parameter	Value (mm)	Parameter	Value (mm)	Parameter	Value (mm)	Parameter	Value (mm)
T_1	1.575	L	7.50	DL	2.00	W_S	5.20
T_2	0.10	L_1	3.50	W	7.50	DW	5.20
T_3	0.254	L_S	0.60	W_1	0.55	M	1.10
T_4	0.127	R_1	0.80	W_2	0.27	D	0.40
T_5	0.787	C	1.30	W_3	2.30	S	0.20

4.2.2 Electromagnetic bandgap (EBG) structure

Figure 4.9(a) shows the enlarged structure of the metasurface which works as an EBG structure here. The length of the rectangular patch is M =1.1 mm and the spacing between two adjacent patches is S = 0.2 mm. The thickness of the substrate that contains the metasurface is T_5 = 0.787 mm. To analyze the behavior of this EBG, a Floquet port is assigned with proper boundary conditions for unit cell simulation of this metasurface shown in Figure 4.9(b).

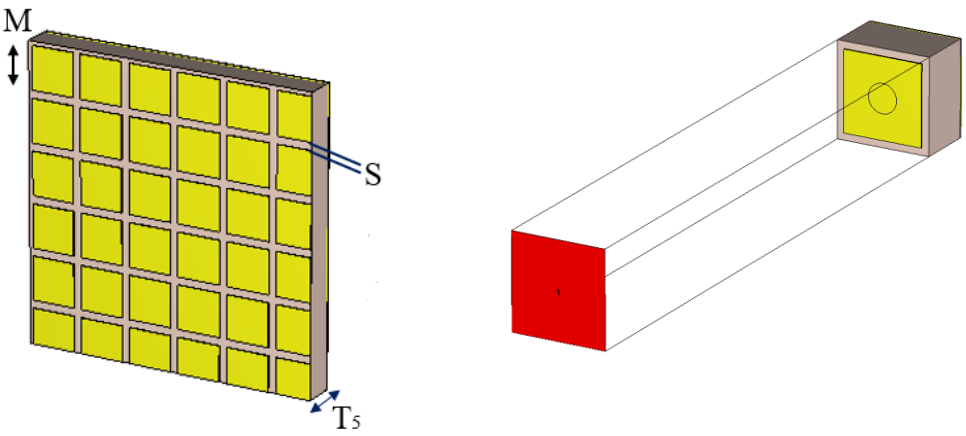

(a) (b)

Figure 4.9 (a) Detailed view of the EBG. (M =1.1 mm, S = 0.2 mm, T_5 = 0.787 mm), (b) Floquet port excitation for unit cell simulation.

The main aim of this simulation is to retrieve the dispersion curve for finding the bandgap of this structure. For this purpose, the phase shift of the normalized wave vector is swept along the high-symmetry points of the first Brillouin zone: Γ representing zero phase shift, X corresponding to a phase shift of π along one lattice direction, and M representing (π, π) along both directions. The eigenfrequencies of the unit cell are calculated by varying the phase from Γ → X → M → Γ. The electromagnetic bandgap frequency range is defined where no propagation modes appear. From the dispersion diagram shown in Figure 4.10, the bandgap of this structure obtained is 29.5 GHz to 39.5 GHz.

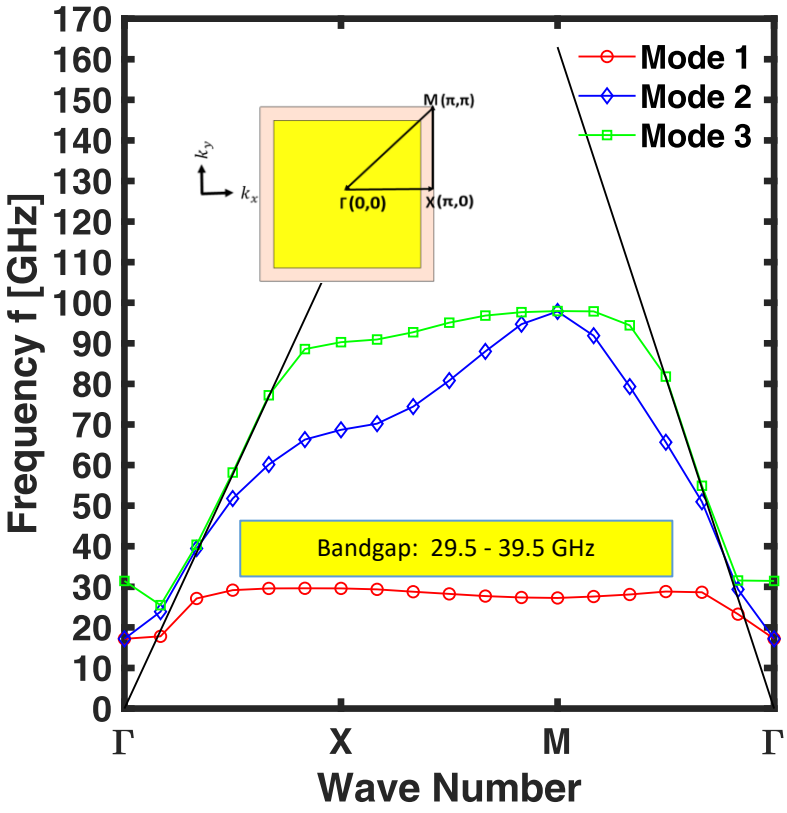

Figure 4.10 Dispersion diagram of the EBG.

4.2.3 Performance of the antenna structure

For both with and without elliptical slots conditions, the simulated scattering parameter S_{11} vs. frequency f curve is shown in Figure 4.11(a). A widening of

the simulated bandwidth is obtained for the optimized elliptical slots in metal planes. It is noted that several 5G NR bands are covered by the simulated fractional impedance bandwidth BW = 45.8% (25.1-40 GHz). The simulated 3 dB gain bandwidth and radiation efficiency as a function of frequency f are plotted in Figure 4.11(b). The highest simulated realized gain is RG_{max} = 8.20 dB noted at the frequency f_m = 34 GHz whereas the simulated fractional 3 dB gain bandwidth is BW_g = 42.4%. The radiation efficiency is $\eta > 0.91$ over the 3 dB gain bandwidth.

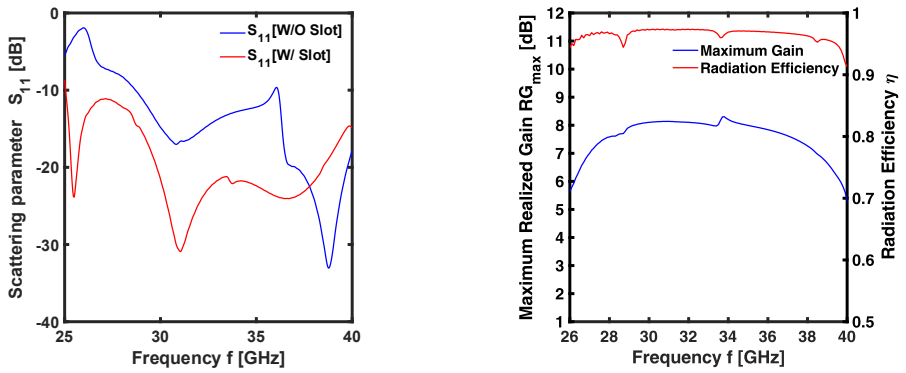

(a) (b)

Figure 4.11 (a) Simulated S_{11} vs. frequency f [202]. (b) Simulated realized gain RG_{max} and simulated radiation efficiency η vs. frequency f [202].

The simulated radiation pattern for the three frequencies f_1 = 29 GHz, f_m = 34 GHz and f_2 = 39 GHz are depicted in Figures 4.12,4.13 and 4.14, respectively. It is worth to mention that, the simulated SLL in every case is reduced by the EBG structure through suppressing surface wave propagation. In particular, the simulated side lobe level at the frequency f_2= 39 GHz, with and without EBG struc-

ture is $SLL_{W/} = -15.4$ dB and $SLL_{W/O} = -6.6$ dB, respectively.

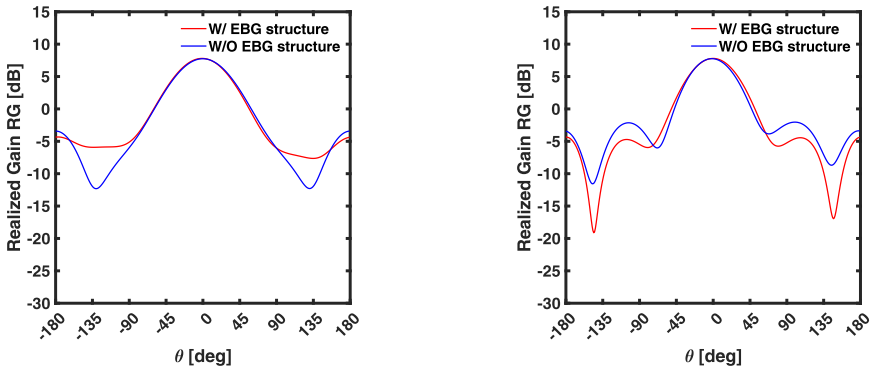

(a) (b)

Figure 4.12 Simulated realized gain RG vs. θ for f_l = 29 GHz. (a) XOZ plane [202] and (b) YOZ plane [202].

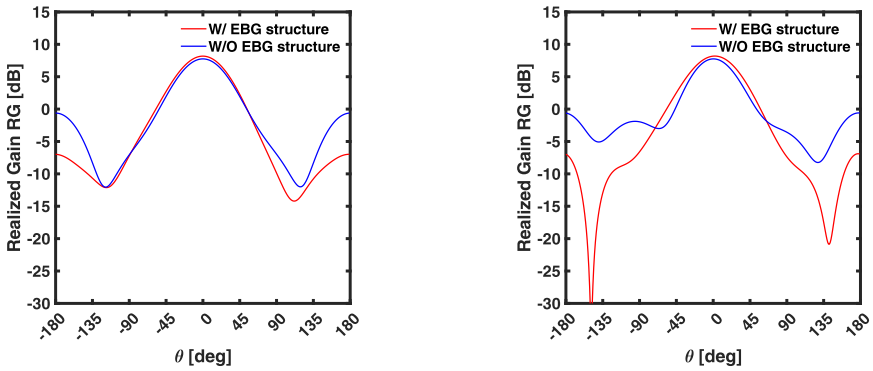

(a) (b)

Figure 4.13 Simulated realized gain RG vs. θ for f_m = 34 GHz. (a) XOZ plane [202] and (b) YOZ plane [202].

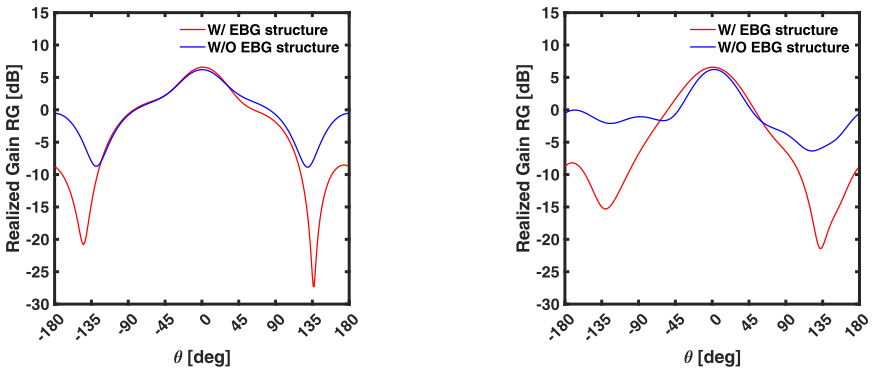

(a) (b)

Figure 4.14 Simulated realized gain RG vs. θ for f_2 = 39 GHz. (a) XOZ plane [202] and (b) YOZ plane [202].

For all the frequencies, f the maximum gain is pointed in the boresight direction and the realized gain RG patterns are symmetrical.

4.2.4 Comparison with other works

A comparison of the proposed antenna's performance is made with other 5G mm-wave designs previously published. Table 4.4 shows the comparison. The proposed antenna demonstrates a simulated -10 dB impedance bandwidth, BW which is marginally narrower than [203] but larger than [204],[205],[206]. Though, the proposed antenna outperforms those reported in [203], [204], [205], [206] regarding the simulated peak gain G_{max}. In case of simulated 3 dB gain bandwidth, BW_g, of the proposed antenna also provides higher gain than those reported in [204],[205],[206].

TABLE 4.4 COMPARISON WITH RELATED WORKS [202].

Reference	**Simulated -10 dB Impedance Bandwidth, BW (%) (GHz-GHz)**	**Simulated Peak Gain, G_{max} (dB)**	**Simulated 3 dB Gain Bandwidth, BW_g (%) (GHz-GHz)**
[203]	47% (24.6–39.7)	5	42.4% (26-40)
[204]	40% (25.8–38.8)	6.12	40% (25.8–38.8)
[205]	14.6% (25.6–29.4)	1	26.8% (25-28.5)
[206]	26.9% (20-26.2)	2.6	26.9% (20-26.2)
This work	45.8% (25.1–40)	8.2	42.4% (26-40)

4.2.5 Summary

The proposed antenna exhibits a simulated impedance bandwidth of BW = 45.8% with a simulated fractional 3 dB gain bandwidth BW_g = 42.4% by exploiting elliptical slots in different metal planes of the stack up. Low SLL and a simulated radiation efficiency $\eta > 0.91$ over the gain bandwidth indicates that this antenna is appropriate for mm-wave applications.

4.3 AMC based magneto electric dipole antenna

For mobile devices, several studies have been done on different 5G mm-wave antennas, particularly those operating in the FR2 band [207]. At mm-wave bands, patch and slot antennas have gone through an extensive advancement over the last decade [208],[209],[210],[211]. These antennas support only 10% impedance bandwidth though designs are simple. Several studies show various techniques for improving impedance bandwidth. For example, in [212], air cavity is used to enhance the impedance matching, as it suppresses the surface wave and directs energy toward the boresight direction. An impedance bandwidth of 15.3% and a 3 dB gain bandwidth of 16.1% are supported by this air cavity backed patch antenna array [212]. In addition, mm-wave antennas based on substrate-integrated waveguides (SIW) [213] and substrate-integrated coaxial lines (SICL) [214] have also been studied. Despite providing reduced loss, SIW and SICL designs are not feasible for portable 5G devices due to the structural complexity.

Considering the broadband operation, high gain, and stable radiation pattern, magneto-electric (ME) dipole antennas [70],[172] are widely investigated nowadays [215]. This antenna is advantageous because of symmetrical E- and H-plane radiation patterns and low back radiation. Traditionally, feeding of ME dipole antennas is typically achieved using probe, transmission line, and aperture excitation methods [216]. In case of probe excitation, the position and structure of the probe can be modified to optimize antenna performance and to control the excitation waveform [217]. This approach suffers from manufacturing difficulties results from the need for complex probe structures. On the other hand, the transmission line feed based antennas provide high gain [218], but reducing their size is not easy when dealing with large-scale complex configuration. Alterna-

tively, by using slots etched in the ground plane, the aperture excitation method can exhibit multiple resonance modes. This method is considered simple among these three methods, due to easier fabrication feature [219].

Another important design consideration of ME dipole antenna is the profile height. Generally, in case of ME dipole antenna, a distance of $0.25\lambda_r$ (λ_r is the medium wavelength of the center frequency, f_c) is maintained between the radiating element and the reflector [12]. This theory results in a high profile ME dipole antenna limiting its aptness for certain applications. Some authors employ bending metal wall [220] or load medium [221] to overcome this problem. Nevertheless, these methods are not suited for PCB based ME dipole antenna. On the other hand, the antenna's profile height can be reduced through replacing the ground plane by the metasurface (MS) structure [222] as required phase reflection can be provided by it if designed properly [223]. Hence, to construct a low-profile ME dipole antenna the usage of the MS structure can help.

A MS loaded aperture feeding based ME dipole antenna having high performance is presented in this research. A bandwidth of BW_i = 6 GHz (24-30 GHz) is supported by this proposed antenna. This antenna is appropriate for actual application in 5G mm-wave bands because of stable radiation pattern and a radiation efficiency $\eta > 0.94$ over the bandwidth.

4.3.1 Antenna structure

The antenna stack up is illustrated in Figure 4.15 (a) whereas Figure 4.15 (b) shows the detailed view of the feed structure. Three substrates and a bondply layer form this proposed antenna. F4BME220 ($\epsilon_s = 2.2$, $\tan\delta_s = 0.0014$) material is considered for the substrate 1, 2 and 3. Rogers 4450 ($\epsilon_b = 3.7$, $\tan\delta_b = 0.004$) material is chosen for the bondply layer.

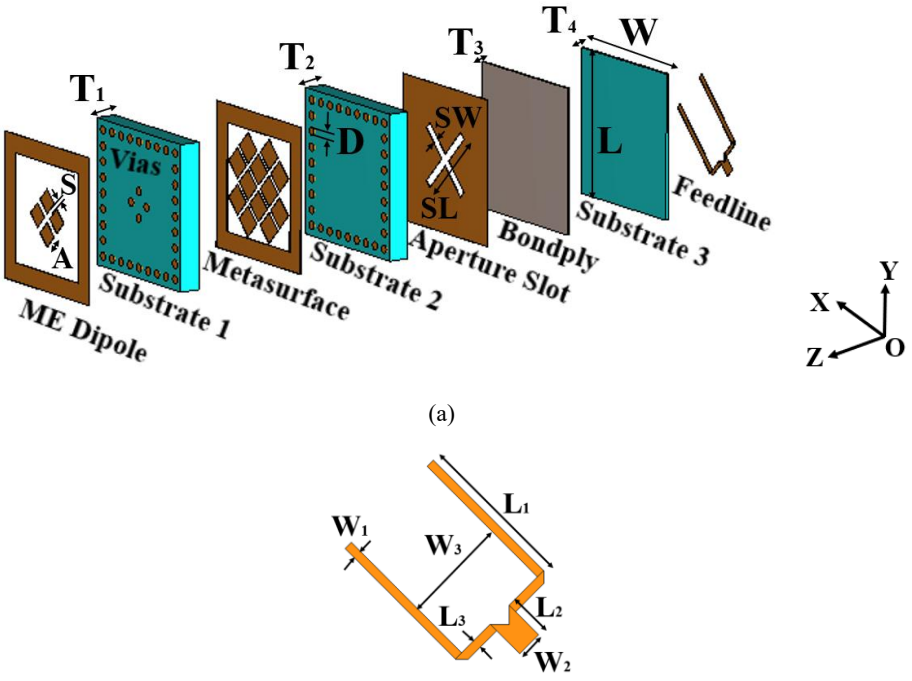

(a)

(b)

Figure 4.15 (a) Sketch of the antenna stack up [18], (b) detailed view of the feedline [224].

For a wavelength $\lambda_c = 11$ mm, corresponding to the central frequency, $f_c = 27$ GHz, the overall dimension of this antenna is $0.9\times0.9\times0.21\lambda_c^3$. By changing the value of parameters, several simulations were performed to get optimized values. Parameters listed in Table I shows the optimized values.

TABLE 4.5 OPTIMIZED DIMENSION [224].

Parameter	**Value (mm)**	**Parameter**	**Value (mm)**	**Parameter**	**Value (mm)**
T_1	1.00	L_1	3.50	W	10.00
T_2	1.00	L_2	0.74	W_1	0.20
T_3	0.10	L_3	0.20	W_2	0.60
T_4	0.127	SL	4.00	W_3	2.40
L	10.00	SW	0.40	S	0.15
A	0.83	D	0.40		

4.3.2 Artificial Magnetic Conductor (AMC)

The MS designed in this antenna works as an artificial magnetic conductor (AMC). The detailed view of the MS is shown in Figure 4.16 (a). To achieve slant (+45°) polarization, the feedline and MS are placed at an angle of $\alpha = +45°$ in the XOY plane. The MS consists of a patch array layer on the top of the substrate 2 and a ground layer. The size of the single square patch is MW = 1.05 mm, and the gap between two adjacent patches is MS = 0.19 mm. The MS is fragmented into unit cell to simulate so that the characteristics of this MS can be revealed. Floquet port is assigned to excite the unit cell shown in Figure 4.16 (b).

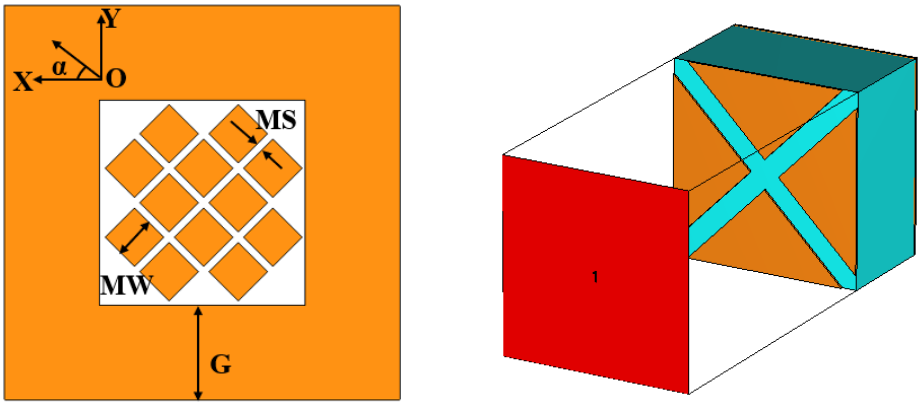

(a) (b)

Figure 4.16 (a) Detailed view of the AMC. (MW =1.05 mm, MS = 0.19 mm, G = 2.40 mm), (b) Floquet port excitation for unit cell simulation.

The characteristic of this MS is shown in Figure 4.17. In particular, Figure 4.17 (a) demonstrates the magnitude of the reflection coefficient $|S_{11}|$ vs. the frequency, f curve. A high value of reflection coefficient $|S_{11}|$ close to 1 is observed from f_L = 24 to f_H = 30 GHz. The phase of reflection coefficient $\angle S_{11}$ vs. the frequency, f is illustrated in Figure 4.17 (b). It is evident that the phase of reflection coefficient $\angle S_{11}$ varies from +90° to -90° throughout the band ranging from f_L = 24 to f_H = 30 GHz. It can be noted that this MS provides an in-phase reflection in the target band with a high reflection magnitude. Hence, this MS can be treated as AMC. The incorporation of AMC structure enables in phase reflection without maintaining the conventional height ($\lambda_c/4$ = 2.78 mm for the center frequency, f_c = 27 GHz) of the magnetic dipole causes an overall profile reduction of 28%.

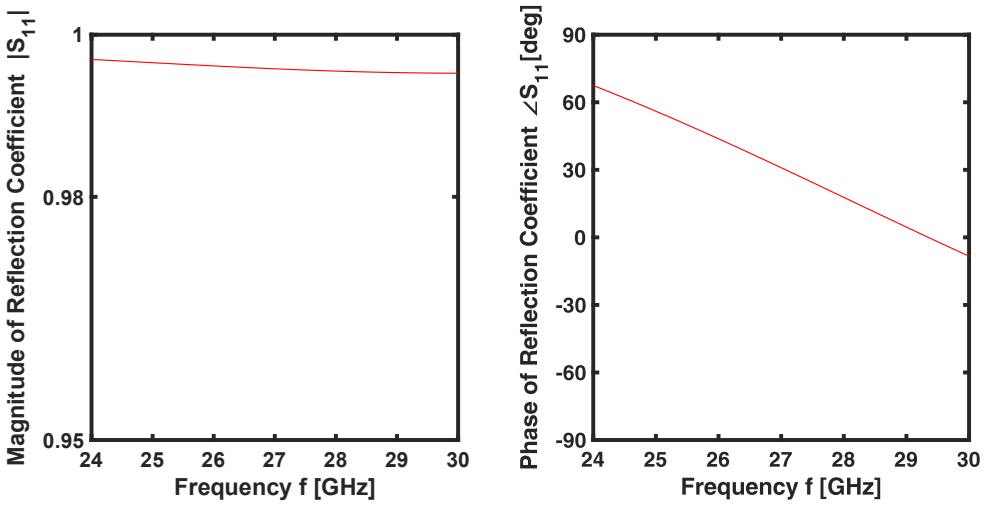

(a) (b)

Figure 4.17 Reflection Coefficient S_{11} vs. Frequency f. (a) Magnitude and (b) Phase.

4.3.3 Performance of the antenna structure

The simulated reflection coefficient S_{11} and the simulated radiation efficiency η as a function of frequency f are shown in Figure 4.18(a). The antenna exhibits a −10 dB impedance bandwidth of BW_i = 6 GHz (24–30 GHz) with a simulated radiation efficiency, η greater than 0.94 across the operating band. The simulated realized gain RG versus the frequency f is demonstrated in Figure 4.18 (b). The peak realized gain, RG_{max} reaches 8.2 dB at f_m = 29 GHz. The realized gain RG curve demonstrates that, the simulated fractional 2 dB gain bandwidth is BW_{ge} = 22.2% (24-30 GHz). The radiation pattern for f_L = 24 GHz, f_c = 27 GHz and f_H = 30 GHz is depicted in Figure 4.19(a),(b),(c), respectively.

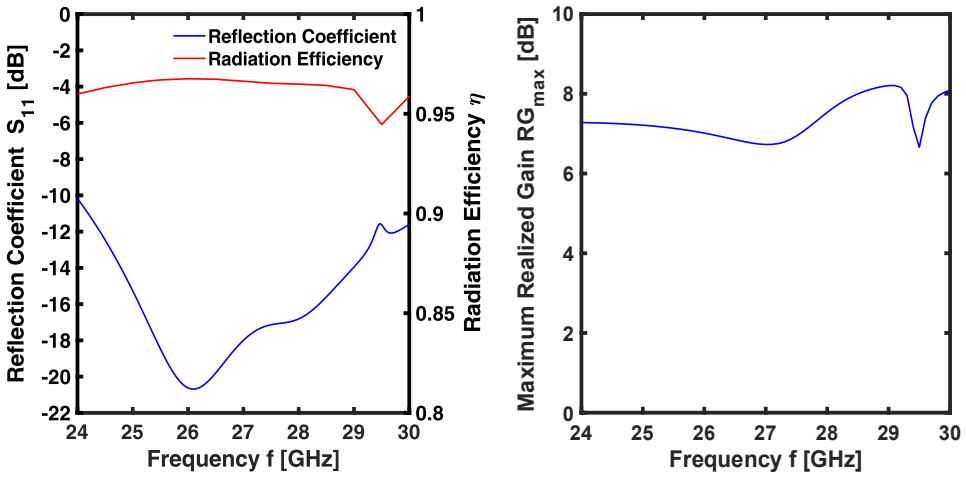

(a) (b)

Figure 4.18 (a) Simulated reflection coefficient S_{11} and radiation efficiency η vs. frequency f [224]; (b) Simulated realized gain RG_{max} vs. frequency f [224].

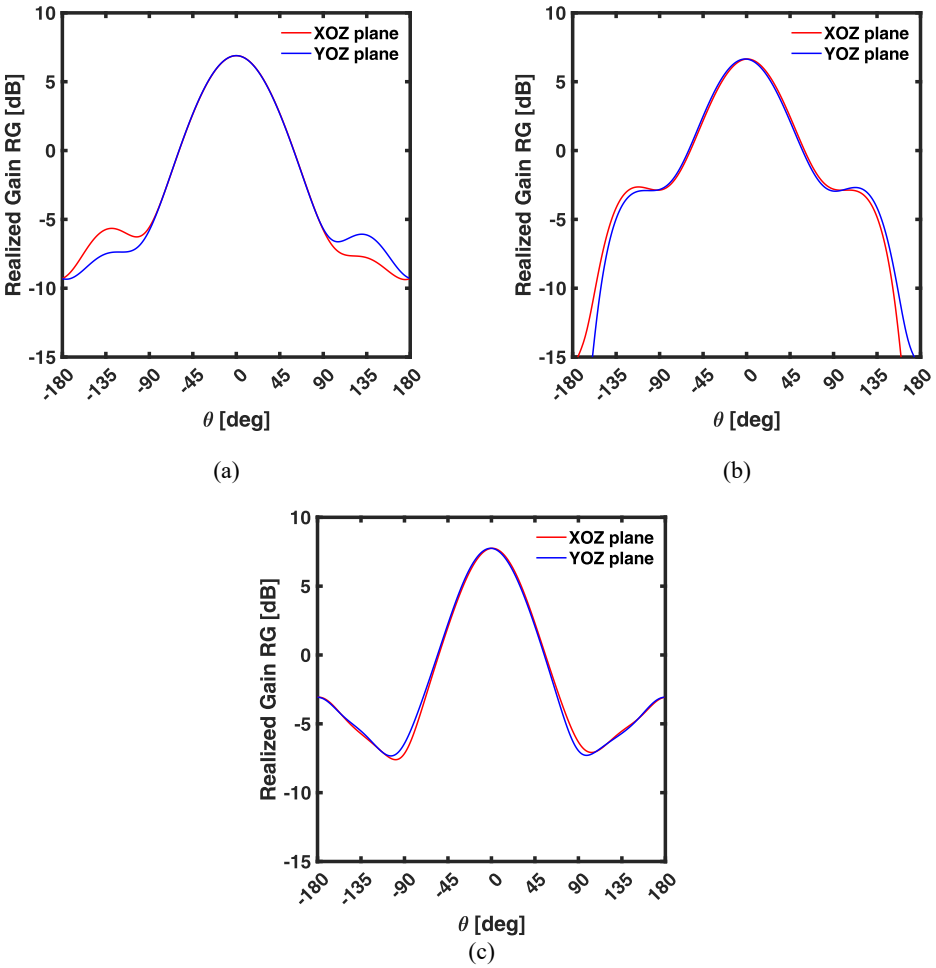

(a) (b)

(c)

Figure 4.19 Simulated realized gain G vs. θ for (a) f_L = 24 GHz [224]; (b) f_c = 27 GHz [224]; and (c) f_H = 30 GHz [224].

It is worth noting that, throughout the band, a stable radiation pattern is observed.

The main beam constantly directs to the boresight direction in case of all patterns. Moreover, the realized gain (RG) patterns show a high degree of symmetry. For all the frequencies, f, the YOZ plane radiation pattern shows approximate identity to the XOZ plane radiation pattern. A simulated half power beamwidth of HPBW $\geq 63.2^{o}$ is found in every case. At f_L = 24 GHz, f_c = 27 GHz and f_H = 30 GHz, the simulated side lobe levels are SLL_1 = - 12.5 dB, SLLc = - 9.3 dB and SLL_2 = - 10.8 dB respectively.

4.3.4 Comparison with other works

In terms of simulated impedance bandwidth (-10dB), BW and simulated peak gain, G_{max} ,the proposed antenna is compared with other related works presented in Table 4.6. In comparison with the works reported in the Table 4.6, the proposed antenna exhibits a highest simulated peak gain, G_{max} = 8.2 dB and a highest simulated fractional impedance bandwidth, BW_{ge} = 22.2% [212],[225],[226], [227],[228]. In case of simulated fractional impedance bandwidth, BW, the antenna of [226] is comparable with the proposed one but it has a lower simulated peak gain, G_{max} . Also, reference [212] shows similar simulated peak gain, G_{max} though it shows inferior performance in terms of simulated fractional impedance bandwidth, BW_i. By considering the promising results, it can be said that this antenna has effective potential to function as an ideal candidate in 5G wireless communication.

TABLE 4.6 COMPARISON WITH RELATED WORKS [224].

Reference	**Center Frequency, f_c (GHz)**	**Simulated −10 dB Impedance Bandwidth, BW_e (%) (GHz-GHz)**	**Simulated Peak Gain, G_{max} (dB)**
[212]	60	10.7% (57.2 - 63.7)	8
[225]	28	10.2% (26.73 - 29.6)	6.48
[226]	27	20% (24.2 - 29.5)	6.6
[227]	60	17.3% (55.3 - 65.7)	7.4
[228]	38	18% (35.4 - 43.1)	7.8
This work	27	22.2% (24 - 30)	8.2

4.3.5 Summary

For 5G mm-wave applications, a MS based slant (+45°) polarized ME dipole antenna is proposed in this research. This antenna supports a simulated impedance bandwidth of BW_i = 6 GHz (24-30 GHz) which completely overlaps with 2 dB realized gain bandwidth, BW_{ge} = 22.2% (24-30 GHz). Moreover, the simulated maximum realized gain, RG_{max} = 8.2 dB and the simulated radiation efficiency over the impedance bandwidth $\eta > 0.94$ enhance the demand of this proposed antenna. The suitability of this proposed antenna for 5G NR band applications is proved from all these features.

4.4 Conclusion

In microwave and mm-wave frequencies, the effectiveness of metasurface-based techniques in improving antenna bandwidth, structural compactness, gain and radiation characteristics is exploited in this chapter. The first part of this chapter shows the feasibility of low-cost fabrication of a PRS-based Fabry–Pérot antenna using unconventional materials while achieving wide gain bandwidth in the 7–9.5 GHz band and high gain (G_M = 13.2 dBi). The second part of this chapter demonstrates the usage of EBG in ME dipole antenna for suppressing unwanted surface modes to perfectly shape the radiation pattern while maintaining a wide impedance bandwidth of BW = 15 GHz and high radiation efficiency $\eta > 0.91$. The final part of this chapter shows how the integration of AMC in the ME dipole antenna successfully results high gain with retaining high bandwidth and high radiation efficiency in 5G mm-wave bands. It can be concluded that to realize high-gain, wideband, low-profile, and radiation-efficient antenna systems strategical design of engineered metasurfaces such as PRS, EBG, and AMC can be beneficial.

5 Wideband aperture coupled multi stacked antenna array

Widespread frequency coverage, along with strong polarization purity and high efficiency is often required for antennas used in modern RF systems. These challenges can be addressed by using wideband aperture-coupled multi-stacked antennas. By using stacked resonators, these antennas increase bandwidth. Moreover, by using aperture-based feeding, they can also improve isolation. This chapter presents the Ph.D. research related to aperture coupled multi stacked dual linear polarized antenna for satellite application.

5.1 Introduction

A Ku-band 2 × 2 stacked patch array is presented in this chapter for dual-polarized SOTM applications. Operation on terrestrial vehicles is the prime target of this antenna. Beam steering can be achieved mechanically by this antenna as the relative motion with respect to the satellite is sufficiently slow. Consequently, there is no requirement of implementing complex and expensive electronic scanning architectures [229]. The operating frequency band of this array is [10.7–14.5] GHz. This range covers both the Ku band uplink ([13.75–14.5] GHz) and downlink ([10.7–12.75] GHz) bands. A modular stacked-patch configuration forms the radiating structure. It is fabricated using low-loss dielectric substrates with standard-thickness. To ensure wide impedance bandwidth and robust im-

pedance matching, geometrical optimization has been performed. Sensitivity to manufacturing tolerances and operating conditions is thereby reduced.

Excitation of the array is achieved through a set of cross-shaped slots. The number of orthogonal slots defines the number of radiating elements in the array. The central ground plane having slot etched on it placed between two dielectric layers. Two compact, low-cost orthogonal microstrip dividers mounted on the external surfaces of these layers are used for exciting the slots as the intended application does not demand the rapid beam steering. For uniform power distribution and wideband impedance matching for each polarization, a multi-stage corporate-feed network is employed. Broadband T-junctions and cascaded quarter-wave transformers are used to design the feed network.

Excellent agreement between measured and simulated results is demonstrated through the experimental validation of the prototype, which confirms the proposed design's effectiveness. The antenna exhibits high resilience to fabrication tolerances in accordance with the design goals. To achieve this goal, neither high-precision manufacturing is employed nor expensive components are used. Considering the overall cost-effectiveness and manufacturability of the system, all layers are implemented using standard printed circuit board (PCB) technology.

The organisation of this chapter is as follows. Subsequent to this Introduction, the design architecture, the simulation setup, and the methodology adopted are described in Section 5.2. Sections 5.3, 5.4 demonstrate the simulated and measured results, respectively. Lastly, the key findings are reviewed, and future work direction is indicated in Section 5.5.

5.2 Antenna design

The sketch of the proposed 2 × 2 stacked patch array is presented in Figure 5.1. To prevent the occurrence of grating lobes at the highest frequency of the operating frequency range ($d \approx 0.8\lambda_{min}$), the inter-element spacing has been carefully set to d = 16.5 mm. The stacked architecture consists of four different PCBs and M4 nylon screws are used to ensure appropriate space between the layers. The confinement of the electromagnetic field within the dielectric substrates is minimized by the air gaps. Hence, the antenna's overall performance is enhanced in accordance with the principles outlined in [230],[231],[232] in terms of impedance bandwidth, gain, and radiation efficiency. The spacing between PCB 1 and PCB 2, and between PCB 2 and PCB 3, has been set to $h_{air_1} = h_{air_2} = 1.5$ mm shown in Figure 5.2. Nylon screws help to held PCBs 3 and 4 together which are stacked on top of each other. As listed in Table 5.1, the spacing between the bottom metal layer acting as a reflector and the PCB 4 has been set to $h_{air_3} = 8$ mm. The stacked PCBs and metal plate of the antenna are grouped by function, i.e. radiation, feeding, and reflection—to effectively explain the proposed design.

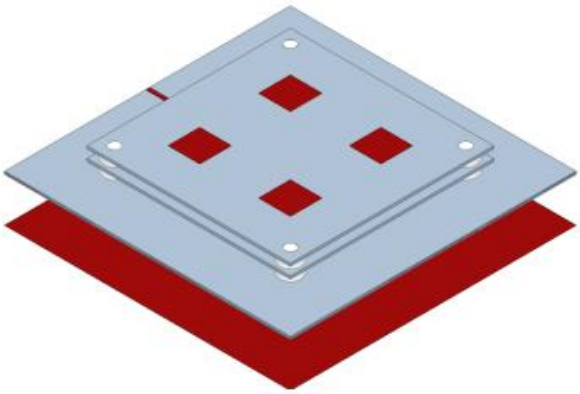

Figure 5.1 Geometry of the stacked patch antenna array [233].

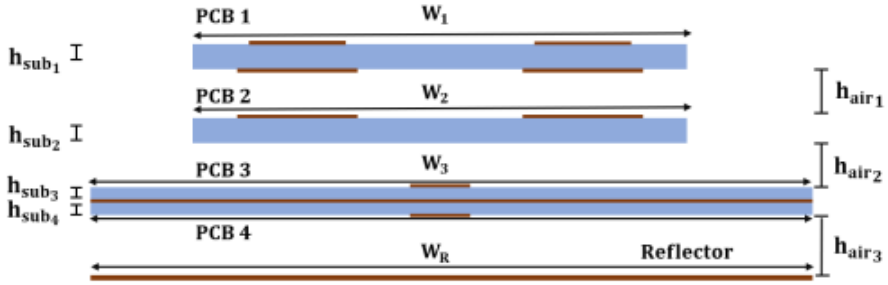

Figure 5.2 Side view of the antenna array stack-up. The structure consists of 4 PCBs and a metal plate, spaced by means of nylon spacers [233].

TABLE 5.1 STACK-UP DIMENSIONS [233].

Parameter	Value (mm)	Parameter	Value (mm)
h_{sub_1}	0.508	h_{air_1}	1.5
h_{sub_2}	0.508	h_{air_2}	1.5
h_{sub_3}	0.252	h_{air_3}	8
h_{sub_4}	0.252	$W_{1,2}$	37
$W_{3,R}$	52		

The stacked antenna consists of PCBs 1 and 2 which host the patches shown in Figure 5.2. These two PCB layers are based on low-loss Rogers RT/duroid 5880 substrates ($\epsilon_r = 2.2$, $\tan\delta = 9 \times 10^{-4}$), with a standard thickness of $h_{sub_1} = h_{sub_2} = 0.508$ mm. Each radiating element has these two substrates, and three square patches. On the top and bottom faces of PCB 1, The first two patches of lengths L_{patch_1} and L_{patch_2}, have been realized, respectively as shown in Figure 5.3. While the top face of PCB 2 contains the third patch having the length of L_{patch_3}. Table 2 listed the patches size. The coupling between the stacked antenna elements is enhanced by the presence of two patches on PCB 1. As a result, without increasing the manufacturing complexity, the overall performance is improved.

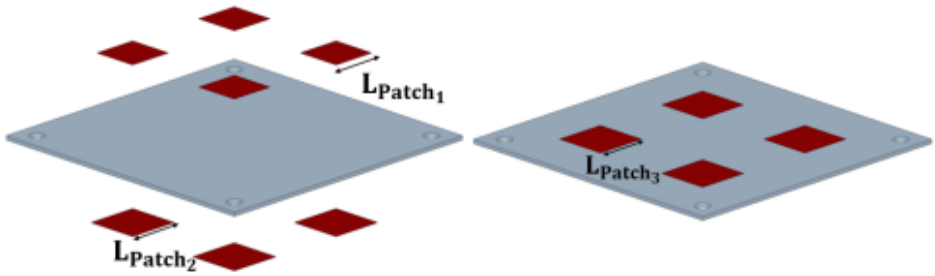

Figure 5.3 Hosting radiation patches PCBs. With reference to Figure 5.2, (left) PCB 1 and (right) PCB 2 [233].

The feeding system is hosted by the PCBs 3 and 4, shown in Figure 5.2. Three metal layers and two Rogers RT/duroid 5880 dielectric slabs having a thickness of $h_{sub_3} = h_{sub_4} = 0.252$ mm formed it. To accommodate the space needed for the coaxial connector, these PCBs are designed larger than the previous PCBs intentionally. Excitation of the array is achieved via four cross-shaped slots, which are etched in the central metal layer positioned between the two PCBs, each slot energises the corresponding radiating element. Figure 5.4 shows the feeding networks, where two orthogonal power dividers are designed in microstrip technology and realized on the external metals of the PCBs to excite these coupling slots.

By appropriately feeding the input ports of each feeding network, this configuration enables electronically reconfigurable dual polarization. Each linear polar-

ization is achieved by stimulating the associated arm of the cross slot using a pair of parallel fork-shaped microstrip lines. Figure 5.4 illustrates that the corresponding arms are extended beyond the slot center by the lengths $l_{stub_{1,2}}$, forming inductive stubs. To improve the impedance matching of the corresponding feeding network, the length of these stubs is set carefully. Figure 5.5 highlights that, T-shaped junctions composed of cascaded quarter-wave transformers based corporate feeding network is employed to achieve the high-impedance matching and broadband operation as these are the requirement of the design. Figure 5.5 illustrates the strategy of impedance matching. By connecting the quarter wave transformer stages consecutively and eliminating additional matched transmission line sections of length L between adjacent impedance transformation steps, an improved broadband matching near the design frequency f_0 is achieved. Table 5.2 reports the dimensions of the feeding network elements.

A metal plane is located at the bottom of the antenna stack-up, is working as a reflector, as shown in Figure 5.2. Suppression of the backward radiation generated by the aperture-coupled feeding mechanism, specifically the slots etched in the ground plane is critical. The reflector is placed in this design for this function.

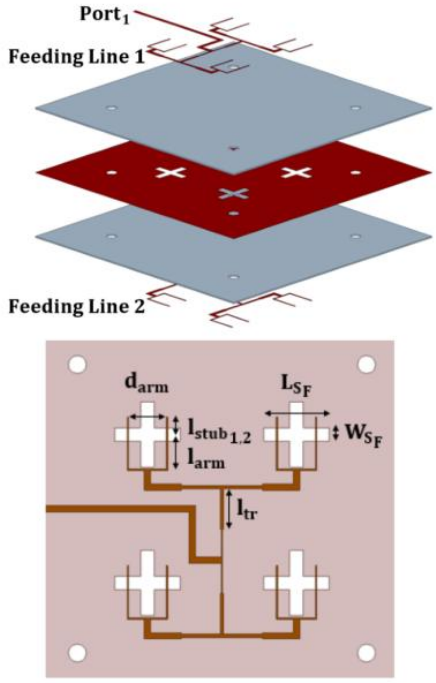

Figure 5.4 Feeding network: exploded view (top) and quoted layout (bottom). It consists of a ground plane embedded in the PCBs on which two orthogonal microstrip lines have been realized, one for each polarization, to properly excite the cross shaped slot etched in the ground plane [233].

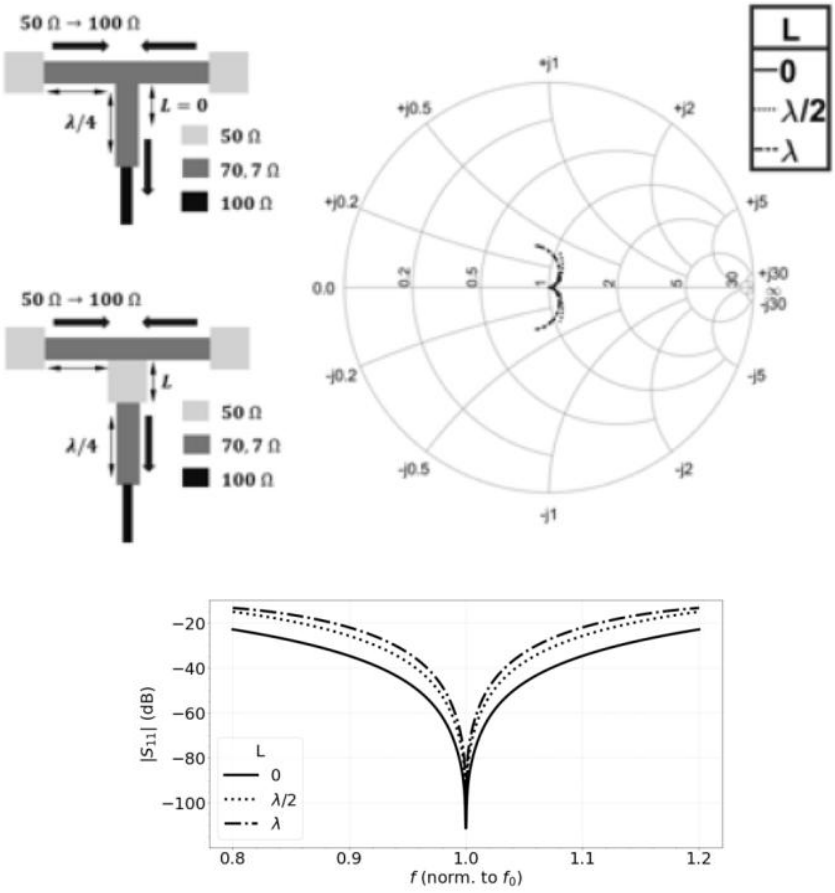

Figure 5.5 The configuration with continuous impedance transformation steps, without matched equivalent transmission line sections (L = 0), improves the broadband impedance matching level [233].

TABLE 5.2 PATCH AND FEEDING NETWORK DIMENSIONS [233].

Parameter	Value (mm)	Parameter	Value (mm)
L_{patch_1}	5.75	l_{stub_1}	1.8
L_{patch_2}	6.7	l_{stub_2}	1.95
L_{patch_3}	6.6	l_{tr}	4.5
L_{S_F}	7.25	W_{tr}	0.43
W_{S_F}	1.5	W_{50}	0.72
d_{arm}	4.5	W_{100}	0.21

5.3 Simulation results

Ansys Electronics Desktop software is used for optimizing and validating the proposed design through full wave simulation. The simulated results are shown in Figures 5.6 and 5.7, indicate that the antenna maintains good impedance matching, with both $|S_{11}|$ and $|S_{22}|$ consistently lower than −14.7 dB within the entire operating bandwidth of this research. Furthermore, high inter-port isolation is observed, with averaging better than $|S_{21}|_{avg}$ = 35 dB across the operating band and the minimum value of $|S_{21}|_{min}$ = −22 dB. Though, it is noted that, the highest $|S_{21}|$ level is observed at f_1 = 13.67 GHz, which is located just beyond the intended Ku-band SOTM uplink operating range. Across the frequency band, the broadside gain spans G_1 = 13 dB to G_2 = 14.5 dB. Also, at all reference frequencies, the radiated field for both port's excitation demonstrates a cross-polar discrimination greater than XPD_{th} = 20 dB. The results demonstrate proper reflector performance as it confirms the broadside gain level higher than the backscattering levels by 19 dB.

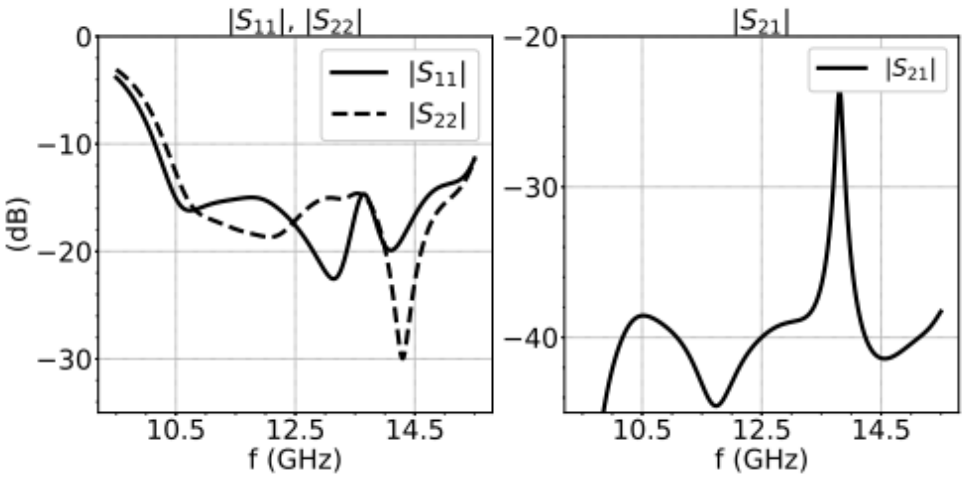

Figure 5.6 Simulated S-parameters of the proposed array [233].

As highlighted earlier, the antenna ensures reliable performance under varying environmental or operational conditions and also dimensional deviations induced by fabrication tolerances. The air gap heights between the substrates are specifically prone to low fabrication accuracy among all the geometric parameters. A careful investigation has performed to identify the impact of air gaps deviation from the optimal design configuration.

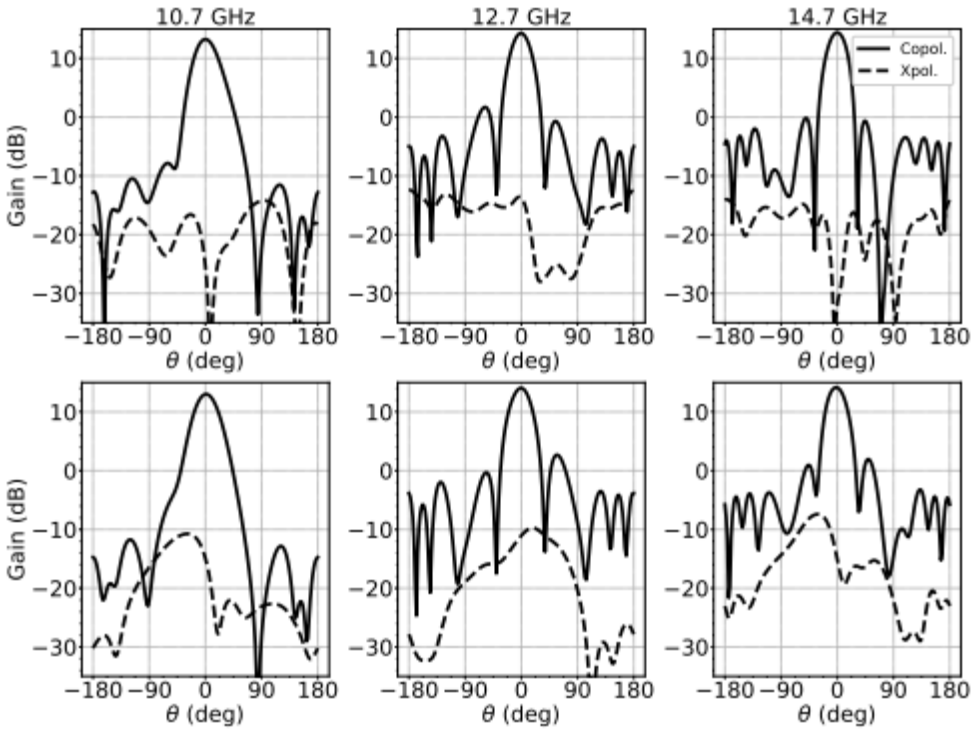

Figure 5.7 Simulated gain patterns on the H-planes at port 1 (top row) and port 2 (bottom row) [233].

One probable reason of these deviations can be the manufacturing tolerances of Nylon spacers, which lack the tight precision of dielectric substrates. Also, inaccuracies during assembly and to external operating conditions such as thermal effects can contribute to these discrepancies. Due to Nylon's high thermal expansion (~100 ppm/°C), it may induce significant structural variations from the intended design, especially if the antenna operates over −40 °C to +55 °C which is the standard SOTM operational temperature range. A sensitivity analysis has

been carried out on the air gap heights to evaluate the impact of such variations. The maximum relative deviation of 15% is considered from the nominal value. Figure 5.8 depicts the result analysis.

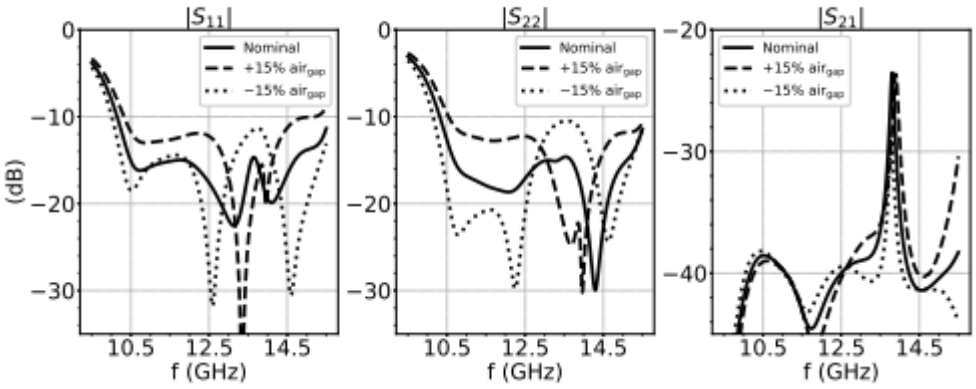

Figure 5.8 S-parameter tolerance analysis with respect to variations in air gap thickness of ±15% with respect to the nominal [233].

It is noted from Figure 5.8 that, the antenna maintains proper operation across the targeted frequency band even in the worst-case scenarios, when all spacer lengths are increased of 15%. Though a slight degradation of performance is observed in terms of impedance matching, but the mutual coupling between ports remains almost unaffected due to the design of the feeding system.

5.4 Fabrication and measurements

An LPKF Protolaser U3 is used to manufacture and subsequently characterize the proposed array. The fabricated protype is shown in Figure 5.9. Two metal

pads have been obtained on PCB 3 to guarantee proper electrical contact between the feeding coaxial shield and the ground plane of the array.

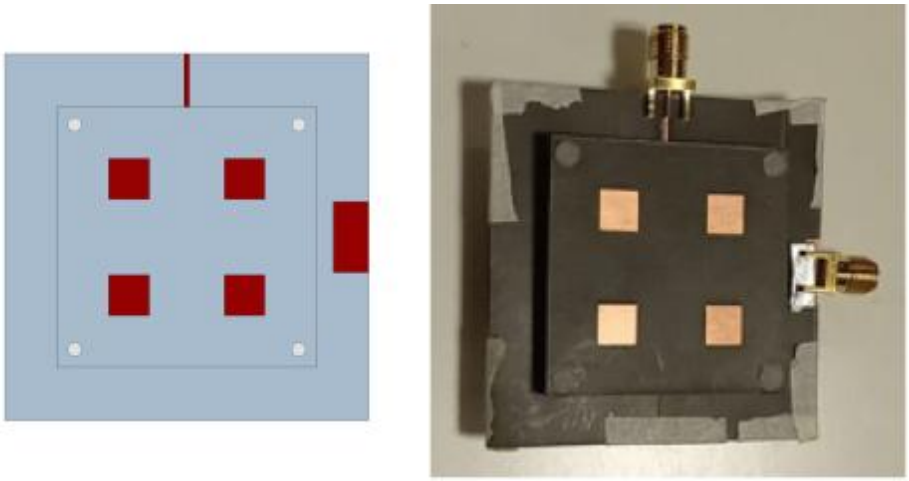

Figure 5.9 Simulated (left) and fabricated (right) stacked patch array [233].

A capacitive coupling between the antenna ground and the coaxial shield is provided by these pads. Though, the frequency response of the previously optimized antenna is affected due to the addition of these metal pads. In particular, the impedance-matching characteristic is changed. It is worth to mention that usage of metal pads is necessary to maintain good electrical contact when SMA connectors are used that do not have through-hole flanges. However, the addition of these metal pads becomes unnecessary during usage of SMA connectors with mounting screws as proper contact is already ensured by the screws that fasten the connector to the substrate. The measurements carried out on the prototype exhibit good consistency with the results obtained from full-wave simulations of the array including the metallic pads. The full-wave simulated results of the array

where the metallic pads are considered show a good consistency with the measured result obtained from the prototype.

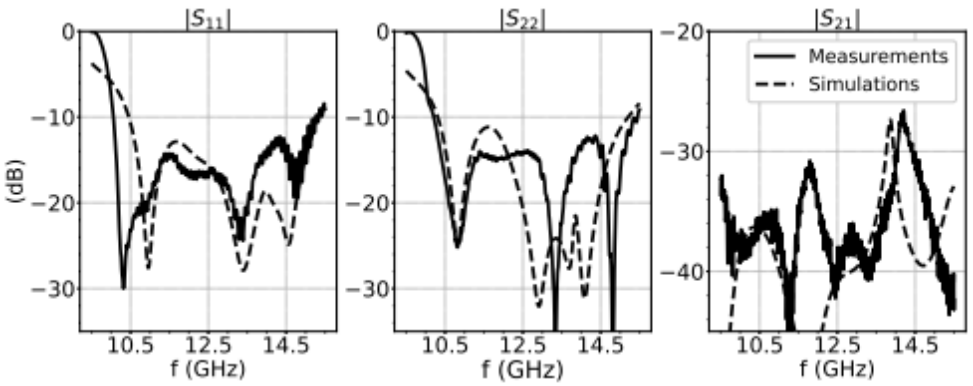

Figure 5.10 Comparison of measured and simulated S-parameters. The graphs show good agreement between the experimental and predicted results [233].

Like the simulated scattering parameters, the measured ones also confirm that the array covers the whole required frequency band, as shown in Figure 5.10. Figure 5.11 depicts the measurement set up of the anechoic chamber for evaluating the radiating performance of the fabricated prototype. As a reference calibrated antenna, a HF907 horn has been adopted. The measured data align with the simulations with a minor deviation in case of cross polar discrimination i.e. the difference between the co polar and cross polar levels relative to expectations as reported in Figure 5.12.

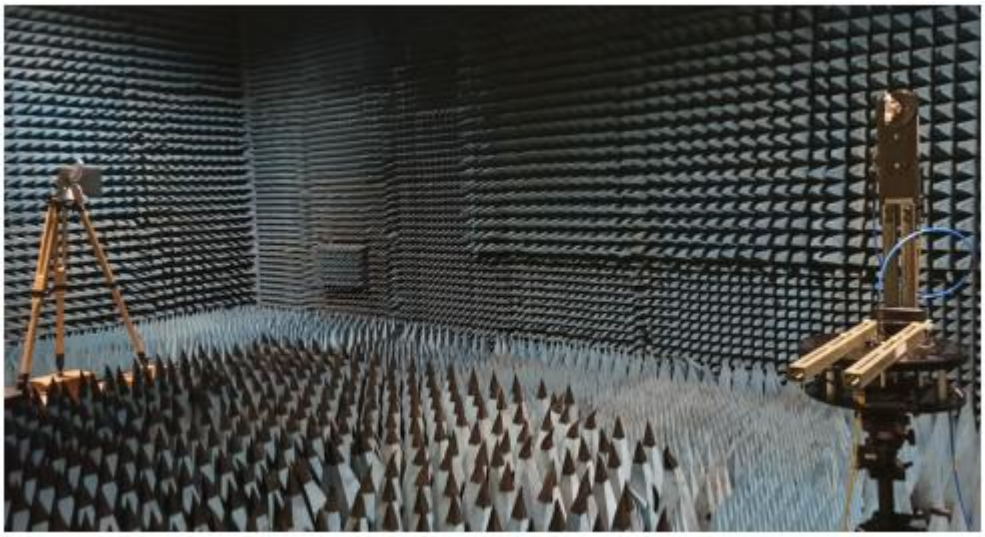

Figure 5.11 Experimental setup adopted for the prototype measurement [233].

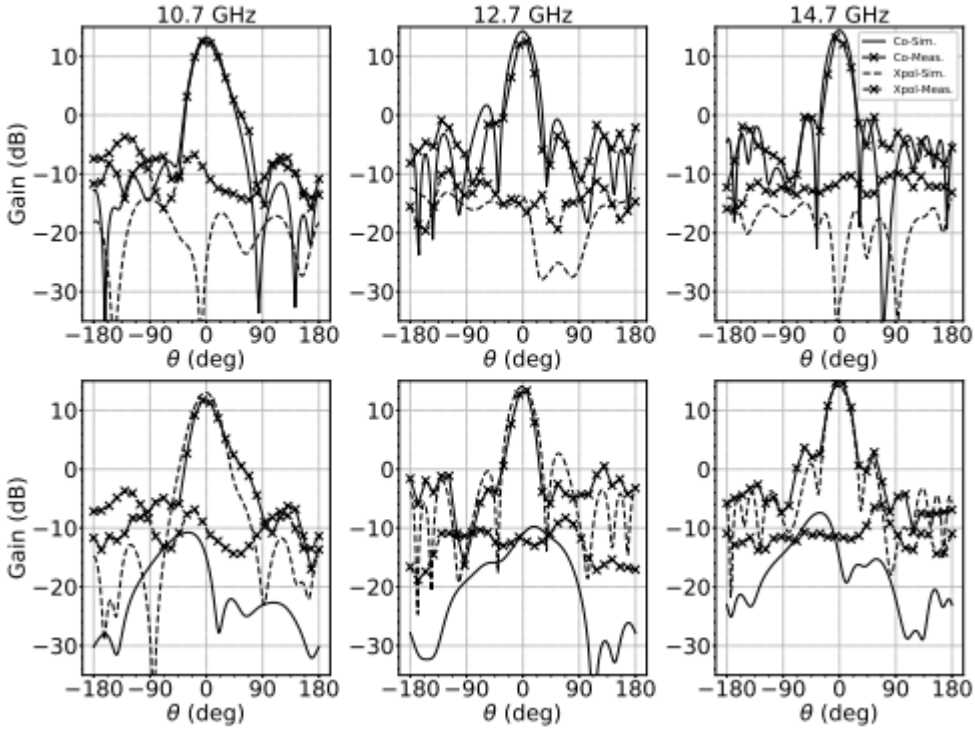

Figure 5.12 Comparison between measured and simulated gain patterns on the H-planes at port 1 (top row) and port 2 (bottom row) [233].

5.5 Discussion

The design objectives defined for the target SOTM application is perfectly achieved by the proposed antenna. It has some features like excellent port-to-port isolation, high XPD, and stable impedance matching across the entire oper-

ating band and it supports electronically reconfigurable polarization architecture also. The proposed simple and modular structure achieves these performances while maintaining strong robustness against process tolerances and different operational conditions, reduced manufacturing cost and low fabrication complexity simultaneously. The reliability of the design is further confirmed by the close agreement between simulated and measured results, regardless of manufacturing the prototype without industry standard as strict tolerance control is not maintained. The comparison among the proposed array and other representative antennas operating in the X and Ku bands, suitable for similar applications is presented in Table 5.3 to highlight the achieved performance. The comparison is meaningful in terms of both electromagnetic performance and implementation complexity as the operating frequencies of reference antennas are comparable. Although multiple patch antennas at similar frequencies have been reported, including stacked configurations [234],[235],[236],[237], none of them achieved all key SOTM requirement unlike the proposed antenna which makes it distinct. Electronically switchable dual polarization feature is not present in compact arrays reported in the literature, and in one research like [234] depends on even mechanical tilting for broadside radiation realization. Furthermore, adequate bandwidth to cover simultaneously both uplink and downlink bands is lacking in several reported designs, whereas some design rely on oversized single element which is inappropriate due to its adverse effect on radiation pattern i.e. generation of grating-lobe. In comparison with previously reported dual-polarized stacked patch antennas operating at lower frequencies (around 2.4 GHz) [230],[232], this proposed antenna array realizes similar mechanical simplicity and modularity though it operates at higher frequency band. A simplified material stack is implemented where only two standard dielectric substrate thicknesses with uniform air gaps are used which eradicates the necessity of utilizing

foam layer. Moreover, the presence of a third radiating patch enables further performance optimization of the antenna. The realized 2 × 2 dual-polarized array outperforms other comparable designs as it provides input reflection coefficients below −15 dB over the operating band while maintaining interport isolation more than 35 dB. Additionally, the extension from the individual element to 2 × 2 array does not alter the outstanding performance in terms of impedance matching, isolation and radiation characteristics due to the presence of a compact corporate-feed network. In order to maximize the impedance matching, the feeding network design method follows the previously outlined transformation principles while preserving both symmetry and easiness of layout scalability. In comparison with more complex architectures such as [238], superior electromagnetic behaviour and optimization efficiency are achieved by this array regardless of its simplicity.

Lastly, for the stacked architecture, preference is given to nylon screws over foam layers or metallic rings. The reason behind this choice is to eliminate the adhesives utilization, commonly seen in architecture based on the latter alternatives, which can degrade under dynamic motion or vibrational conditions. Furthermore, the most cost effective and versatile solution among these three is the screw-based architecture. Also, this configuration facilitates precise control over inter-layer distances, permitting correction of small deviation introduced from fabrication tolerances or operating conditions. Overall, this antenna maintains low manufacturing complexity and cost having features of wide impedance bandwidth, high polarization purity, and strong port isolation.

TABLE 5.3 COMPARISON WITH LITERATURE [233].

Ref.	Antenna type	FBW(%) (fc GHz)	Iso. (dB)	Pol.	XPR (dB)	Gain (dBi)	Dim. (mm^3) (λ_c^3)	Fab. Compl.
[234]	4 × 4 [1]SPA	33.3 (10.50)	//	[2]SL	NA	20*	125 × 125 × 3.5 (4.38 × 4.38 × 0.12)	Low
[235]	1 × 16 [1]SPA	20.57 (16.72)	//	[2]SL	NA	19	181 × 15 × 3.3 (10.1 × 0.84 × 0.18)	Low
[236]	Patch Antenna	40 (15.05)	//	[2]SL	25	19	20 × 32 × 1.5 (1 × 1.6 × 0.075)	Low
[237]	DGS Patch Antenna	58.72 (11.75)	//	[2]SL	16	5	60 × 60 × 3 (2.35 × 2.35 × 0.12)	Low
[238]	2 ×2 [1]SPA	27 (13.75)	31	[3]DL	34	NA	NA × NA × 9.3 (NA × NA × 0.43)	Low
[239]	4 × 4 Waveguide	32 (12.50)	21.7	[3]DL	25	21	92 × 92 × 45 (3.83 × 3.83 × 1.88)	High
[240]	Cavity Antenna	40 (10.00)	23	[3]DL	20	5.8	1.32× 1.32 × 11.7 (0.44 × 0.44 × 0.39)	[4]Med.
[241]	Slot Antenna	20 (10.00)	28	[3]DL	22	5.3	44.1 × 44.1 × 3.9 (1.47 × 1.47 × 0.13)	[4]Med.
[242]	6 × 6 Slot Array	30 (12.85)	33	[3]DL	28	23	120 × 120 × 21.1 (5.14 × 5.14 × 0.9)	High
This Work	2 × 2 [1]SPA	41 (13.00)	22**	[3]DL	20	14	54 × 54 × 12.5 (2.34 × 2.34 × 0.54)	Low

[1]SPA = Stacked Patch Array. [2]SL = Single linear. [3]DL= Dual linear.[4]Med.=Medium. * Pointing direction 20◦. **Average isolation in the actual bands of interest for SOTM is > 35 dB.

Circular polarization can also be accomplished due to the symmetric layout of the radiating elements and the identical impedance matching at both ports. An axial ratio below 1.25 dB across the band can be attained by properly phasing the two input ports. These characteristics highlight the polarization flexibility of this design and prove it a cost-effective and strong candidate for SOTM applications as it provides either similar or better performance than other architectures having more structural complexity.

5.6 Conclusion

A stacked 2 × 2 patch array having dual polarized operation is deigned, fabricated and characterized for satellite-on-the-move (SOTM) application. It covers both uplink and downlink SATCOM bands as it operates over the [10.7 - 14.5] GHz frequency range. A combination of robust performance with structural simplicity is presented by the proposed architecture. The close agreement between the full wave simulations with experimental measurements proves its effectiveness in mobile satellite communication systems for dual-polarized and high-performance operation.

Conclusions

In this Ph.D. thesis, novel antenna systems have been designed, fabricated, and experimentally characterized for microwave communication applications, including IoT, satellite-on-the-move, and 5G. The following points highlight the summarized results and important aspects related to planar transmitarray antenna:

- The design presents a dual polarized, high gain, beam steering low profile transmitarrays for next generation wireless communication networks.
- Multiple phase-compensating layers based planar transmitarray antenna has been designed which exhibits high gain (G_{m0} = 21 dB) and has the capability of beam steering up to ±30° at Ku band.
- Experimental results confirm the accuracy of simulated results, in particular, low side lobe level SLL_1 = −20.8 dB based radiation pattern is observed. Also, low scan loss of $\triangle G_{MSL1}$ = 2.73 dB proves its feasibility in beam steering application.
- Low transmission loss and 3-bit phase compensation are ensured with compact architecture (thickness, $\rho = 0.126\lambda_0$), providing a rational choice to traditional transmitarray.

The key aspects of low cost based Fabry–Pérot cavity antenna are:

- A PRS based Fabry–Pérot cavity antenna has been fabricated using a hybrid fabrication technique consisting of both inkjet printing and 3D printing technology for low-cost production.

- Coherent with simulated result, a maximum gain of ~13.2 dBi and a 3 dB gain bandwidth of 24.5% are measured due to the constructive interference within the cavity.

The key points of EBG and AMC structures based wideband magneto-electric dipole antennas are:

- The EBG based ME dipole antenna achieves wide impedance bandwidth of BW = 42.4% with a maximum gain of G_{max} = 8.2 dB.
- A metasurface (AMC) based slant-polarized ME dipole provides 2 dB realized gain bandwidth of BW_{ge} = 22.2% (24-30 GHz) and a radiation efficiency of $\eta > 0.94$ over the impedance bandwidth.
- Integration of EBG causes a reduction of side-lobe levels through suppressing unwanted surface modes.
- Incorporation of the AMC structures enables in phase reflection while maintaining a comparatively lower height of the magnetic dipole results a reduction of the overall profile.

The main features related to wideband patch arrays for SOTM applications include:

- A stacked 2 × 2 patch array having dual polarized operation is designed for satellite-on-the-move systems, having a high fractional bandwidth of FBW = 41% [10.7 GHz - 14.5 GHz] with an isolation, $|S_{2,1}|$ more than 35 dB between two ports.
- Low profile architecture and low fabrication complexity makes this antenna array demanding.

- High gain of G = 14dBi and cross polar ratio of XPR = 20 dB ensures its suitability in next-generation wireless communication technologies.

Though robust frameworks have been established for transmitarray, Fabry-Pérot cavity, ME dipole, and wideband patch array antenna in this thesis, several promising options remain for extending the performance and versatility of these systems. For example, integration of electronic components in the transmitarray for enabling dynamic beam steering, frequency tuning, and polarization control can be a potential future research direction. Furthermore, for beam steering applications, investigating the feasibility of applying amplitude taper methods in the design process of the transmitarray can be fruitful for further reduction of the side lobe level. In case of Fabry-Pérot cavities, conformal architecture, flexible metasurfaces, and antennas of unconventional shape, difficult to fabricate through traditional techniques, can be explored. The developed ME dipole antennas can be extended to design phased array antenna for beam steering application. Also, for controlling the polarization of the developed wideband patch array, which is crucial for SATCOM applications, the incorporation of electronic circuitry can be performed through proper phasing in both ports.

The obtained results have been published in international journals and presented at national and international conferences, as listed in the next paragraph.

List of publications

International Journals:

[j1] M. I. Khan, A.M. Loconsole, F. Anelli, V.V. Francione, A.U. Khan, M. Simone, G. Sorbello, F. Prudenzano, "A Low-Profile Dual-Polarized Transmitarray with Enhanced Gain and Beam Steering at Ku Band," *Applied Sciences*, 15(9):4656, 2025,doi:10.3390/app15094656.
[j2] F. Anelli, A. M. Loconsole, V. V. Francione, M. I. Khan and F. Prudenzano, "Cost-Effective Fabry–Pérot Antenna via Conductive Inkjet and Additive Printing," in *IEEE Antennas and Wireless Propagation Letters*, vol. 24, no. 8, pp. 2182-2186, Aug. 2025, doi: 10.1109/LAWP.2025.3557941.
[j3] D. Guarnera, M. Simone, A. M. Loconsole, M. I. Khan, F. Anelli, S. C. Pavone, F. Prudenzano, G. Sorbello, "Design of a Dual-Polarised Wide-Band Stacked-Patch Array for Ku Band Satcom On-the-Move," IET Microwaves, Antennas & Propagation: e70081., 2026.,doi: 10.1049/mia2.70081.

Proceedings of International Conferences (= presenter)*:

[c1] M. I. Khan (*), F. Anelli, A. M. Loconsole, V. V. Francione and F. Prudenzano, "Ultra-Thin Metasurface for High Gain and Beam Steering at 5G Millimeter Wave Applications," *2024 24th International Conference on Transparent Optical Networks (ICTON)*, Bari, Italy, 2024, pp. 1-4, doi: 10.1109/ICTON62926.2024.10648279.
[c2] M. I. Khan (*), A. M. Loconsole, F. Anelli, V. V. Francione and F. Prudenzano, "A Wideband Magneto-Electric Dipole Based Slant Polarized Antenna with Metasurface",*2025 IEEE International Conference on Antennas and Applications*, Antibes, France, 2025.
[c3] M. I. Khan (*), F. Anelli, A. M. Loconsole, V. V. Francione and F. Prudenzano, "A Wideband Magneto-Electric Dipole Antenna with Electromagnetic Bandgap Structure",*2025 IEEE International Conference on Antennas and Applications*, Antibes, France, 2025.

[c4] A. M. Loconsole, V.V. Francione, A. Annunziato, F. Anelli; M. I. Khan; S. Taccheo, "Design of a praseodymium-doped fluoroindate fiber amplifier for medium infrared wavelength range applications," *2024 24th International Conference on Transparent Optical Networks (ICTON)*, Bari, Italy, 2024, pp. 1-4.
[c5] F. Anelli, A. Annunziato, A. M. Loconsole, V. V. Francione, M. I. Khan; S. Cozic, "Indium Fluoride Optical Fiber End-Pump Combiner for High-Power All-Fiber Sources," *2024 24th International Conference on Transparent Optical Networks (ICTON)*, Bari, Italy, 2024, pp. 1-4.
[c6] F. Anelli, A. Annunziato, A. M. Loconsole, V. V. Francione, M. I. Khan, S. Cozic, "Enhancing Sensing Capabilities: Fabrication of Tapered Optical Fiber Sensors in Fluoride Glasses," *2024 24th International Conference on Transparent Optical Networks (ICTON)*, Bari, Italy, 2024, pp. 1-4.
[c7] A. M. Loconsole, V. V. Francione, A. Annunziato, F. Anelli, M. I. Khan, S. Taccheo, F. Prudenzano, "Design of a mid-IR optical fiber amplifier based on a Pr3+:InF3 glass," Proc. SPIE 13003, Fiber Lasers and Glass Photonics: Materials through Applications IV, 130030J,20 June 2024.

International Conferences (= presenter)*:

[c1] F. Anelli, A. M. Loconsole, V.V. Francione, M. I. Khan, F. Prudenzano, "Inkjet-printed antennas: from simple structures to complex resonators," *20th International Conference on Microwave and High Frequency Applications*, Bari, Italy,2025.
[c2] A. M. Loconsole, F. Anelli, V.V. Francione, M. I. Khan, F. Prudenzano, "Microwave needle applicators for cancer therapy: a low-cost and mini-invasive solution," *20th International Conference on Microwave and High Frequency Applications*, Bari, Italy,2025.
[c3] M. Simone, D. Guarnera, A. M. Loconsole, M. I. Khan, S. C. Pavone, F. Prudenzano, G. Sorbello, "Two stacked planar antennas for satellite applications" *20th International Conference on Microwave and High Frequency Applications*, Bari, Italy,2025.

National Conferences (= presenter)*:

[n1] F. Anelli, V. V. Francione, M. I. Khan, A. M. Loconsole, "Fabrication and Characterization of Micro-Tapered Long Period Gratings on Zirconium Fluoride Optical Fiber for Mid-Infrared Applications," XXV Riunione Nazionale di Elettromagnetismo (RiNEm 2024),Viareggio, Italy, 2024.

[n2] A.M. Loconsole, V. V. Francione, F. Anelli, M. I. Khan, Adham Mahmoud (University of Rennes), Mauro Ettorre, Francesco Prudenzano " Design and Fabrication of an Air-Filled Substrate Integrated Waveguide Antenna Array," XXV Riunione Nazionale di Elettromagnetismo (RiNEm 2024),Viareggio, Italy, 2024.

References

[1] Gurbet, Y.S., Doğu, S., "Comprehensive Review of Ku, K, and Ka Band Antenna Designs: Applications in CubeSats," *Int. J. Aeronaut. Space Sci.*, vol. 27, pp. 447–496, 2026.

[2] Yang Y, Mao M, Xu J, Liu H, Wang J, Song K., "Millimeter-Wave Antennas for 5G Wireless Communications: Technologies, Challenges, and Future Trends," *Sensors*, vol. 25, 5424, 2025.

[3] Mehmood F, Mehmood A. "Recent Advancements in Millimeter-Wave Antennas and Arrays: From Compact Wearable Designs to Beam-Steering Technologies," *Electronics*., vol. 14, 2705, 2025.

[4] M. A. Belen *et al.*, "Optimal Design of Transmitarray Antennas via Low-Cost Surrogate Modelling," *Sci. Rep.*, 2023.

[5] R. De Marco, L. Boccia, G. Amendola, E. Arnieri, F. Greco and A. Bordbar, "Low Profile Dual-Band Dual-Polarized Transmitarray Antenna for Satellite Communications," *2023 17th European Conference on Antennas and Propagation (EuCAP)*, Florence, Italy, 2023, pp. 1-4.

[6] A. Clemente, M. Smierzchalski, F. F. Manzillo and T. Le Nadan, "Experimental Characterization of a Low-Profile 37-dBi Gain Transmitarray for Backhauling at E-Band," *2023 IEEE International Symposium on Antennas and Propagation and USNC-URSI Radio Science Meeting (USNC-URSI)*, Portland, OR, USA, 2023, pp. 23-24.

[7] Eyman PourMohammadi, Hassan Naseri, Noureddine Melouki, Fahad Ahmed, Qi Zheng, Amjad Iqbal, Tayeb A. Denidni, "A wideband beam

steering transmitarray antenna for Ka-band applications," *AEU - International Journal of Electronics and Communications*, vol. 193, 155720, 2025.

[8] N. Melouki, A. Hocini, F. Z. Fegriche, P. PourMohammadi, H. Naseri, A. Iqbal, and T. A. Denidni, "High-Gain Wideband Circularly Polarised Fabry–Perot Resonator Array Antenna Using a Single-Layered Pixelated PRS for Millimetre-Wave Applications," *Micromachines*, vol. 13, no. 10, Art. 1658, 2022.

[9] D. *et al.*, "Design of a Planar, High-Gain, Substrate-Integrated Fabry–Perot Cavity Antenna at Terahertz Frequency," *Current Applied Physics*, vol. 15, no. 9, pp. 1047–1053, 2015.

[10] M. F. El-Sewedy and M. Abdalla, "Wideband and high-directive reflective metasurface-based Fabry–Perot cavity antennas," *Int. J. Microw. Wireless Technol.*, 2022.

[11] Cai L, Tong KF. "A Single-Fed Wideband Circularly Polarized Cross-Fed Cavity-Less Magneto-Electric Dipole Antenna," *Sensors (Basel),* vol. 23, 1067, Jan 2023.

[12] Y. -L. Yu and Y. -L. Ban, "Low-Profile Wideband Magneto-Electric Dipole Antenna with AMC," *2022 IEEE MTT-S International Wireless Symposium (IWS)*, Harbin, China, 2022, pp. 1-3.

[13] J. Sun and K. -M. Luk, "Wideband Linearly-Polarized and Circularly-Polarized Aperture-Coupled Magneto-Electric Dipole Antennas Fed by Microstrip Line With Electromagnetic Bandgap Surface," in *IEEE Access*, vol. 7, pp. 43084-43091, 2019.

[14] Liao L, Li Z, Tang Y, Chen X., "Dual-Polarized Stacked Patch Antenna for Wireless Communication Application and Microwave Power Transfer," *Electronics*, vol. 10, 2988, 2021.

[15] Karami F, Rezaei P,Amn-e-Elahi A, Abolfathi A, A. Kishk, "Broadband and efficient patch array antenna fed by substrate integrated waveguide feed network for Ku-band satellite applications," *Int J RF MicrowComput Aided Eng.*, vol. 31, e22772, 2021.

[16] C. A. Balanis, *Antenna Theory: Analysis and Design*, 4th ed., Wiley, 2016.

[17] S. S. Holland and R. C. Johnson, "The slotted waveguide array: An experimental and theoretical study," *IEEE Transactions on Antennas and Propagation*, vol. 9, no. 3, pp. 219–225, May 1961.

[18] R. J. Mailloux, *Phased Array Antenna Handbook*, 2nd ed., Artech House, 2005.

[19] L. Zhang *et al*, "Demonstration of a Wideband Multipolarization Transmitarray Antenna for Satellite Communication," *International Journal of RF and Microwave Computer-Aided Engineering*, vol. 2023, no. 1, May. 2023.

[20] Hamza Kaouach, "Design and demonstration of 1-bit and 2-bit transmitarrays at X-band frequencies," *Progress in Electromagnetics Research*, vol. 5, pp. 731-736, 2009.

[21] A. H. Abdelrahman, A. Z. Elsherbeni, and F. Yang, "Transmission Phase Limit of Multilayer Frequency-Selective Surfaces for Transmitarray Designs," *IEEE Transactions on Antenna and Propagation*, vol. 62, no. 2, pp. 690–697, Feb. 2014.

[22] W. An, S. Xu, F. Yang, and M. Li, "A Double-Layer Transmitarray Antenna Using Malta Crosses with Vias," *IEEE Transactions on Antenna and Propagation*, vol. 64, no. 3, pp. 1120–1125, Mar. 2016.

[23] A. H. Abdelrahman, "Critical Analysis of Transmitarray Antenna Design," *University of Mississippi Electronic Theses and Dissertations*, 2014.

[24] X. Wang, P.-Y. Qin, Anh Tuyen Le, H. Zhang, R. Jin, and Y. Jay Guo, "Beam Scanning Transmitarray Employing Reconfigurable Dual-Layer Huygens Element," *IEEE Transactions on Antennas and Propagation*, vol. 70, no. 9, pp. 7491–7500, Sep. 2022.

[25] M. Chen, A. Epstein, and G. V. Eleftheriades, "Design and Experimental Verification of a Passive Huygens' Metasurface Lens for Gain Enhancement of Frequency-Scanning Slotted-Waveguide Antennas,"

IEEE Transactions on Antennas and Propagation, vol. 67, no. 7, pp. 4678–4692, Jul. 2019.

[26] Z. X. Wang *et al.*, "Broadband and Ultrathin Huygens Metasurface with High Transmittance," *Journal of Physics D: Applied Physics*, vol. 53, no. 45, p. 455102, Aug. 2020.

[27] M. Chen, M. Kim, A. M. H. Wong, and G. V. Eleftheriades, "Huygens' Metasurfaces from Microwaves to optics: a Review," *Nanophotonics*, vol. 7, no. 6, pp. 1207–1231, Jun. 2018.

[28] Iman Derafshi and Nader Komjani, "A New High Aperture Efficiency Transmitarray Antenna Based on Huygens Metasurfaces," *IEEE Transactions on Antenna and* 94 *Propagation*, vol. 70, no. 7, pp. 5458–5467, Jul. 2022.

[29] A. Epstein, J. K. Wong, and G. V. Eleftheriades, "Cavity-excited Huygens' Metasurface Antennas for near-unity Aperture Illumination Efficiency from Arbitrarily Large Apertures," *Nature Communications*, vol. 7, no. 1, Jan. 2016.

[30] A. H. Abdelrahman, Payam Nayeri, A. Z. Elsherbeni, and F. Yang, "Bandwidth Improvement Methods of Transmitarray Antennas," *IEEE Transactions on Antenna and Propagation*, vol. 63, no. 7, pp. 2946–2954, Apr. 2015.

[31] Y. Zhao, Y. Lin, L. Jiang, and P. Li, "Design and implementation of a novel wideband dual-polarised transmitarray antenna based on tightly coupled cross dipole cells," *IET Microwaves, Antennas & Propagation*, vol. 18, no. 12, pp. 1011–1023, Nov. 2024.

[32] M. Ghaderi and P. Rezaei, "Analytical Design of Low-Profile Wideband Multi-Layer Transmitarray Antenna for Ku Band," *Wireless Networks*, 2024. [Online]. Available: https://doi.org/10.1007/s11276-024-03870-7.

[33] Y. Cao, M. Zhang, C. Fan, and J. Chen, "A Broadband Transmitarray Antenna Using a Metasurface-Based Element for Millimeter-Wave Applications," *Micromachines*, vol. 15, no. 3, p. 383, 2024.

[34] L. Chen, Y. Ge, and T. Bird, "Ultrathin Flat Microwave Transmitarray Antenna for Dual-Polarised Operations," *Electronics Letters*, vol. 52, no. 17, pp. 1433–1435, Aug. 2016.

[35] M. Sun et al., "Reconfigurable Transmitarray Based on Frequency Selective Surface for 2D Wide-Angle Beam Steering," *Electronics*, vol. 12, no. 18, p. 3854, Sep. 2023.

[36] A. Gülseren, A. Alparslan and N. Tokan, "Dual-Band Frequency Selective Surface Backed Reflectarray for High-Speed Ka-Band Satellites," *Applied Sciences*, vol. 14, no. 7, p. 2928, March. 2024.

[37] D. R. Jackson, C. Caloz, and T. Itoh, "Leaky-Wave Antennas," *Proceedings of the IEEE,* special issue on Antennas in Wireless Communications, K. M. Luk and K. F. Lee, Editors, vol. 100, no. 7, pp. 2194-2206, Jul. 2012.

[38] G. von Trentini, "Partially reflecting sheet arrays," *IEEE Trans. Antennas Propagat,* vol. 4, pp. 666–671, Oct. 1956.

[39] A. P. Feresidis and J. C. Vardaxoglou, "High gain planar antenna using optimised partially reflective surfaces," *IEE Proc. Microwave Antennas Propagat.,* vol. 148, pp. 345–350, Dec. 2001.

[40] A. F. Pan, F. Feresidis, and J. C. Vardaxoglou, *Modern Antenna Handbook*, "Leaky-Wave and Fabry-Pérot Cavity Antennas," Chap. 7, Wiley, pp. 357–358, 2011.

[41] C. Mateo-Segura, A. P. Feresidis and G. Goussetis, "Broadband leaky-wave antennas with double-layer PRS: analysis and design," *European Conf. on Antennas and Propagation (EuCAP)*, Apr. 11–15, 2011.

[42] F. Capolino and D. R. Jackson, "Directive Fabry-Pérot Cavity Leaky-Wave Antennas: History, Design and Theory," Short Course given at the IEEE AP-S Intl. Symp., Chicago, IL, Jul. 8–14, 2012.

[43] L. Moustafa and B. Jecko, "EBG structure with wide defect band for broadband cavity antenna applications," *IEEE AWPL,* vol. 7, pp. 693–696, Nov. 2008.

[44] Y. F. Lu and Y. C. Lin, "Design and implementation of broadband partially reflective surface antenna," *IEEE AP-S Intl. Symp.*, Spokane, WA, Jul. 3 - 8, 2011.

[45] A. P. Feresidis and J. C. Vardaxoglou, "A broadband high-gain resonant cavity antenna with single feed," *European Conf. on Antennas and Propagation (EuCAP)*, Nice, France, Nov. 6–10, 2006.

[46] Z. G. Liu, W. X. Zhang, D. L. Fu, Y. Gu and Z. C. Ge, "Broadband Fabry-Pérot resonator printed antennas using FSS superstrate with dissimilar size," *Microw. Opt. Technol. Lett.,* vol. 50, no. 6, pp. 1623–1627, Jun. 2008.

[47] C. Mateo-Segura, A. P. Feresidis and G. Goussetis, "Highly directive 2-D leaky wave antennas based on double meta-surfaces," *European Conf. on Antennas and Propagation (EuCAP)*, Barcelona, Spain, Apr. 12 –16, 2010.

[48] A. Foroozesh and L. Shafai, "Investigation into the effects of the reflection phase charactersitics of highly-reflective superstrates on resonant cavity antennas," *IEEE Trans. Antennas Propag.,* vol. 58, no. 10, pp. 3392–3396, Oct. 2010.

[49] M. A. Al-Tarifi, D. E. Anagnostou, A. K. Amert and K. W. Whites, "Multiple superstrates technique for a broadband cavity resonance antenna (CRA)," *IEEE AP-S Intl. Symposium*, Spokane, WA, Jul. 3–8, 2011.

[50] S. Wang, A. P. Feresidis, G. Goussetis and J. C. Vardaxoglou, "Low profile resonant cavity antenna with artificial magnetic conductor ground plane," *Electronics Letters,* vol. 40, pp. 405–506, Apr. 1, 2004.

[51] S. Wang, A. P. Feresidis, G. Goussetis and J. C. Vardaxoglou, "Artificial magnetic conductors for low-profile resonant cavity antennas," *IEEE AP-S Intl. Symposium*, Monterey, CA, USA, vol. 2, pp. 1423–1426, Jun. 20–25, 2004.

[52] A. P. Feresidis, G. Goussetis, S. Wang and Vardaxoglou, "Artificial magnetic conductor surfaces and their application to low-profile high-

gain planar antennas," *IEEE Trans. Antennas Propag.,* vol. 53, no. 1, pp. 209–215, Jan. 2005.

[53] S. N. Burokur, R. Yahiaoui and A. de Lustrac, "Subwavelength resonant cavities fed by microstrip patch array," *IEEE Intl. Workshop on Antenna Technology,* Santa Monica, CA, USA, pp. 1–4, Mar. 2–4, 2009.

[54] L. Zhou, H. Li, Y. Qin, Z. Wei and C. T. Chan, "Directive emissions from subwavelength metamaterial-based cavities," *IEEE Intl. Workshop on Antenna Technology,* pp. 191–194, Mar. 7–9, 2005.

[55] A. Ourir, A. de Lustrac and J.-M. Lourtioz, "All-metamaterial-based subwavelength cavities (λ/60) for ultrathin directive antennas," *Applied Physics Letters,* vol. 88, Feb. 2006.

[56] S. Wang, A. P. Feresidis, G. Goussetis and J. C. Vardaxoglou, "High gain subwavelength resonant cavity antennas based on metamaterial ground planes," *IEEE Proc. Microwaves, Antennas, and Propagation,* vol. 53, no. 1, pp. 1–6, Feb. 2006.

[57] J. R. Kelly and A. P. Feresidis, "Low-profile high gain sub-wavelength resonant cavity antennas for wimax applications," *European Conf. on Antennas and Propagation (EuCAP)*, Edinburgh, Scotland, U.K., Nov. 11–16, 2007.

[58] R. Yahiaoui, S. N. Burokur and A. d. Lustrac, "Enhanced directivity of ultra-thin metamaterial-based cavity antenna fed by multisource," *Electronics Letters,* vol. 45, no. 16, pp. 814–816, Jul. 2009.

[59] Z. -G. Liu and R. Qiang, "Comparative approach of Fabry-Pérot resonator antenna with PMC and PEC ground plane," *IEEE AP-S Intl. Symposium*, Toronto, Ontario, Canada, Jul. 11–17, 2010.

[60] C. Mateo-Segura, G. Goussetis and A. P. Feresidis, "Sub-wavelength profile 2-D leaky-wave antennas with two periodic layers," *IEEE Trans. Antennas Propag.,* vol. 59, no. 2, pp. 416–424, Feb. 2011.

[61] J. Ju, D. Kim, W. Lee and J. Choi, "Low-profile Fabry-Pérot cavity antenna with a double-layered partially reflecting surface structure," *Mi-*

crowave and Optical Technology Letters, vol. 53, no. 2, pp. 271–273, Feb. 2011.

[62] Y. Liu and X. Zhao, "High-gain ultrathin resonant cavity antenna," *Microwave and Optical Technology Letters,* vol. 53, no. 9, pp. 1945–1949, Sep. 2011.

[63] A. Pirhadi, M. Hakkak, F. Keshmiri and R. K. Baee, "Design of compact dual band high directive electromagnetic bandgap (EBG) resonator antenna using artificial magnetic conductor," *IEEE Trans. Antennas Propagat.,* vol. 55, no. 6, pp. 1682– 1690, Jun. 2007.

[64] Z.-G. Liu and T. -H. Liu, "Comparative study of Fabry-Pérot resonator antenna with PMC and PEC ground plane," *J. Progress in Electromagnetics Research B,* vol. 32, pp. 299–317, 2011.

[65] F. Costa and A. Monorchio, "Design of subwavelength tunable and steerable Fabry-Pérot/leaky wave antennas," *J. Progress in Electromagnetics Research,* vol. 111, pp. 467–481, 2011.

[66] G. Lovat, P. Burghignoli and D. R. Jackson, "An investigation of directive radiation from ultra subwavelength-thick planar antennas with partially-reflecting surfaces," *IEEE AP-S Intl. Symp.*, San Diego, CA, Jul. 5–12, 2008.

[67] A. Chlavin, "A New Antenna Feed Having Equal E- and H- Plane Patterns," vol. 93, 1954.

[68] H. Wong, K.-M. Mak, and K.-M. Luk, "Wideband Shorted Bowtie Patch Antenna With Electric Dipole," *IEEE Trans. Antennas Propag.*, vol. 56, no. 7, pp. 2098–2101, 2008.

[69] L. Ge and K. M. Luk, "A Low-Profile Magneto-Electric Dipole Antenna," *IEEE Trans. Antennas Propagations*, vol. 60, no. 4, pp. 1684–1689, 2012.

[70] K. Luk and H. Wong, "A New Wideband Unidirectional Antenna Element," *Int. J. Microw. Opt. Technol.*, no. 1, pp. 35–44, 2006.

[71] L. E. I. Ge and K. M. A. N. Luk, "Beamwidth Reconfigurable MagnetoElectric Dipole Antenna Based on Tunable Strip Grating Reflector," *IEEE Access*, vol. 4, pp. 7039–7045, 2016.

[72] K. He, S. Gong, and F. Gao, "A Wideband Dual-Band Magneto-Electric Dipole," *IEEE Antennas Wirel. Propag. Lett.*, vol. 13, pp. 1729–1732, 2015.

[73] W. X. An, H. Wong, K. L. Lau, S. F. Li, and Q. Xue, "Design of Broadband Dual-Band Dipole for Base Station Antenna," *IEEE Trans. Antennas Propagations*, vol. 60, no. 3, pp. 1592–1595, 2012.

[74] S. Yan, P. J. Soh, and G. A. E. Vandenbosch, "Wearable Dual-Band Magneto-Electric Dipole Antenna for WBAN / WLAN Applications," *IEEE Trans. Antennas Propag.*, vol. 63, no. 9, pp. 4165–4169, 2015.

[75] B. Q. Wu and K. Luk, "A Broadband Dual-Polarized Magneto-Electric Dipole Antenna With Simple Feeds," *IEEE Antennas Wirel. Propag. Lett.*, vol. 8, pp. 60–63, 2009.

[76] Q. Xue, S. W. Liao, and J. H. Xu, "A Differentially-Driven Dual-Polarized Magneto-Electric Dipole Antenna," *IEEE Trans. Antennas Propag.*, vol. 61, no. 1, pp. 425–430, 2013.

[77] Y. Gou, S. Yang, J. Li, and Z. Nie, "A Compact Dual-Polarized Printed Dipole Antenna With High Isolation for Wideband Base Station Applications," *IEEE Trans. Antennas Propag.*, vol. 62, no. 8, pp. 4392–4395, 2014.

[78] A. O. Li and K. Luk, "A Dual Linearly Polarized End-Fire Antenna Array for the 5G Applications," *IEEE Access*, vol. 6, pp. 78276–78285, 2018.

[79] S. J. Yang, Y. M. Pan, S. Member, Y. Zhang, and S. Member, "Low-Profile Dual-Polarized Filtering Magneto-Electric Dipole Antenna for 5G Applications," *IEEE Trans. Antennas Propag.*, vol. 67, no. 10, pp. 6235–6243, 2019.

[80] Y. Li and K. Luk, "A 60-GHz Wideband Circularly Polarized Aperture Coupled Magneto-Electric Dipole Antenna Array," *IEEE Trans. Antennas Propag.*, vol. 64, no. 4, pp. 1325–1333, 2016.

[81] S. X. Ta and I. Park, "Crossed Dipole Loaded With Magneto-Electric Dipole for Wideband and Wide-Beam Circularly Polarized Radiation," *IEEE Antennas Wirel. Propag. Lett.*, vol. 14, pp. 358–361, 2015.

[82] J. Cao, H. Wang, S. Mou, S. Quan, Z. Ye, and A. Abstract, "W-Band High Gain Circularly Polarized Aperture-Coupled Magneto-Electric Dipole Antenna Array With Gap Waveguide Feed Network," *IEEE Antennas Wirel. Propag. Lett.*, vol. 16, pp. 2155–2158, 2017.

[83] M. Li and K. -M. Luk, "A wideband dual-fed circularly polarized antenna," *2013 IEEE International Workshop on Electromagnetics, Applications and Student Innovation Competition*, Hong Kong, China, 2013, pp. 112-114.

[84] L. Ge and K. M. Luk, "A Magneto-Electric Dipole Antenna With Low-Profile and Simple Structure," *IEEE Antennas Wirel. Propag. Lett.*, vol. 12,pp. 140–142, 2013.

[85] K. B. Ng, H. Wong, K. K. So, C. H. Chan, and K. M. Luk, "60 GHz Plated Through Hole Printed Magneto-Electric Dipole Antenna," *IEEE Trans. Antennas Propag.*, vol. 60, no. 7, pp. 3129–3136, 2012.

[86] A. N. Ince, Digital Satellite Communications Systems and Technologies: Military and Civil Applications, Springer, 2012.

[87] D. Brunnenmeyer et al., "Ka and Ku operational considerations for military SATCOM applications," *MILCOM 2012–2012 IEEE Military Communications Conference*, pp. 1–7, 2012.

[88] H. Lueschow and R. Pelaez, "Satellite communication for security and defense," *Handbook of Space Security: Policies, Applications and Programs*, Springer, pp. 779–796, 2020.

[89] Q. Luo and S. Gao, "Smart antennas for satellite communications on the move," *2017 Intern. Workshop on Antenna Technology (iWAT)*, pp. 260–263, 2017.

[90] S. Vaccaro et al., "Ku-Band Low Profile Antennas for Mobile Satcom," in *4th Adv. Sat. Mob. Syst*., pp. 24–28, 2008.

[91] R. J. Bolt et al., "Characterization of a Dual-Polarized Connected-Dipole Array for Ku-Band Mobile Terminals," *IEEE Trans. Antennas Propag.*, vol. 64, no. 2, pp. 591–598, 2016.

[92] A. H. Aljuhani et al., "A Scalable Dual-Polarized 256-Element Ku-Band Phased-Array SATCOM Receiver with ±70◦ Beam Scanning," *IEEE/MTT-S Intern. Microw. Symp. (IMS)*, pp. 1203–1206, 2018.

[93] K. Y. Kapusuz et al., "Low-profile scalable phased array antenna at Ku-band for mobile satellite communications," *IEEE Intern. Symp. Phased Array Syst. Tech. (PAST)*, pp. 1–4, 2016.

[94] M. H. Awida and A. E. Fathy, "Substrate-Integrated Waveguide Ku-Band Cavity Backed 2×2 Microstrip Patch Array Antenna," *IEEE Antennas Wireless Propag. Lett*., vol. 8, pp. 1054–1056, 2009.

[95] D. Guarnera et al., "Design of a Corporate Feed Cavity Backed Linear Slot Array in Waveguide Technology," *2023 IEEE Conf. Antenna Measurements and Applications (CAMA)*, pp. 334–336, 2023.

[96] W. Yuan et al., "Rectangular Grating Waveguide Slot Array Antenna for SATCOM Applications," *IEEE Trans. Antennas Propag*., vol. 67, no. 6, pp. 3869–3880, 2019.

[97] M. Mirmozafari, G. Zhang, S. Saeedi, and R. J. Doviak, "A dual linear polarization highly isolated crossed dipole antenna for MPAR application," *IEEE Antennas Wireless Propag. Lett*., vol. 16, pp. 1879–1882, 2017.

[98] S. C. Pavone, G. S. Mauro, L. Di Donato, and G. Sorbello, "Design of Dual Circularly Polarized Sequentially-Fed Patch Antennas for Satellite Applications," *Appl. Sci*., vol. 10, no. 6, 2020.

[99] S. C. Pavone, M. Casaletti, and M. Albani, "Automatic design of a CP Fan-beam Linear Slotted Array in SIW Technology," *IEEE Access*, vol. 7, pp. 155977–155985, 2019.

[100] O. Leonardi, M. G. Pavone, G. Sorbello, A. F. Morabito, and T. Isernia, "Compact single-layer circularly polarized antenna for short-range communication systems," *Microw. Opt. Technol. Lett.*, vol. 56, no. 8, pp. 1843–1846, 2014.

[101] H. Kaouach, L. Dussopt, J. Lanteri, T. Koleck, and R. Sauleau, "Wideband low-loss linear and circular polarization transmit-arrays in V-band", *IEEE Transactions on Antennas and Propagation*, vol. 59, 7, pp. 2513–2523, 2011.

[102] F. Foglia Manzillo, A. Clemente, and J. L. González-Jiménez, "High-gain D-band transmitarrays in standard PCB technology for beyond-5G communications", *IEEE Transactions on Antennas and Propagation*, vol. 68, 1, pp. 587–592, 2020.

[103] K. Medrar, L. Marnat, L. Dussopt, et al., "H-band substrate-integrated discrete lens antenna for high data rate communication systems", *IEEE Transactions on Antennas and Propagation*, vol. 69, 7, pp. 3677–3688, 2021.

[104] A. Clemente, L. Dussopt, R. Sauleau, P. Potier, and P. Pouliguen, "Wideband 400- element electronically reconfigurable transmitarray in X band", *IEEE Transactions on Antennas and Propagation*, vol. 61, 10, pp. 5017–5027, 2013.

[105] A. Clemente, "*Design of transmitarrays with beamforming/beamtilting capability*" PhD dissertation, University of Rennes, France, 2012.

[106] Orestis Koutsos, "*Study, modeling and design of fixed beam transmitarray antennas at 300 GHz*", PhD dissertation, Electronics, University of Rennes, France, 2022.

[107] S. Datthanasombat, L. R. Amaro, J. A. Harrell, S. Spitz and J. Perret, "Layered lens antenna", *IEEE Antennas and Propagation Society International Symposium*, pp. 777–780, Boston, 2001.

[108] D. M. Pozar, *Microwave Engineering*, 3rd ed., John Wiley & Sons, Inc., New York, 2005.

[109] B. A. Munk, *Frequency Selective Surfaces, Theory and Design*, John Wiley & Sons, Inc., NY,2000.

[110] Pablo Mateos-Ruiz, Alberto Hernandez-Escobar, Elena Abdo-S´anchez, Carlos Camacho-Pe´nalosa, "Design and Fabrication of a Fabry-Pérot Cavity Antenna for the Ku-band", *XXXV National Symposium of the International Union of Radio Science, URSI 2020*, Spain, September 2-4, 2020.

[111] O. Luukkonen *et al*., "Simple and Accurate Analytical Model of Planar Grids and High-Impedance Surfaces Comprising Metal Strips or Patches," in *IEEE Transactions on Antennas and Propagation*, vol. 56, no. 6, pp. 1624-1632, June 2008.

[112] Mahajan, R.C., Vyas, V., "Verification, enhancement and mathematical analysis of EBG structure using complex geometrical shapes and eigenmode analysis approach," *SN Appl. Sci.*, vol. 2, article no. 30, 2020.

[113] 1. Alhalabi, R.A.; Rebeiz, G.M., "High-efficiency angled-dipole antennas for millimeter-wave phased array applications," *IEEE Trans. Antennas Propag.*, vol. 56, pp. 3136–3142, 2008.

[114] Zhang, H.Y.; Zhang, F.S.; Zhang, F.; Sun, F.K.; Xie, G.J., "High-power array antenna based on phase-adjustable array element for wireless power transmission," *IEEE Antennas Wirel. Propag. Lett.*, vol. 16, pp. 2249–2253, 2017.

[115] Zhang, S.; Chen, X.; Syrytsin, I.; Pedersen, G.F, "A planar switchable 3-D-coverage phased array antenna and its user effects for 28-GHz mobile terminal applications," *IEEE Trans. Antennas Propag.*, vol. 65, pp. 6413–6421, 2017.

[116] Han, G.; Du, B.; Wu, W.; Yang, B., "A novel hybrid phased array antenna for satellite communication on-the-move in Ku-band," *IEEE Trans. Antennas Propag.*, vol. 63, pp. 1375–1383, 2015.

[117] Wang, Z.; Zhang, G.X.; Yin, Y.; Wu, J., "Design of a dual-band high-gain antenna array for WLAN and WiMAX base station," *IEEE Antennas Wirel. Propag. Lett.*, vol. 13, pp. 1721–1724, 2014.

[118] Alotaibi, N.N.; Hamdi, K.A., "Switched phased-array transmission architecture for secure millimeter-wave wireless communication," *IEEE Trans. Commun.*, vol. 64, pp. 1303–1312, 2016.

[119] Hwang, S.; Lee, B.; Kim, D.H.; Park, J.Y., "Design of S-band phased array antenna with high isolation using broadside coupled split ring resonator," *J. Electromagn. Eng. Sci.*, vol. 18, pp. 108–116, 2018.

[120] Xu, H.X.; Cai, T.; Zhuang, Y.Q.; Peng, Q.; Wang, G.; Liang, J.G., "Dual-mode transmissive metasurface and its applications in multibeam transmitarray," *IEEE Trans. Antennas Propag.*, vol. 65, pp. 1797–1806, 2017.

[121] Diaby, F.; Clemente, A.; Sauleau, R.; Pham, K.T.; Dussopt, L., "2-bit reconfigurable unit-cell and electronically steerable transmitarray at Ka-band," *IEEE Trans. Antennas Propag.*, vol. 68, pp. 5003–5008, 2020.

[122] Wang, Y.; Xu, S.; Yang, F.; Li, M., "A novel 1-bit wide-angle beam scanning reconfigurable transmitarray antenna using an equivalent magnetic dipole element," *IEEE Trans. Antennas Propag.*, vol. 68, pp. 5691–5695, 2020.

[123] Zeng, Q.; Xue, Z.; Ren, W.; Li, W., "Dual-band beam-scanning antenna using rotatable planar phase gradient transmitarrays," *IEEE Trans. Antennas Propag.*, vol. 68, pp. 5021–5026, 2020.

[124] Liang, Z.; Ouyang, J.; Yang, F., "Low-profile wideband circularly polarised single-layer metasurface antenna," *Electron. Lett.*, vol. 54, pp. 1362–1364, 2018.

[125] Abdelrahman, A.H.; Nayeri, P.; Elsherbeni, A.Z.; Yang, F., "Single-feed quad-beam transmitarray antenna design," *IEEE Trans. Antennas Propag.*, vol. 64, pp. 953–959, 2016.

[126] Zheng, B.; Fan, Y.; Cheng, Y.J., "Wideband high-efficiency circularly polarized transmitarray with linearly polarized feed," *IEEE Antennas Wirel. Propag. Lett.*, vol. 22, pp. 1451–1455, 2023.

[127] Abdelrahman, A.H.; Yang, F.; Elsherbeni, A.Z.; Nayeri, P.; Balanis, C.A. *Analysis and Design of Transmitarray Antennas*; Springer: Cham, Switzerland, 2017.

[128] Ramazannia Tuloti, S.H.; Rezaei, P.; Tavakkol Hamedani, F., "High-efficient wideband transmitarray antenna," *IEEE Antennas Wirel. Propag. Lett.*, vol. 17, pp. 817–820, 2018.

[129] Watts, C.M.; Pedross-Engel, A.; Smith, D.R.; Reynolds, M.S., "X-band SAR imaging with a liquid-crystal-based dynamic metasurface antenna," *J. Opt. Soc. Am. B Opt. Phys.*, vol. 34, pp. 300–306, 2017.

[130] Arbabi, E.; Arbabi, A.; Kamali, S.M.; Horie, Y.; Faraji-Dana, M.; Faraon, A., "MEMS-tunable dielectric metasurface lens," *Nat. Commun.*, vol. 9, 812, 2018.

[131] Sleasman, T.; Imani, M.F.; Xu, W.; Hunt, J.; Driscoll, T.; Reynolds, M.S.; Smith, D.R., "Waveguide-fed tunable metamaterial element for dynamic apertures," *IEEE Antennas Wirel. Propag. Lett.*, vol. 15, pp. 606–609, 2016.

[132] Xu, H.-X.; Tang, S.; Ma, S.; Luo, W.; Cai, T.; Sun, S.; He, Q.; Zhou, L., "Tunable microwave metasurfaces for high-performance operations: Dispersion compensation and dynamical switch," *Sci. Rep.*, vol. 6, 38255, 2016.

[133] Massaccesi, A.; Dassano, G.; Pirinoli, P., "Beam scanning capabilities of a 3D-printed perforated dielectric transmitarray," *Electronics*, vol. 8, 379, 2019.

[134] Ali, Q.; Shahzad, W.; Ahmad, I.; Safiq, S.; Bin, X.; Abbas, S.M.; Sun, H., "Recent developments and challenges on beam steering characteristics of reconfigurable transmitarray antennas," *Electronics*, vol. 11, 587, 2022.

[135] Lee, J.-G.; Kwon, T.-S.; Lee, J.-H., "Beam pattern reconfigurable circularly polarized transmitarray antenna by rearrangement of sources," *Microw. Opt. Technol. Lett.*, vol. 61, pp. 999–1003, 2019.

[136] Lee, C.; Hoang, T.V.; Wook, S.; Lee, S.; Lee, J., "Low-profile quad-beam circularly polarised antenna using transmissive metasurface," *IET Microw. Antennas Propag.*, vol. 13, pp. 1690–1698, 2019.

[137] Mei, P.; Zhang, S.; Pedersen, G.F., "A low-profile and beam-steerable transmitarray antenna: Design, fabrication, and measurement [Antenna Applications Corner]," *IEEE Antennas Propag. Mag.*, vol. 63, pp. 88–101, 2021.

[138] De Marco, R.; Arnieri, E.; Greco, F.; Bordbar, A.; Amendola, G.; Boccia, L., "Low-profile dual-band dual-polarized transmitarray antenna based on multilayer frequency selective surfaces," *IEEE Trans. Antennas Propag.*, vol. 71, pp. 7354–7362, 2023.

[139] Jiao, X.-H.; Wan, G., "A novel low-profile planar microstrip transmitarray antenna with high efficiency," *Int. J. RF Microw. Comput.-Aided Eng.*, vol. 31, e22614, 2021.

[140] Park, J.-H.; Lee, J.-G., "Low-profile high-efficiency transmitarray antenna using optimized phase compensation surface (PCS) and PEC sidewalls," *ICT Express*, vol. 7, pp. 501–506, 2021.

[141] Frank, M.; Lurz, F.; Weigel, R.; Koelpin, A., "Low-profile and low-cost transmitarray antenna at 122 GHz based on unit-cells with 1-bit phase resolution," *Electron. Lett.*, vol. 56, pp. 1293–1295, 2020.

[142] Wang, X.; Cheng, Y.; Dong, Y., "Millimeter-wave high-efficiency double-layer transmitarray antenna using miniaturized dualpolarized elements," *IEEE Trans. Antennas Propag.*, vol. 70, pp. 8637–8642, 2022.

[143] Li, T.; Sun, J.; Meng, H.; Shen, Y.; Hu, S.; Dou, W.; Chen, Z.N.; Zwick, T., "Characteristic mode inspired dual-polarized double-layer metasurface lens," *IEEE Trans. Antennas Propag.*, vol. 69, pp. 3144–3154, 2021.

[144] Xue, C.; Sun, J.; Niu, L.; Lou, Q., "Ultrathin dual-polarized Huygens' metasurface: Design and application," *Ann. Phys.*, vol. 532, 2000151, 2020.

[145] Yang, S.; Yan, Z.; Cai, M.; Fan, F.; Zhang, T., "A high-efficiency double-layer transmitarray antenna using low-loss dual-linearly polarized elements," *IEEE Antennas Wirel. Propag. Lett.*, vol. 19, pp. 2378–2382, 2020.

[146] Yi, X.; Su, T.; Li, X.; Wu, B.; Yang, L., "A double-layer wideband transmitarray antenna using two degrees of freedom elements around 20 GHz," *IEEE Trans. Antennas Propag.*, vol. 67, pp. 2798–2802, 2019.

[147] Pham, K.; Nguyen, N.T.; Clemente, A.; Di Palma, L.; Le Coq, L.; Dussopt, L.; Sauleau, R., "Design of wideband dual linearly polarized transmitarray antennas," *IEEE Trans. Antennas Propag.*, vol. 64, pp. 2022–2026, 2016.

[148] Aziz, A.; Yang, F.; Xu, S.; Li, M., "An efficient dual-band orthogonally polarized transmitarray design using three-dipole elements," *IEEE Antennas Wirel. Propag. Lett.*, vol. 17, pp. 319–322, 2018.

[149] Bagheri, M.O.; Hassani, H.R.; Rahmati, B., "Dual-band, dual-polarised metallic slot transmitarray antenna," *IET Microw. Antennas Propag.*, vol. 11, pp. 402–409, 2017.

[150] Aziz, A.; Yang, F.; Xu, S.; Li, M.; Chen, H.-T., "A high-gain dual-band and dual-polarized transmitarray using novel loop elements," *IEEE Antennas Wirel. Propag. Lett.*, vol. 18, pp. 1213–1217, 2019.

[151] Wu, F.; Wang, J.; Xiang, L.; Hong, W.; Luk, K.-M., "A wideband dual-polarized magneto-electric dipole transmitarray with independent control of polarizations," *IEEE Trans. Antennas Propag.*, vol. 70, pp. 8632–8636,2022.

[152] Pham, K.T.; Sauleau, R.; Fourn, E.; Diaby, F.; Clemente, A.; Dussopt, L., "Dual-band transmitarrays with dual-linear polarization at Ka-band," *IEEE Trans. Antennas Propag.*, vol. 65, pp. 7009–7018, 2017.

[153] Pan, W.; Huang, C.; Ma, X.; Jiang, B.; Luo, X., "A dual linearly polarized transmitarray element with 1-bit phase resolution in X-band," *IEEE Antennas Wirel. Propag. Lett.*, vol. 14, pp. 167–170, 2015.

[154] Saleh, W.; Letestu, Y.; Sauleau, R.; Cruz, E.M., "Design and measurements of a high-performance wideband transmitarray antenna for D-band communications," *IEEE Antennas Wirel. Propag. Lett.*, vol. 20, pp. 1765–1769, 2021.

[155] Wang, Y.; Xu, S.; Yang, F.; Werner, D.H., "1-bit dual-linear polarized reconfigurable transmitarray antenna using asymmetric dipole elements with parasitic bypass dipoles," *IEEE Trans. Antennas Propag.*, vol. 69, pp. 1188–1192, 2021.

[156] Khan MI, Loconsole AM, Anelli F, Francione VV, Khan AU, Simone M, Sorbello G, Prudenzano F., "A Low-Profile Dual-Polarized Transmitarray with Enhanced Gain and Beam Steering at Ku Band," *Applied Sciences*, vol. 15, 4656, 2025.

[157] Zhang, S.; Cao, W.; Wu, T.; Wang, J.; Wei, Y., "The Design of a Multifunctional Coding Transmitarray with Independent Manipulation of the Polarization States," *Micromachines*, vol. 15, 1014, 2024.

[158] Li, Z.; Weng, X.; Yi, X.; Li, K.; Duan, W.; Bi, M., "Design and analysis of a complementary structure-based high selectivity tri-band frequency selective surface," *Sci. Rep.*, vol. 14, 9415, 2024.

[159] Losito, O.; Portosi, V.; Venanzoni, G.; Bigelli, F.; Mencarelli, D.; Scalmati, P.; Renghini, C.; Carta, P.; Prudenzano, F., "Feasibility investigation of SIW cavity-backed patch antenna array for Ku-band applications," *Appl. Sci.*, vol. 9, 1271, 2019.

[160] Huang, G.-L.; Pang, Z.-Y.; Al-Nuaimi, M.K.T.; Kishk, A.A.; Mahmoud, A., "A Broadband and High-Aperture-Efficiency Multilayer Transmitarray Based on Aperture-Coupled Slot Unit Cells.," *IEEE Trans. Antennas Propag.*, vol. 71, pp. 9633–9642, 2023.

[161] Fan, Y.-L.; Lin, X.-Q.; Liu, S.-L., "A broadband bifocal conformal transmitarray antenna with wide scanning angles," *Microw. Opt. Technol. Lett.*, vol. 64, pp. 1800–1808, 2022.

[162] Jiang, M.; Chen, Z.N.; Zhang, Y.; Hong, W.; Xuan, X., "Metamaterial-based thin planar lens antenna for spatial beamforming and multibeam massive MIMO," *IEEE Trans. Antennas Propag.*, vol. 65, pp. 464–472,2017.

[163] Zhang, F.; Yang, G.-M.; Jin, Y.-Q., "Low-Profile Circularly Polarized Transmitarray for Wide-Angle Beam Control With a Third-Order Meta-FSS," *IEEE Trans. Antennas Propag.*, vol. *68*, pp. 3586–3597,2020.

[164] Niroo Jazi, M.; Chaharmir, M.R.; Shaker, J.; Sebak, A.R., "Broadband transmitarray antenna design using polarization-insensitive frequency selective surfaces," *IEEE Trans. Antennas Propag.* vol. 64, pp. 99–108, 2016.

[165] Li, M.-Y.; Ban, Y.-L.; Yan, F.-Q., "Wideband low-profile Ku-band transmitarray antenna," *IEEE Access,* vol. 9, pp. 6683–6688, 2021.

[166] Li, G.; Ge, Y.; Chen, Z. A compact multibeam folded transmitarray antenna at Ku-band. *IEEE Antennas Wirel. Propag. Lett.*, vol. 20, pp. 808–812, 2021.

[167] A. T. Castro and S. K. Sharma, "Inkjet-Printed Wideband Circularly Polarized Microstrip Patch Array Antenna on a PET Film Flexible Substrate Material," IEEE Antennas Wirel. Propag. Lett., vol. 17, no. 1, pp. 176–179, Jan. 2018.

[168] B. S. Cook and A. Shamim, "Inkjet Printing of Novel Wideband and High Gain Antennas on Low-Cost Paper Substrate," IEEE Trans. Antennas Propag., vol. 60, no. 9, pp. 4148–4156, Sep. 2012.

[169] B. S. Cook, B. Tehrani, J. R. Cooper, and M. M. Tentzeris, "Multilayer Inkjet Printing of Millimeter-Wave Proximity-Fed Patch Arrays on Flexible Substrates," IEEE Antennas Wirel. Propag. Lett., vol. 12, pp. 1351–1354, 2013.

[170] H. Saghlatoon, L. Sydanheimo, L. Ukkonen, and M. Tentzeris, “Optimization of Inkjet Printing of Patch Antennas on Low-Cost Fibrous Substrates,” IEEE Antennas Wirel. Propag. Lett., vol. 13, pp. 915–918, 2014.

[171] Y. Ge, K. P. Esselle, and T. S. Bird, “The Use of Simple Thin Partially Reflective Surfaces With Positive Reflection Phase Gradients to Design Wideband, Low-Profile EBG Resonator Antennas,” IEEE Trans. Antennas Propag., vol. 60, no. 2, pp. 743–750, Feb. 2012.

[172] R. M. Hashmi, B. A. Zeb, and K. P. Esselle, “Wideband High-Gain EBG Resonator Antennas With Small Footprints and All-Dielectric Superstructures,” IEEE Trans. Antennas Propag., vol. 62, no. 6, pp. 2970–2977, Jun. 2014.

[173] K. Konstantinidis, A. P. Feresidis, and P. S. Hall, “Multilayer Partially Reflective Surfaces for Broadband Fabry-Perot Cavity Antennas,” IEEE Trans. Antennas Propag., vol. 62, no. 7, pp. 3474–3481, Jul. 2014.

[174] B. A. Zeb, N. Nikolic, and K. P. Esselle, “A High-Gain Dual-Band EBG Resonator Antenna with Circular Polarization,” IEEE Antennas Wirel. Propag. Lett., vol. 14, pp. 108–111, 2015.

[175] M. A. Al-Tarifi, D. E. Anagnostou, A. K. Amert, and K. W. Whites, “Bandwidth Enhancement of the Resonant Cavity Antenna by Using Two Dielectric Superstrates,” IEEE Trans. Antennas Propag., vol. 61, no. 4, pp. 1898–1908, Apr. 2013.

[176] A. R. Weily, L. Horvath, K. P. Esselle, B. C. Sanders, and T. S. Bird, “A planar resonator antenna based on a woodpile EBG material,” IEEE Trans. Antennas Propag., vol. 53, no. 1, pp. 216–223, Jan. 2005.

[177] M. W. Niaz, Y. Yin, R. A. Bhatti, Y.-M. Cai, and J. Chen, “Wideband Fabry–Perot Resonator Antenna Employing Multilayer Partially Reflective Surface,” IEEE Trans. Antennas Propag., vol. 69, no. 4, pp. 2404–2409, Apr. 2021.

[178] F. Anelli, A. M. Loconsole, V. V. Francione, M. I. Khan and F. Prudenzano, "Cost-Effective Fabry–Pérot Antenna via Conductive Inkjet and

Additive Printing," in *IEEE Antennas and Wireless Propagation Letters*, vol. 24, no. 8, pp. 2182-2186, Aug. 2025.

[179] N. Wang, Q. Liu, C. Wu, L. Talbi, Q. Zeng and J. Xu, "Wideband Fabry-Perot Resonator Antenna With Two Complementary FSS Layers," IEEE Trans. Antennas Propag., vol. 62, no. 5, pp. 2463–2471, May 2014.

[180] Y. Pan, J. Dong, and M. Wang, "Equivalent Circuit-Assisted Multi-Objective Particle Swarm Optimization for Accelerated Reverse Design of Multi-Layer Frequency Selective Surface," Nanomaterials, vol. 12, no. 21, p. 3846, Oct. 2022.

[181] N. Wang, J. Li, G. Wei, L. Talbi, Q. Zeng, and J. Xu, "Wideband Fabry–Perot Resonator Antenna With Two Layers of Dielectric Superstrates," IEEE Antennas Wirel. Propag. Lett., vol. 14, pp. 229–232, 2015.

[182] G. Gonçalves Machado, R. Cahill, V. Fusco, and G. Conway, "Frequency selective superstrate absorber for wideband RCS reduction of metal-backed antennas," IET Microw. Antennas Propag., vol. 15, no. 4, pp. 441–450, Mar. 2021.

[183] M. M. Taskhiri and S. Fakhte, "Broadband inhomogeneous lens with conical radiation pattern," Sci. Rep., vol. 13, no. 1, p. 12907, Aug. 2023.

[184] J. A. Ansari, S. K. Dubey, P. Singh, R. U. Khan, and B. R. Vishvakarma, "Analysis of V-slot loaded patch for wide-band operation," Microw. Opt. Technol. Lett., vol. 50, no. 12, pp. 3069–3075, Dec. 2008.

[185] K. Konstantinidis, A. P. Feresidis, and P. S. Hall, "Broadband Sub-Wavelength Profile High-Gain Antennas Based on Multi-Layer Metasurfaces," IEEE Trans. Antennas Propag., vol. 63, no. 1, pp. 423–427, Jan. 2015.

[186] F. Meng and S. K. Sharma, "A Wideband Resonant Cavity Antenna With Compact Partially Reflective Surface," IEEE Trans. Antennas Propag., vol. 68, no. 2, pp. 1155–1160, Feb. 2020.

[187] H. Attia, M. L. Abdelghani, and T. A. Denidni, "Wideband and High-Gain Millimeter-Wave Antenna Based on FSS Fabry–Perot Cavity,"

IEEE Trans. Antennas Propag., vol. 65, no. 10, pp. 5589–5594, Oct. 2017.

[188] S. F. Jilani, M. O. Munoz, Q. H. Abbasi, and A. Alomainy, "Millimeter-Wave Liquid Crystal Polymer Based Conformal Antenna Array for 5G Applications," IEEE Antennas Wirel. Propag. Lett., vol. 18, no. 1, pp. 84–88, Jan. 2019.

[189] W. Peng, J. Yu, H. Zhang, X. Wang, C. Zhang, and H. Xiao, "High-Bandwidth Flexible Inkjet-Printed Antenna Design for Microwave Power Transfer Applications," IEEE Electron Device Lett., vol. 45, no. 7, pp. 1377–1380, Jul. 2024.

[190] (Nov. 2018). *Ericsson Mobility Report.* [Online]. Available: https://www.ericsson.com/4ac644/assets/local/reports-papers/mobility report/documents/2018/ericsson-mobility-report-november-2018.pdf

[191] S. Uk Oh, H. Yoo and T. H. Jang, "A Low-Profile Millimeter-Wave Broadband Magneto Electric Dipole Antenna With Fragmented Dipole Arm," in *IEEE Transactions on Antennas and Propagation*, vol. 73, no. 2, pp. 1203-1208, Feb. 2025.

[192] L. Wang, Y.-X. Guo, and W.-X. Sheng, "Wideband high-gain 60-GHz LTCC L-probe patch antenna array with a soft surface," *IEEE Trans. Antennas Propag.*, vol. 61, no. 4, pp. 1802–1809, Apr. 2013.

[193] H. Sun, Y.-X. Guo, and Z. Wang, "60-GHz circularly polarized U-slot patch antenna array on LTCC," *IEEE Trans. Antennas Propag.*, vol. 61,no. 1, pp. 430–435, Jan. 2013.

[194] Y. Li and K.-M. Luk, "Low-cost high-gain and broadband substrate integrated-waveguide-fed patch antenna array for 60-GHz band," *IEEE Trans. Antennas Propag.*, vol. 62, no. 11, pp. 5531–5538, Nov. 2014.

[195] Q. Zhu, K. B. Ng, C. H. Chan, and K.-M. Luk, "Substrate-integrated-waveguide-fed array antenna covering 57-71 GHz band for 5G applications," *IEEE Trans. Antennas Propag.*, vol. 65, no. 12, pp. 6298–6306, Dec. 2017.

[196] Y. Li *et al.*, “A Ka-band 3-D-printed wideband stepped waveguide-fed magneto-electric dipole antenna array,” *IEEE Trans. Antennas Propag.*, vol. 68, no. 4, pp. 2724–2735, Apr. 2020.

[197] J. Sun, A. Li and K. -M. Luk, "A High-Gain Millimeter-Wave Magnetoelectric Dipole Array With Packaged Microstrip Line Feed Network," in *IEEE Antennas and Wireless Propagation Letters*, vol. 19, no. 10, pp. 1669-1673, Oct. 2020.

[198] Y. Li, C. Wang, and Y. X. Guo, “A Ka-band wideband dual-polarized magneto-electric dipole antenna array on LTCC,” *IEEE Trans. Antennas Propag.*, vol. 68, no. 6, pp. 4985–4990, Jun. 2020.

[199] J. Cao, H. Wang, S. Mou, P. Soothar, and J. Zhou, “An air-cavity-fed circularly polarized magneto-electric dipole antenna array with gap waveguide technology for mm-wave applications,” *IEEE Trans. Antennas Propag.*, vol. 67, no. 9, pp. 6211–6216, Sep. 2019.

[200] D. Zarifi, A. Farahbakhah, A. U. Zaman, and P.-S. Kildal, “Design and fabrication of a high-gain 60-GHz corrugated slot antenna array with ridge gap waveguide distribution layer,” *IEEE Trans. Antennas Propag.*, vol. 64, no. 7, pp. 2905–2913, Jul. 2016.

[201] N. Ashraf, A. R. Sebak, and A. A. Kishk, “Packaged microstrip line feed network on a single surface for dual-polarized 2n × 2m ME-dipole antenna array,” *IEEE Antennas Wireless Propag. Lett.*, vol. 19, no. 4, pp. 596–600, Apr. 2020.

[202] M. I. Khan, F. Anelli, A. M. Loconsole, V. V. Francione and F. Prudenzano, "A Wideband Magneto-Electric Dipole Antenna with Electromagnetic Bandgap Structure",*2025 IEEE International Conference on Antennas and Applications*, Antibes, France, 2025.

[203] J. Kim, S. U. Oh and T. H. Jang, "Wide Beamwidth and Miniaturized Millimeter-Wave Endfire Angled ME Dipole Antenna With Extended Ground," in *IEEE Antennas and Wireless Propagation Letters*, vol. 23, no. 3, pp. 965-969, March 2024.

[204] S. X. Ta, H. Choo, and I. Park, "Broadband printed-dipole antenna and its arrays for 5G applications," *IEEE Antennas Wireless Propag. Lett.*, vol. 16, pp. 2183–2186, 2017.

[205] J. Zeng and K.-M. Luk, "Wideband millimeter-wave endfire magnetoelectric dipole antenna with microstrip-line feed," *IEEE Trans. Antennas Propag.*, vol. 68, no. 4, pp. 2658–2665, Apr. 2020.

[206] R. A. Alhalabi and G. M. Rebeiz, "High-efficiency angled-dipole antennas for millimeter-wave phased array applications," *IEEE Trans. Antennas Propag.*, vol. 56, no. 10, pp. 3136–3142, Oct. 2008.

[207] W. Hong, K. H. Baek, and S. Ko, "Millimeter-wave 5G antennas for smartphones: Overview and experimental demonstration," *IEEE Trans. Antennas Propag.*, vol. 65, no. 12, pp. 6250–6261, Dec. 2017.

[208] J.-C. S. Chieh, B. Pham, A.-V. Pham, G. Kannell, and A. Pidwerbetsky, "Millimeter-wave dual-polarized high-isolation antennas and arrays on organic substrates," *IEEE Trans. Antennas Propag.*, vol. 61, no. 12, pp. 5948–5957, Dec. 2013.

[209] T. Chaloun, V. Ziegler, and W. Menzel, "Design of a dual-polarized stacked patch antenna for wide-angle scanning reflectarrays," *IEEE Trans. Antennas Propag.*, vol. 64, no. 8, pp. 3380–3390, Aug. 2016.

[210] J. Lu et al., "Broadband dual-polarized waveguide slot filtenna array with low cross polarization and high efficiency," *IEEE Trans. Antennas Propag.*, vol. 67, no. 1, pp. 151–159, Jan. 2019.

[211] Q. Yang et al., "Differentially-fed dual-polarized 2D multibeam antenna array for millimeter-wave applications," in *Proc. Int. Conf. Microw. Millimeter Wave Technol.*, 2020, pp. 1–3.

[212] Y. J. Li and K. M. Luk, "60-GHz substrate integrated waveguide fed cavity-backed aperture-coupled microstrip patch antenna arrays," *IEEE Transactions on Antennas and Propagation*, vol. 63, no. 3, pp. 1075–1085, 2015.

[213] Z. Chen, H. Liu, J. Yu, and X. Chen, “High gain, broadband and dual polarized substrate integrated waveguide cavity-backed slot antenna array for 60 GHz band,” *IEEE Access*, vol. 6, pp. 31012–31022, 2018.

[214] F. F. Fan, Q. L. Chen, Y. X. Xu, *et al*., “A wideband compact printed dipole antenna array with SICL feeding network for 5G application,” *IEEE Antennas and Wireless Propagation Letters*, vol. 22, no. 2, pp. 283–287, 2023.

[215] L. Xiang *et al*., "Wideband Single and Dual Linearly Polarized Magneto-Electric Dipole Array Antennas for 5G/6G Millimeter-Wave Applications," in *IEEE Open Journal of Antennas and Propagation*, vol. 5, no. 2, pp. 525-539, April 2024.

[216] D. A. Pham, E. Park, H. L. Lee and S. Lim, "High Gain and Wideband Metasurfaced Magnetoelectric Antenna for WiGig Applications," in *IEEE Transactions on Antennas and Propagation*, vol. 69, no. 2, pp. 1140-1145, Feb. 2021.

[217] C.-Q. Feng, F.-S. Zhang, H.-J. Zhang, and J.-X. Su, "A single-feed circularly polarized magnetoelectric dipole antenna for wideband wireless applications," *Prog. Electromagn. Res. M*, vol. 65, pp. 1–8, 2018.

[218] X. Ruan, K. B. Ng and C. H. Chan, "A Differentially Fed Transmission-Line-Excited Magnetoelectric Dipole Antenna Array for 5G Applications," in *IEEE Transactions on Antennas and Propagation*, vol. 66, no. 10, pp. 5224-5230, Oct. 2018.

[219] X. Cui, F. Yang, M. Gao, L. Zhou, Z. Liang and F. Yan, "A Wideband Magnetoelectric Dipole Antenna With Microstrip Line Aperture-Coupled Excitation," in *IEEE Transactions on Antennas and Propagation*, vol. 65, no. 12, pp. 7350-7354, Dec. 2017.

[220] C. Ding and K. -M. Luk, "Low-Profile Magneto-Electric Dipole Antenna," IEEE Antennas Wirel. Propag. Lett., vol. 15, pp. 1642-1644, 2016.

[221] L. Siu, H. Wong and K. Luk, "A Dual-Polarized Magneto-Electric Dipole With Dielectric Loading," IEEE Trans. Antennas Propag., vol. 57, no. 3, pp. 616-623, March 2009.

[222] M. Li, Q. L. Li, B. Wang, C. F. Zhou and S. W. Cheung, "A Low-Profile Dual-Polarized Dipole Antenna Using Wideband AMC Reflector," IEEE Trans. Antennas Propag., vol. 66, no. 5, pp. 2610-2615, May 2018.

[223] H. Malekpoor and S. Jam, "Improved Radiation Performance of Low Profile Printed Slot Antenna Using Wideband Planar AMC Surface," IEEE Trans. Antennas Propag., vol. 64, no. 11, pp. 4626-4638, Nov. 2016.

[224] M. I. Khan, A. M. Loconsole, F. Anelli, V. V. Francione and F. Prudenzano, "A Wideband Magneto-Electric Dipole Based Slant Polarized Antenna with Metasurface",*2025 IEEE International Conference on Antennas and Applications*, Antibes, France, 2025.

[225] H. Y. Jin, W. Q. Che, K. S. Chin, *et al*., "Millimeter-wave TE_{20}-mode SIW dual-slot-fed patch antenna array with a compact differential feeding network," *IEEE Transactions on Antennas and Propagation*, vol. 66, no. 1, pp. 456–461, 2018.

[226] S. J. Yang, Y. M. Pan, L. Shi, and X. Y. Zhang, "Millimeter-wave dual polarized filtering antenna for 5G application," *IEEE Trans. Antennas Propag.*, vol. 68, no. 7, pp. 5114–5121, Jul. 2020.

[227] T. H. Jang, H. Y. Kim, D. M. Kang, S. H. Kim, and C. S. Park, "60 GHz low-profile, wideband dual-polarized U-slot coupled patch antenna with high isolation," *IEEE Trans. Antennas Propag.*, vol. 67, no. 7, pp. 4453–4462, Jul. 2019.

[228] T. Y. Yang, W. Hong, and Y. Zhang, "Wideband millimeter-wave substrate integrated waveguide cavity-backed rectangular patch antenna," IEEE Antennas Wireless Propag. Lett., vol. 13, pp. 205–208, 2014.

[229] Y. He, F. Yang, G. Han, and Y. Li, "High-throughput SatCom-on-the-move antennas: Technical overview and state-of-the-art," *Digital Commun. Netw*., vol. 10, no. 6, pp. 1760–1768, 2024.

[230] A. Serra, P. Nepa, G. Manara, G. Tribellini, and S. Cioci, "A Wide-Band Dual Polarized Stacked Patch Antenna," *IEEE Antennas Wireless Propag. Lett*., vol. 6, pp. 141–143, 2007.

[231] F. E. Gardiol and J. Zurcher, "Broadband patch antennas – A SSFIP update," in *IEEE Antennas Propag. Soc. Intern. Symp*., vol. 1, pp. 2–5, 1996.

[232] Barba, Mariano, "A high-isolation, wideband and dual-linear polarization patch antenna," in *IEEE Trans. Antennas Propag*., vol. 56, n. 5, pp. 1472–1476, 2008.

[233] Davide Guarnera, Marco Simone, Antonella M. Loconsole, Md. Imran Khan, Francesco Anelli, Santi C. Pavone, Francesco Prudenzano, Gino Sorbello ," Design of a Dual-Polarised Wide-Band Stacked-Patch Array for Ku Band Satcom On-the-Move," *IET Microwaves, Antennas & Propagation*: e70081,2026.

[234] Bilgic, MM and Yegin, Korkut, "Wideband offset slot-coupled patch antenna array for X/Ku-band multimode radars," in *IEEE Antennas Wireless Propag. Lett*., vol. 13, pp. 157–160, 2014.

[235] Kazemi, Reza and Fallah, Mohsen and Abbasi Arand, Bijan and Mohseni Armaki, Hossein, "Wideband stacked patch antenna array with reduced sidelobes for Ku band applications," in *Electromagnetics*, vol. 41, n. 6, pp. 432–447, 2021.

[236] Cao, Yufan and Cai, Yang and Cao, Wenquan and Xi, Baokun and Qian, Zuping and Wu, Tao and Zhu, Lei, "Broadband and high-gain microstrip patch antenna loaded with parasitic mushroom-type structure," in *IEEE Antennas Wireless Propag. Lett*., vol. 18, n. 7, pp. 1405–1409, 2019.

[237] Sarkar, Tanmoy and Ghosh, Abhijyoti and Singh, L Lolit Kumar and Chattopadhyay, Sudipta and Sim, Chow-Yen-Desmond, "DGS-inte-

grated air-loaded wideband microstrip antenna for X-and Ku-band," in *IEEE Antennas Wireless Propag. Lett*., vol. 19, n. 1, pp. 114–118, 2019.

[238] SWang, Wei and Wang, Jing and Liu, Aimeng and Tian, Yuhang, "A novel broadband and high-isolation dual-polarized microstrip antenna array based on quasi substrate integrated waveguide technology," in *IEEE Trans. Antennas Propag*., vol. 66, n. 2, pp. 951–956, 2017.

[239] Lu, Yunlong and Shen, Shuhao and You, Yang and Xu, Jun and Huang, Jifu, "Wideband dual linearly polarized hollow-waveguide septum antenna array for Ku-band satellite communications," in *IEEE Trans. Antennas Propag.*, vol. 71, n. 3 pp. 2433–2442, 2023.

[240] Yang, Yu-Hang and Liu, Bing-Yi and Zhou, Shi-Gang, "A wideband cavity-backed dual-polarized antenna for X-band applications," in *IEEE Antennas Wireless Propag. Lett*., vol. 22, n. 4, pp. 913–917, 2022.

[241] Paryani, Rajesh C and Wahid, Parveen F and Behdad, Nader, "A wideband, dual-polarized, substrate-integrated cavity-backed slot antenna," in *IEEE Antennas Wireless Propag. Lett*., vol. 9, pp. 645–648, 2010.

[242] Zhou, Shi-Gang and Peng, Zhao-Hang and Huang, Guan-Long and Li, Jian-Ying and Sim, Chow-Yen-Desmond, "Design of wideband and dual polarized cavity antenna planar array," in *IEEE Trans. Antennas Propag*., vol. 64, n. 10, pp. 4565 – 4569, 2016.

Acknowledgements

Completing this PhD has been a significant milestone in my academic journey, and I would like to acknowledge the people and institutions that supported me along the way.

My sincere appreciation goes to my supervisor, Professor Francesco Prudenzano, whose guidance, constructive feedback, and constant encouragement greatly contributed to the development of this work. His experience, patience, and trust created a motivating research environment and allowed me to approach my work with independence and curiosity.

I am also grateful to the Italian government for providing the PhD scholarship that enabled me to pursue my doctoral studies. This financial support played a fundamental role in allowing me to dedicate myself fully to research and to successfully complete this program.

I would like to thank my colleagues for the collaborative atmosphere they created during these years. The exchange of ideas, technical discussions, and shared experiences made the research process both stimulating and rewarding.

My deepest gratitude is reserved for my parents, whose unconditional love, sacrifices, and continuous encouragement have always been the foundation of my achievements.

Finally, I would like to acknowledge my friends who stood by me during the demanding moments of this path. Their support, patience, and companionship provided balance and helped make these years not only productive but also enjoyable.